

2/2011

**environment
protection
engineering**

published quarterly

Wrocław 2011

Founding Editor

TOMASZ WINNICKI

Editor-in-Chief

KATARZYNA MAJEWSKA-NOWAK

Vice-Editors

Jerzy ZWOŹDZIAK, Lucjan PAWŁOWSKI

Assistant Editor

IZABELA KOWALSKA

Editorial Office

Faculty of Environmental Engineering

Wrocław University of Technology

Wybrzeże Wyspiańskiego 27, 50-370 Wrocław, Poland

Publisher

Wrocław University of Technology, Wybrzeże Wyspiańskiego 27, 50-370 Wrocław
Wrocław University of Technology Press, Wrocław, Wybrzeże Wyspiańskiego 27

© Copyright by Oficyna Wydawnicza Politechniki Wrocławskiej, Wrocław 2011

Drukarnia Oficyny Wydawniczej Politechniki Wrocławskiej – Zam. 645/2011.

CONTENTS

J. KAWIECKA-SKOWRON, K. MAJEWSKA-NOWAK, Effect of dye content in a treated solution on performance of the UF ceramic membrane	5
R. STRAKA, J. MAKOVICKA, M. BENEŠ, Numerical simulation of NO production in a pulverized coal fired furnace	13
A. KOTOWSKI, A. DANCEWICZ, B. KAŽMIERCZAK, Accuracy of measurements of precipitation amount using standard and tipping bucket pluviographs in comparison to Hellmann rain gauges	23
A. BIELSKI, Modelling of mass transport in watercourses considering mass transfer between phases in unsteady states. Part I. Mass transfer process for periodic and aperiodic changes of concentration	35
Z. DUAN, Microbial degradation of phenol by activated sludge in a batch reactor	53
S. M. SHIRAZI, S. WIWAT, H. KAZAMA, J. KUWANO, M. G. SHAABAN, Salinity effect on swelling characteristics of compacted bentonite	65
M. KABSCH-KORBUTOWICZ, M. KUTYŁOWSKA, Use of artificial intelligence in predicting the turbidity retention coefficient during ultrafiltration of water	75
K. PIEKARSKA, M. ZACIERA, A. CZARNY, E. ZACZYŃSKA, Application of short-term tests in assessment of atmospheric air pollution	85
M. GŁOMBA, E. SZMIGIELSKA, Impact of limestone grinding degree on the volume of the absorption suspension tank in flue gas desulphurization systems	99
K. JUDA-REZLER, M. REIZER, W. TRAPP, Analysis of possible climate change impacts on air pollution by sulfur species over central eastern Europe	109
M. BRANC, J. HORÁK T. OCHODEK, Fine particle emissions from combustion of wood and lignite in small furnaces	123
M. ZIELINA, W. DĄBROWSKI, Impact of raw water quality on operation of variable declining rate filter plants	133

JOANNA KAWIECKA-SKOWRON*, KATARZYNA MAJEWSKA-NOWAK*

EFFECT OF DYE CONTENT IN A TREATED SOLUTION ON PERFORMANCE OF THE UF CERAMIC MEMBRANE

Low-pressure membrane processes have been studied in order to treat aqueous solutions of dyes. The influence of dye concentration (10, 20, 100 g/m³) on separation efficiencies of organic dyes (Methyl Orange, Titan Yellow and Direct Black) was analyzed. CéRAM INSIDE® (Tami Industries) membranes with various cut-off values (1, 15 kDa) were examined. The ultrafiltration process was carried out at the transmembrane pressures of: 0.03, 0.06, and 0.09 MPa. It was found that the process efficacy was affected not only by the kind of dye, but also by the dye concentration, applied pressure and membrane cut-off. With increasing dye content in the treated solution the rejection coefficient improved.

1. INTRODUCTION

Lack of water is a worldwide problem that will be exacerbated by water pollution. The textile industry consumes large volumes of water in numerous wet processes. Therefore it produces enormous amounts of textile wastewater heavily charged with unconsumed dyes and other chemicals [1]. Dyeing wastewater contains large amounts of dyestuff together with significant amounts of suspended solids, dispersing agents, salts and trace metals. This dyeing wastewater can cause serious environmental problems due to its high colour, large amount of suspended solids and high chemical oxygen demand [2]. Even small quantities of dyes can determine colour of large water bodies [3, 4]. Coloured dye effluents are generally considered highly toxic to the aquatic biota, affecting the symbiotic process by disturbing the natural equilibrium through reduced photosynthetic activity due to the colouration of water in streams. Some dyes are reported to cause allergy, dermatitis, skin irritation, and cancer in humans. Thus, the removal of dyes from effluents before they are mixed up with unpolluted natural water bodies is important [5, 6].

*Institute of Environmental Protection Engineering, Wrocław University of Technology, Wybrzeże Wyspiańskiego 27, 50-370 Wrocław, Poland. Corresponding author Joanna Kawiecka-Skowron, e-mail: joanna.kawiecka-skowron@pwr.wroc.pl

The treatment of wastewater containing dyes and its decolourization involves serious problems. A wide range of pH, high salt concentrations and complex chemical structures hinder even more their treatment [4]. The conventional treatments of wastewater containing dyestuff include biological oxidation, chemical coagulation and adsorption. The traditional processes for treatment of dye-house effluents prove to be insufficient to purify the important quantity of wastewater after the different operations of dyeing and washing [7]. Furthermore, the composition of wastewater from the dyeing and textile processes varies greatly from day to day and hour to hour, depending on the dyestuff type, the fabric type and the concentration of fixing compounds which are added [2].

Membrane separation processes could be a promising alternative for the removal of a variety of dyestuffs. Membrane pressure-driven processes, especially nanofiltration and reverse osmosis, are being increasingly used in the treatment of textile wastewater [8–13]. However, these techniques are characterized by high energy consumption. Therefore low-pressure membrane processes (microfiltration and ultrafiltration) could be economically more favourable in the dye effluent treatment.

A membrane installation should be characterized by a process stability, high availability, and simple preliminary treatment. Membranes applied should have high chemical, thermal and biological resistances. Ceramic membranes are able to meet these demands due to their high chemical and physical stability, and long lifespan. Other advantages of ceramic membranes include the ability to use steam sterilization and back flushing, high abrasion resistance, high fluxes, bacteria resistance, possibility of regeneration and dry storage after cleaning [14]. The supports for the inorganic membrane elements are made from aluminum oxides, zirconium oxides, titanium oxides or silicon carbides [15, 16]. These materials can fulfil high requirements relating to mechanical stability. The supports can be designed for a single-channel or multi-channels modules. The membrane layer is only few μm thick and is placed on the inner side of the channel.

The aim of the present paper was to investigate the membrane process efficiency for aqueous solutions containing three organic dyes at various concentrations in aqueous solutions. The effect of the dye concentration, as well as the molecular weight of the dye and the membrane cut-off on the process efficiency was reported.

2. MATERIALS AND METHODS

Commercially available CéRAM INSIDE® (Tami Industries) ceramic membranes, with the cut-off values of 1 kDa and 15 kDa, were used in the experiments. The membranes were 0.25 m long and had one channel with the diameter of 6 mm. The external diameter of the membrane was equal to 10 mm. The membrane surface area amounted to 0.0042 m^2 (per module).

Transport and separation properties of the membranes were tested with respect to three anionic dyes (Methyl Orange – MO, Titan Yellow – TY, Direct Black – DB). The characteristic of the dyes is given in Table 1. The molecular weights of tested dyes ranged from 327 to 1060 Da. The permeation measurements were carried out with distilled water and aqueous solutions of dyes. Dye concentrations in model solutions were equal to 10, 20 and 100 g/m³. The dye concentrations in permeate and concentrate were determined spectrophotometrically by measuring of the absorbance at the wavelength of maximum absorbance of the sample.

Table 1
Characteristics of the dyes under investigation

Dye	Molecular weight [Da]	Type	pH ^a	Dye	λ_{\max}^b [nm]	Structural formula
Methyl orange C.I. ^c 13025	327	acid dye	5.7	MO	465	C ₁₄ H ₁₄ N ₉ O ₉ SnA
Titan yellow C.I. 19540	696	direct dye	5.5	TY	399	C ₂₈ H ₁₉ N ₅ Na ₂ O ₆ S ₄
Direct black C.I. 35435	1060	direct dye	7.6	DB	585	C ₄₄ H ₃₂ N ₁₃ O ₁₁ S ₃ Na ₃

^aDetermined for the dye solutions of concentration equal to 100 g/m³.

^bWavelength corresponding to the maximum absorbance of the dye solution.

^cColour index number.

The ProFlux M12 (Millipore) installation (Fig. 1) was used in the experiments. To provide constant concentration of examined solutions, permeate was recirculated to the feeding tank. The ultrafiltration process involved the pressure range from 0.03 to 0.09 MPa.

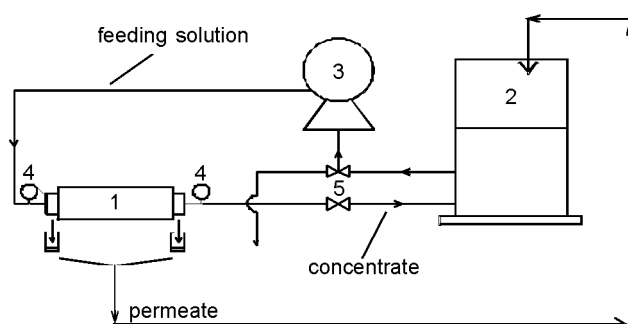


Fig. 1. Laboratory UF installation ProFlux M12: 1 – ceramic membrane module,
2 – feeding tank, 3 – pressure pump, 4 – pressure sensor, 5 – valve

3. RESULTS AND DISCUSSION

Figure 2 shows the distilled water flux at three transmembrane pressures for two membranes (1 kDa and 15 kDa). As it was expected there was an evident relationship

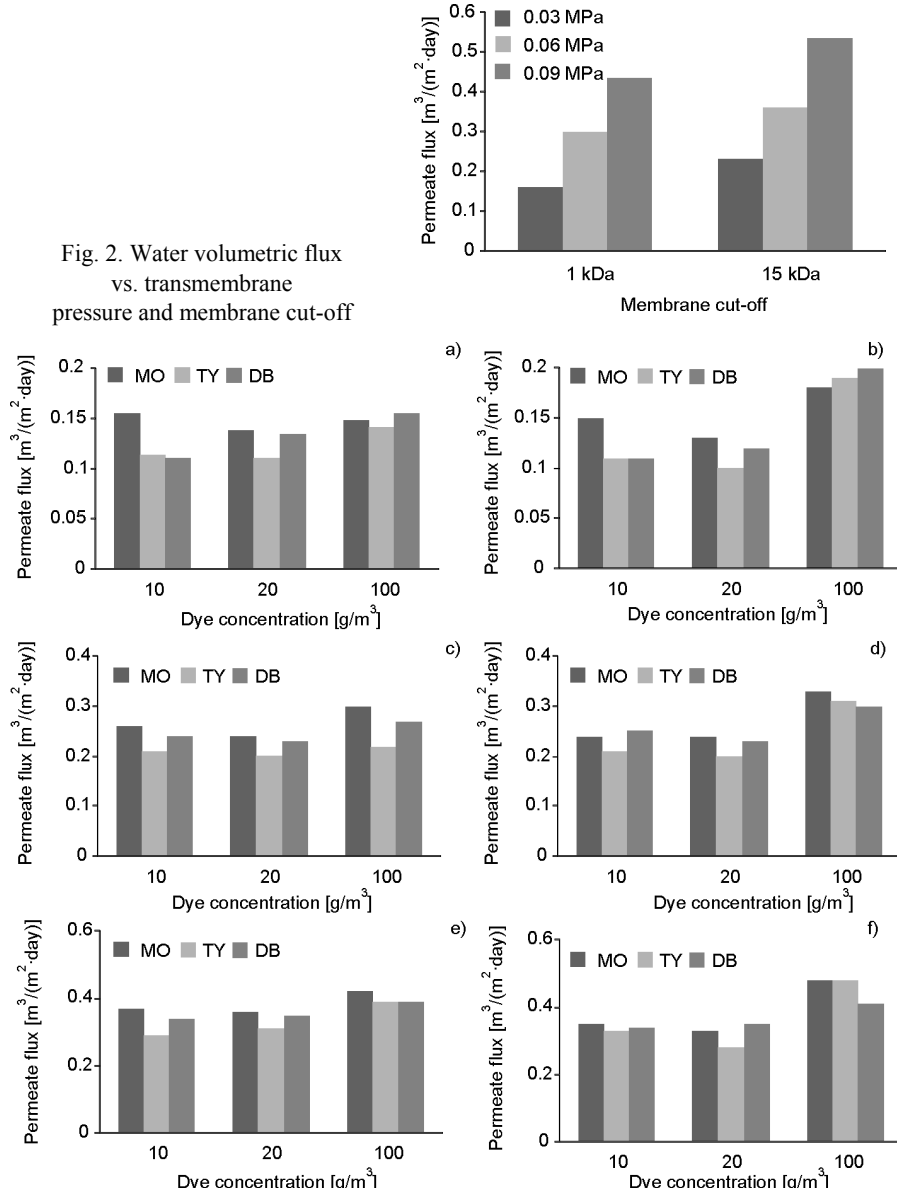


Fig. 3. Permeate volumetric flux of solutions containing MO, TY, DB for 1 (a, c, e) and 15 (b, d, f) kDa membranes vs. dye concentration under 0.03 (a, b), 0.06 (c, d), and 0.09 (e, f) MPa

between water permeability and applied pressure. It was also found that permeability of the membrane with the higher cut-off value was higher than the permeability of 1 kDa membrane. The water flux ranged from $0.16 \text{ m}^3/(\text{m}^2 \cdot \text{day})$ to $0.44 \text{ m}^3/(\text{m}^2 \cdot \text{day})$ for 1 kDa membrane and from $0.21 \text{ m}^3/(\text{m}^2 \cdot \text{day})$ to $0.54 \text{ m}^3/(\text{m}^2 \cdot \text{day})$ for the 15 kDa membrane.

The ceramic membrane permeabilities in the course of ultrafiltration of organic dyes solutions are shown in Fig. 3. It was found that the membrane permeability was dependent on the initial concentration of dye, the applied pressure and the membrane cut-off value. It is interesting to note that the membrane type was of less importance, although the distilled water fluxes varied with membrane cut-off (Fig. 2).

The lowest permeate flux (approximately $0.10 \text{ m}^3/(\text{m}^2 \cdot \text{day})$) was obtained under the pressure of 0.03 MPa (Figs. 3a, b). Increasing pressure caused the increase in the permeate flux (to approximately $0.48 \text{ m}^3/(\text{m}^2 \cdot \text{day})$) (Fig. 3f). The highest permeate flux was observed when the 15 kDa membrane was used under the highest pressure. Under the lowest pressure, the highest permeate flux was obtained for solutions with the highest initial concentration.

The presence of dye molecules in treated solutions caused decrease in the membrane permeabilities. This demonstrates that the membranes were blocked by rejected particles. As a measure of the pore blocking degree, the relative membrane permeability was taken into account (Table 2). It was determined as the ratio of the volumetric flux of a dye solution to water volumetric flux.

Table 2

The relative permeability of ceramic membranes

Dye	1 kDa membrane		15 kDa membrane			
	Dye concentration [g/m ³]					
	10	20	100	10	20	100
0.03 MPa						
MO	0.98	0.87	0.93	0.64	0.57	0.76
TY	0.72	0.70	0.89	0.46	0.45	0.81
DB	0.70	0.85	0.98	0.49	0.51	0.84
0.06 MPa						
MO	0.84	0.78	0.99	0.65	0.65	0.90
TY	0.69	0.67	0.74	0.58	0.54	0.85
DB	0.79	0.76	0.89	0.68	0.64	0.82
0.09 MPa						
MO	0.84	0.82	0.97	0.65	0.62	0.89
TY	0.67	0.71	0.90	0.62	0.52	0.90
DB	0.77	0.80	0.90	0.64	0.66	0.76

At higher initial concentrations of dyes, membrane blocking was less effective. This can be explained in terms of aggregation of dye particles in the treated solutions.

At low dye concentrations, the degree of aggregation is lower. Thus, non-aggregated dye particles can freely enter the membrane pores and block them. Aggregated dye particles, due to their bigger diameters, will be rejected by the membranes.

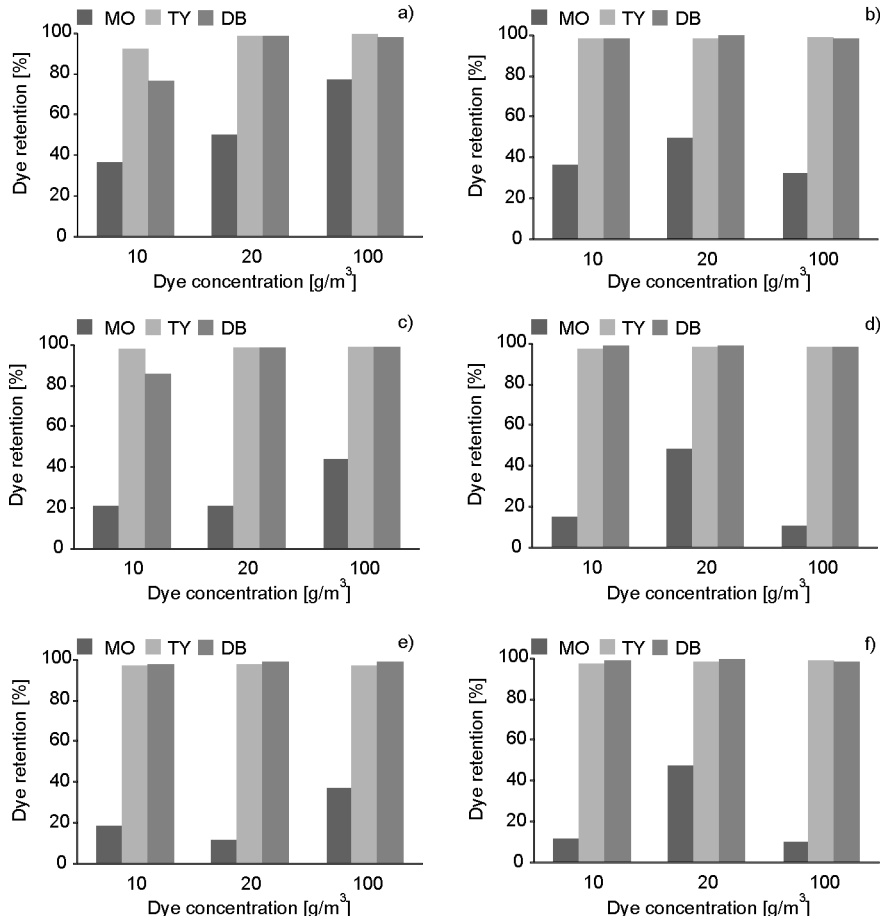


Fig. 4. Dye retention for solutions containing MO, TY, DB for 1 (a, c, e) and 15 (b, d, f) kDa membranes vs. dye concentration under 0.03 (a, b), 0.06 (c, d), and 0.09 (e, f) MPa

The transport properties of ceramic membranes influenced directly the separation properties. The experimental results are shown in Fig. 4. The molecular weight of a dye has a significant influence on the process efficiency. The dyes of higher molecular weight (Titan Yellow, Direct Black) were removed with much higher efficacy than the low molecular weight dye (Methyl Orange) irrespective of the membrane cut-off. The applied pressure had an insignificant influence on the removal efficiency of high-molecular weight dyes. Dye rejection coefficients for Titan Yellow and Direct Black were very high and varied from 85 to 99.3%, depending on the initial dye concentra-

tion. The worst removal efficiency was noticed when the initial dye concentration was lowest, but when the dye concentration was increasing, the results of ultrafiltration process were improved. When the initial concentration was equal to 10 g/m^3 the aggregation degree of dye particles was rather low, thus more single dye particles were available in the treated solution. As a consequence, the separation efficiency became worse.

The retention coefficient of Methyl Orange depended on the initial concentration of dye in a higher extent, but there was no visible trend between the initial concentration of dye and the removal efficiency. Generally, the separation of Methyl Orange was rather low – the retention coefficients varied from 11% to 77%, depending on the membrane cut-off and the applied pressure. The best results were obtained for 1 kDa membrane and the lowest pressure (Fig. 4a). The poor rejection of Methyl Orange could be attributed to small size of the dye particles. The worsening of separation of low molecular weight dye upon increasing pressure was observed. Higher pressure caused more intensive passing of dye particles through the membrane. When the concentration of Methyl Orange was the lowest and the applied pressure was the highest, there was the dye rejection was worst (Fig. 4e, f). Probably, under the low concentration, dye aggregation was hindered and a greater number of non-aggregated dye particles penetrated through the ceramic membrane.

4. CONCLUSIONS

The experimental results demonstrated that the commercially available ceramic membranes can be successfully applied to treat organic dye solutions, particularly when the solutions contain high-molecular-weight dyes ($> 700 \text{ Da}$). The effectiveness of organic dye removal depends on its initial concentration in the treated solution, applied pressure and the membrane cut-off. For low molecular weight dyes the increase in the membrane cut-off and transmembrane pressure causes worsening of dye rejection. For high molecular weight dyes the rejection degree is almost complete (97–99%) unless the dye content in the separated solution is rather high (100 g/m^3). The decrease of dye concentration brings about deterioration of the separation efficiency.

ACKNOWLEDGEMENT

The financial support of the Ministry of Science and Higher Education No. N N523 424637 is greatly appreciated.

REFERENCES

- [1] FORGACS E., CSERHÁTI T., OROS G., Environ. Int., 2004, 30 (7), 953.
- [2] KIM T.H., PARK C., YANG J., KIM S., J. Hazard Mater., 2004, 112 (1–2), 95.

- [3] MITTAL A., MALVIYA A., KAUR D., MITTAL J., KURUP L., *J. Hazard Mater.*, 2007, 148 (1–2), 229.
- [4] SANROMÁN M.A., PAZOS M., RICART M.T., CAMESELLE C., *Chemosphere*, 2004, 57 (3), 233.
- [5] BHATNAGAR A., JAIN A.K., MUKUL M.K., *Environ. Chem. Lett.*, 2004, 2 (4), 199.
- [6] SONG Y.L., LI J.T., *Ultrason. Sonochem.*, 2009, 16 (4), 440.
- [7] LI C.S., TANG Y.P., KANG B.N., WANG B.S., ZHOU F., MA Q., XIAO J., WANG D.Z., LIANG J., *Sci. China Ser. E, Tech. Sci.*, 2007, 50 (3), 279.
- [8] AL-BASTAKI N., *Chem. Eng. Process.*, 2004, 43 (12), 1561.
- [9] ALLÈGRE C., MOULIN P., MAISSEU M., CHARBIT F., *J. Membr. Sci.*, 2006, 269 (1–2), 15.
- [10] KIM T.H., PARK C., KIM S., *J. Clean. Prod.*, 2005, 13 (8), 779.
- [11] AL-ASEERI M., BU-ALI Q., HAJI S., AL-BASATAKI N., *Desalination*, 2007, 206 (1–30), 407.
- [12] MO J.H., LEE Y.H., KIM J., JEONG J.Y., JEGAL J., *Dyes Pigments*, 2008, 76 (2), 429.
- [13] PETRINIĆ I., ANDERSEN N.P.R., ŠOSTAR-TURK S., MARECHAL A.M.L., *Dyes Pigments*, 2007, 74 (3), 512.
- [14] FINLEY J., *Filtr. Sep.*, 2005, 42 (9), 34.
- [15] ZENG Z., XIAO X., GUI Z., LI L., *J. Membr. Sci.*, 1997, 136 (1–2), 153.
- [16] TSURU T., *J. Sol-Gel Sci. Technol.*, 2008, 46 (3), 349.

R. STRAKA*, J. MAKOVIČKA**, M. BENEŠ**

NUMERICAL SIMULATION OF NO PRODUCTION IN A PULVERIZED COAL FIRED FURNACE

Behaviour of air-coal mixture has been described using the Navier–Stokes equations for the mixture of air and coal particles, accompanied by the turbulence model. The undergoing chemical reactions are described by the Arrhenius kinetics (reaction rate proportional to $\exp(-E/RT)$). Heat transfer via conduction and radiation has also been considered. The system of partial difference equations is discretized using the finite volume method and the advection upstream splitting method as the Riemann solver. The resulting ordinary differential equations are solved using the 4th order Runge–Kutta method. Results of simulation for typical power production level are presented together with the air staging impact on NO production.

1. INTRODUCTION

The main motivation of the examination of the combustion model is its potential inclusion in the current model of a steam generator [1], to use this model for development of control systems for the industrial installation. Another application for the combustion model is the optimization of the production of nitrogen oxide which strongly depends on the temperature and unburned char distribution, and thus it can be controlled by intelligent distribution of fuel and oxygen into the burners. Because the experiments on a real device are prohibitively cumbersome and expensive, in extreme cases even hazardous, the only way to test the behaviour of the furnace is mathematical modelling.

The mathematical model of combustion is based on the Navier–Stokes equations for a mixture of multiple components where coal particles are treated as one of the phases. We use this approach, as it simplifies the model especially when dealing with

*Department of Heat Engineering and Environment Protection, Faculty of Metals Engineering and Industrial Computer Science, AGH University of Science and Technology, al. Mickiewicza 30, 30-059, Cracow, Poland, e-mail: straka@metal.agh.edu.pl

**Department of Mathematics, Faculty of Nuclear Sciences and Physical Engineering, Czech Technical University, Trojanova 13, 120-00, Prague, Czech Republic.

turbulence, and also removes several empirical relations and constants, moreover, it shortens the computational time of the simulation.

2. MATHEMATICAL MODEL

The mathematical model of combustion is based on the Navier–Stokes equations for a mixture of multiple components where the coal particles are treated as one of the phases. Unlike e.g. in [2], where the gas particles are treated separately and use separate equations of momentum, we chose to use this approach, as it simplifies the model especially when dealing with turbulence, and also removes several empirical relations and constants.

Currently, the following components of the mixture are considered:

- chemical compounds engaged in major thermal and fuel NO reactions (nitrogen (N_2), oxygen (O_2), nitric oxide (NO), hydrogen cyanide (HCN), ammonia (NH_3), carbon dioxide (CO_2) and water (H_2O)),
- char and volatile part of the coal particle.

The gas phase is described by equations given below. The mass balance is described by equations of mass balance of each sub-component (the Einstein summation is used)

$$\frac{\partial}{\partial t}(\rho Y_i) + \frac{\partial}{\partial x_j}(\rho Y_i u_j) = \nabla \vec{J}_i + R_i, \quad (1)$$

where ρ is the flue gas mass density, Y_i – mass fraction of the i -th component, and u_i are the gas velocity components. The right hand side terms describe the laminar and turbulent diffusion of the components and either production or consumption due to chemical reactions within the R_i term. The equations of mass balance of components are supplemented by the equation of total mass balance:

$$\frac{\partial \rho}{\partial t} + \frac{\partial(\rho u_j)}{\partial x_j} = 0. \quad (2)$$

Equations of momentum conservation are as follows

$$\frac{\partial}{\partial t}(\rho u_i) + \frac{\partial(\rho u_i u_j)}{\partial x_j} = -\frac{\partial p}{\partial x_i} + \frac{\partial}{\partial x_i} \left[\mu_{eff} \left(\frac{\partial u_i}{\partial x_j} + \frac{\partial u_j}{\partial x_i} - \frac{2}{3} \delta_{ij} \frac{\partial u_l}{\partial x_l} \right) \right] + g_i, \quad (3)$$

where $\vec{g} = [g_1, g_2, g_3]$ is the external force acting on the fluid, in our case it is the gravity force. The effective friction coefficient μ_{eff} is calculated from the turbulence model as

$$\mu_{\text{eff}} = \mu + \mu_t = \mu + \rho C_\mu \frac{k^2}{\varepsilon},$$

where μ is the laminar viscosity, k – the turbulent kinetic energy, and ε – the turbulent energy dissipation rate. Constant C_μ , like additional constants introduced later in the description of the turbulence model, has to be chosen empirically for a particular problem, in our case we use $C_\mu = 0.09$, which appears to give satisfactory results.

The last equation describes the conservation of energy

$$\frac{\partial}{\partial t}(\rho h) + \frac{\partial(\rho u_j h)}{\partial x_j} = -n_{\text{coal}} \frac{dm_{\text{coal}}}{dt} h_{\text{comb}} + q_r + q_c + q_s, \quad (4)$$

where the right hand side terms are the heat of combustion, heat transfer by radiation, heat transfer by conduction, and heat source or sink. The heat transfer terms are computed as follows

$$q_c = -\nabla \cdot (\lambda \nabla T),$$

for the transfer by conduction, which is described by the Fourier law of heat conduction, and

$$q_r = -\nabla \cdot (c T^3 \nabla T),$$

for the transfer by radiation. The radiation heat transfer is fully described by an integral-differential equation of radiation, which is very computationally expensive to solve. However, as the flue gas can be considered an optically thick matter, the above approximation of the radiation flux called the Rosseland radiation model can be applied.

The heat sink term is nonzero only in the edge computation cells and describes the energy exchange with the walls of the furnace via conduction and radiation

$$q_s = A(T_{\text{gas}} - T_{\text{wall}}) - B(T_{\text{gas}}^4 - T_{\text{wall}}^4),$$

where A and B are constants dependent on the properties of the interface between the modelled region and its surroundings.

The particle mass change rate is currently described by the one-step Arrhenius kinetics, which is used separately for the char and volatile coal components – combustion of the volatiles is more rapid than combustion of the char

$$\frac{dm_p}{dt} = -A_v m_p^\alpha [\text{O}_2]^\beta \exp\left(-\frac{E_v}{RT_p}\right),$$

where m_p is the particle combustible mass, A_v , E_v are empirical constants, $[\text{O}_2]$ – oxygen concentration, T_p is the particle temperature and R is the universal gas constant.

As usual, these equations are supplemented by the equation of state

$$p = (\kappa - 1)\rho \left(e_{\text{gas}} - \frac{1}{2}v_{\text{gas}}^2 \right),$$

where κ is the Poisson constant and e_{gas} is the gas energy per unit mass.

For the turbulence modelling, we use the standard $k-\varepsilon$ model, which describes the evolution of turbulence using two equations, former for the turbulent kinetic energy

$$\frac{\partial}{\partial t}(\rho k) + \frac{\partial(\rho u_j k)}{\partial x_j} = \frac{\partial}{\partial x_j} \left[\left(\mu + \frac{\mu_t}{\sigma_k} \right) \frac{\partial k}{\partial x_j} \right] + G_k - \rho \varepsilon, \quad (5)$$

and the other one for the turbulent kinetic energy dissipation rate

$$\frac{\partial}{\partial t}(\rho \varepsilon) + \frac{\partial(\rho u_j \varepsilon)}{\partial x_j} = \frac{\partial}{\partial x_j} \left[\left(\mu + \frac{\mu_t}{\sigma_\varepsilon} \right) \frac{\partial \varepsilon}{\partial x_j} \right] + C_{1\varepsilon} \frac{\varepsilon}{k} G_k - \rho C_{2\varepsilon} \frac{\varepsilon^2}{k}. \quad (6)$$

Constants in this model have once more to be determined empirically, in our case they are: $C_{1\varepsilon} = 1.44$, $C_{2\varepsilon} = 1.92$, $\sigma_k = 1.0$, $\sigma_\varepsilon = 1.3$.

Left hand sides of the equations describe passive advection of the respective quantities by the advection velocity \vec{u} . Right hand sides describe their spatial diffusion, production and dissipation.

The term G_k describing the production of turbulence, can be derived from the Reynolds averaging process and written in terms of the fluctuating part of the velocity as

$$G_k = \tau_{jl} \frac{\partial u_j}{\partial x_l} = -\rho \bar{u}'_j \bar{u}'_l \frac{\partial u_j}{\partial x_l} = \mu_t S^2 \quad \text{with} \quad S_{ij} = \frac{1}{2} \left(\frac{\partial u_i}{\partial x_j} + \frac{\partial u_j}{\partial x_i} \right),$$

where τ_{jl} is the Reynolds stress tensor and S_{ij} is a mean strain rate. However during practical computation, fluctuations u'_j and u'_l are unknown, we use the Boussinesq hypothesis that the Reynolds stress is proportional to the mean strain rate.

Diffusion of the species consists of two processes, laminar and turbulent ones, and the diffusion term in Eq. (1) can be written in the form

$$\vec{J}_i = - \left(\rho D_{i,m} + \frac{\mu_t}{Sc_t} \right) \nabla Y_i.$$

The former term corresponds to linear laminar diffusion, the latter one to turbulent diffusion. Given the fact that the turbulent diffusion generally predominate the laminar one, and the term $D_{i,m}$ is difficult to determine, the laminar diffusion can be usually ignored. The coefficient Sc_t is the turbulent Schmidt number and we have $Sc_t = 0.7$.

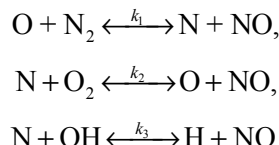
3. SIMPLIFIED MODEL OF NO CHEMISTRY

This model has been developed to approximately describe the amounts of NO emissions leaving a coal combustion furnace. The real mechanism of coal flue gas production seems to be very complicated, so that just the most important phenomena and reaction paths were considered to provide maximum possibility of using this model in real-time control and operation systems.

Two major processes contribute to the total NO chemistry. The former is known as thermal NO or Zeldovich NO and simply consists of oxidation of atmospheric nitrogen at high temperature. The latter is called fuel NO and describes creation of NO from nitrogen, which is chemically bounded in coal fuel. Fuel NO is usually the major source of NO emissions, when the thermal way is suppressed. These are the only mechanisms involved, although a few more could be considered (such as prompt NO (Fenimore) or nitrous oxide (N_2O) intermediate mechanisms).

3.1. THERMAL NO

Thermal NO generation mechanism is applicable only at high temperature and is represented by a set of three equations, introduced by Zeldovich [2] and extended by Bowman [3]



All these reactions are considered to be reversible. Rate constants were taken from [4]. In order to compute the NO concentration, concentrations of nitrogen radical [N], oxygen radical [O] and hydroxyl radical [OH] must be known. It is useful to assume that N is in a quasi-steady state according to its nearly immediate conservation after creation. In fact, this N radical formation is the rate limiting factor for thermal NO production, due to extremely high activation energy of nitrogen molecule, which is caused by a triple bond between two nitrogen atoms. Hence, the NO formation rate can be stated as

$$\frac{d[NO]}{dt} = 2k_1^+[O][N_2] \frac{1 - \frac{k_1^- k_2^- [NO]^2}{k_1^+ k_2^+ [N_2][O_2]}}{1 + \frac{k_1^- [NO]}{k_2^+ [O_2] + k_3^+ [OH]}}.$$

Concentrations of O and OH can be profitably described by following partial equilibrium approach [5, 6]

$$[\text{O}] = K_1 [\text{O}_2]^{1/2} T^{1/2}, \quad [\text{OH}] = K_2 [\text{O}]^{1/2} [\text{H}_2\text{O}]^{1/2} T^{-0.57}.$$

Equilibrium constants are as follows

$$K_1 = 36.64 \exp\left(-\frac{27123}{T}\right), \quad K_2 = 212.9 \exp\left(-\frac{4595}{T}\right).$$

3.2. FUEL NO

The composition analysis shows that nitrogen based species are more or less present in coal, usually in amounts of tenths to units of percent by weight. When coal is heated, these species are transformed into certain intermediates and then into NO. Fuel itself is therefore a significant source of NO pollutants. When a coal particle is heated, it is presumed that nitrogen compounds are distributed into volatiles and char. The parameter α is introduced to describe the distribution of the coal-bounded nitrogen between the volatiles and char part of the coal particle.

$$m_{\text{vol}}^{\text{N}} = \alpha m_{\text{tot}}^{\text{N}}, \quad m_{\text{char}}^{\text{N}} = (1 - \alpha) m_{\text{tot}}^{\text{N}},$$

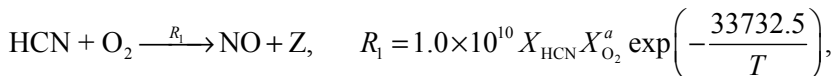
where $\alpha \in \langle 0, 1 \rangle$, $m_{\text{tot}}^{\text{N}}$ is the total mass of nitrogen per 1 kg of the coal used in boiler, $m_{\text{vol}}^{\text{N}}$ is the mass of bounded nitrogen in volatiles and $m_{\text{char}}^{\text{N}}$ is the mass of bounded nitrogen in char. As mentioned above, nitrogen transforms to pollutants via intermediates which usually are ammonia NH_3 , and hydrogen cyanide HCN . To proceed further, we must define four parameters to describe complex partitioning of the fuel bound nitrogen:

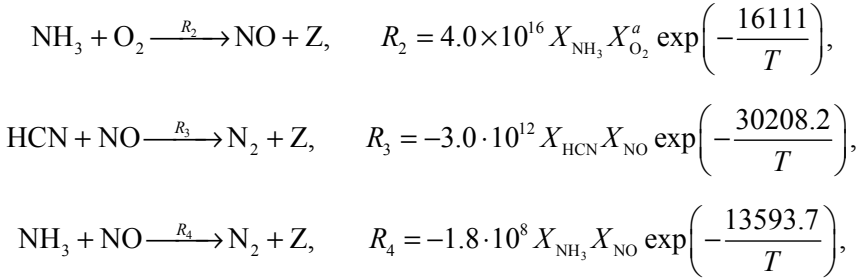
- β is a part of volatile bounded nitrogen which converts to HCN ,
- δ_1 is the distribution of char bounded nitrogen which converts to HCN ,
- δ_2 is the distribution of char bounded nitrogen which converts to NH_3 ,
- δ_3 is the distribution of char bounded nitrogen which converts to NO ,

$$\beta \in \langle 0, 1 \rangle, \quad \delta_1 + \delta_2 + \delta_3 = 1.$$

Different parametric studies should be carried out to find the best values of these parameters suitable for a specific type of coal. Five overall reactions of either NO formation or depletion were incorporated in the combustion part of the numerical code.

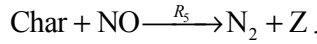
NO, HCN, NH₃ reactions. According to [7], we have following reactions and their formation rates





where X is the mole fraction, a is the oxygen reaction order and Z are other products we simply neglect.

Heterogeneous reduction of NO. Present char allows following adsorption process to occur



Levy [8] uses surface area of pores (BET) to define NO source term

$$S_{\text{ads}}^{\text{NO}} = R_5 c_s A_{\text{BET}} M_{\text{NO}} p_{\text{NO}},$$

where $R_5 = 2.27 \times 10^{-3} \exp(-17168.33/T)$ is the rate constant, $S_{\text{ads}}^{\text{NO}}$ is the NO source term, c_s is the concentration of particles, A_{BET} is the pore surface area and P_{NO} is the partial pressure of NO.

In order to evaluate overall NO source term, single source terms have to be summarized. This overall source term can be further used in transport equations. As for HCN and NH₃ source terms, it is possible to determine them from coal burnout rate. It is assumed that nitrogen from both char and volatiles transforms to intermediate species quickly and totally.

For numerical solution of the equations, the finite volume method is used. For left and right hand sides in Eqs. (1)–(6), advection upstream splitting method (cf. [9]) is used to approximate fluxes in the FVM formulation, and edge dual volume approximation is used to approximate the second order derivatives, respectively. For detailed description of the solution procedure see [1].

4. RESULTS

In Table 1, the values of various parameters used in simulation are given as well as summarized numerical values of air and fuel distribution among the burners, excess air coefficients for the burners and outlet concentration of NO, CO₂ and O₂ taken from the outlet area of the boiler. In Figure 1, profiles of mass fractions of NO are shown spatial-averaged over the boiler cross section area.

Table 1

Simulation parameters and fuel/air proportions for studied cases

Parameter								Symbol	Value						
Gas heat capacity [$\text{J}\cdot\text{kg}^{-1}\cdot\text{K}^{-1}$]								c_V	1037.0						
Molar weight of gas [$\text{kg}\cdot\text{mol}^{-1}$]								M	0.02896						
Raw coal density [$\text{kg}\cdot\text{m}^{-3}$]								ρ	1345.0						
Coal particle radius [m]								r_{coal}	0.2×10^{-3}						
Coal heat capacity [$\text{J}\cdot\text{kg}^{-1}\cdot\text{K}^{-1}$]								c_{coal}	2048						
Boiler cross-section [m^2]								S	49						
Coal feeding rate [$\text{kg}\cdot\text{s}^{-1}$]								\dot{m}_{coal}	5.63						
Initial pressure [Pa]								p_{ini}	1×10^5						
Initial temperature [°C]								T_{ini}	800						
Mixture temperature at the inlet [°C]								T_{mix}	350						
Pressure at the inlet [Pa]								p_{in}	1×10^5						
Pressure at the outlet [Pa]								p_{out}	$p_{\text{in}} - 100$						
Excess air coefficient								α	1.3						
Temperature of the wall [°C]								T_{wall}	300						
Width of the side wall [m]								a, b	7.0						
First burners row position [m]								B_1	2.74						
Second burners row positions [m]								B_2	3.84						
Third burners row position [m]								B_3	4.93						
Fourth burners row position [m]								B_4	6.03						
Number of burners in a row								N_B	4						
Burner diameter [m]								D_B	0.8						
Gas-wall heat transfer coefficient due to conduction [$\text{W}\cdot\text{m}^{-2}\cdot\text{K}^{-1}$]									30.0						
Gas-wall heat transfer coefficient due to radiation [$\text{W}\cdot\text{m}^{-2}\cdot\text{K}^{-4}$]									0.6×10^{-8}						
Results of coal analysis [%]															
Ash								A	9.5						
Water								W	30						
Carbon								C	45.72						
Hydrogen								H	3.69						
Sulfur								S	1.16						
Oxygen								O	9.42						
Nitrogen								N	0.5						
Case	Air distribution [%]				Fuel distribution [%]				Excess air coefficient						
	B_1	B_2	B_3	B_4	B_1	B_2	B_3	B_4	B_1	B_2					
1	25	25	25	25	25	25	25	25	1.3	1.3	1.3	1.3	357	20	1.9
2	50	20	20	10	25	25	25	25	2.6	1.04	1.04	0.52	177	20	1.9
3	10	20	20	50	25	25	25	25	0.52	1.04	1.04	2.6	134	20	2
4	25	25	25	25	50	20	20	10	0.65	1.63	1.63	3.25	182	18	4.5
5	25	25	25	25	10	20	20	50	3.25	1.63	1.63	0.65	233	20	2
6	10	20	20	50	10	20	20	50	1.3	1.3	1.3	1.3	355	20	2
7	50	20	20	10	50	20	20	10	1.3	1.3	1.3	1.3	388	20	1.9
8	50	20	20	10	10	20	20	50	6.5	1.3	1.3	0.26	173	20	1.9
9	10	20	20	50	50	20	20	10	0.26	1.3	1.3	6.5	124	20	2

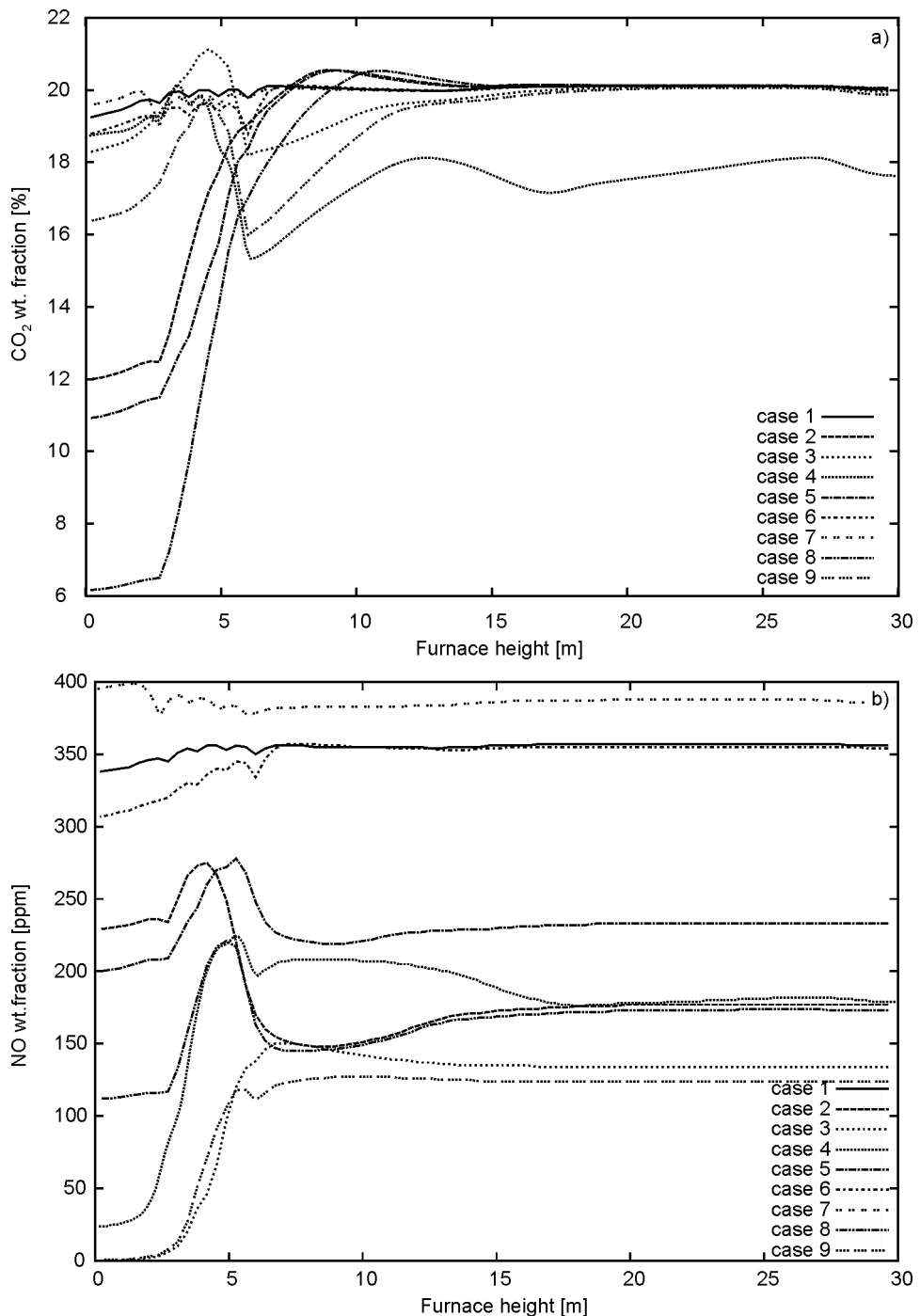


Fig. 1. Profiles of CO_2 (a) and NO (b) weight fractions for various arrangements of air and fuel

Averaged values are computed after 35 s of boiler operation. One can see that the lowest NO concentrations are obtained for the configuration 3 and 9. This is consistent with creating fuel-rich, oxygen-lean zone in the lower part of the burners, where the temperature is low and thermal NO production is inefficient, fuel NO is low because of low oxygen concentration and NO is also reduced on the char surface which is greater because of high concentration of fuel.

5. CONCLUSION

A numerical model of pulverized coal fired boiler has been presented. It has been developed taking into consideration the balance between computation complexity and the precision of simulation. This was also the reason for using a simplified reaction kinetics instead of full reaction set for the production of NO and simple kinetic approach of the coal particle combustion. At current state, the model can be used as air-stage designing tool for coal fired boilers. Presented results with emphasis on the NO production are adequate when compared with real life devices, as well as model behaviour for different cases. Still there are places where enhance of the model is needed, mainly the radiation heat transfer modelling and more accurate coal particle combustion model.

ACKNOWLEDGMENTS

This work has been partly supported by the project *Applied Mathematics in Physical and Technical Sciences* MSM 6840770010 and *Jindřich Nečas Center for Mathematical Modelling* of the Czech Ministry of Education, Youth and Sport.

REFERENCES

- [1] MAKOVÍČKA J., HAVLENA V., BENEŠ M., *ALGORITMY 2002*, Proc. contributed papers, 2002, 171.
- [2] ZELDOVICH J.B., *Acta Physicochim. URSS*, 1946, 21, 577.
- [3] BOWMAN C.T., SEERY D.J., *Emissions from Continuous Combustion Systems*, Plenum Press, New York, 1972.
- [4] NIST, Chemical Kinetics Database on the Web., National Institute of Standards and Technology, <http://www.kinetics.nist.gov>, 2000.
- [5] WARNATZ J., *NO_x Formation in High Temperature Processes*, University of Stuttgart, Germany, 2001.
- [6] BAULCH D.L., *J. Phys. Chem. Ref. Data*, 1992, 21, 411.
- [7] DE SOETE G.G., Proc. 15th Int. Symposium on Combustion, 1975, 1093.
- [8] LEVY J.M., CHEN L.K., SAROFIM A.F., BEER J.M., Proc. 15th Int. Symposium on Combustion, 1981, 111.
- [9] LIOU M.S., STEFFEN Jr. C., *J. Comput. Phys.*, 1993, 107, 23.

ANDRZEJ KOTOWSKI*, ANDRZEJ DANCEWICZ**, BARTOSZ KAŽMIERCZAK*

ACCURACY OF MEASUREMENTS OF PRECIPITATION AMOUNT USING STANDARD AND TIPPING BUCKET PLUVIOPHOTOGRAPHS IN COMPARISON TO HELLMANN RAIN GAUGES

Accuracy of measurements of the precipitation amount in function of time has been analysed using a traditional pluviograph and a new generation tipping bucket pluviograph (SEBA) in comparison to standard Hellmann's rain gauge. It was based on pluviographic material from IMGW meteorological station in Legnica (warm half-year from May to October 2009). The comparisons were made for 4 typical balance precipitation periods: May–October period, 1 month, 24 h, 360 min. For balance periods: season, month, 24 hours it was considered sufficiently accurate and approximately equal. However the analysis of short term precipitation (up to 360 min) showed that the biggest differences in precipitation amounts occur in the first 5 min of the rainfall time interval. Mutual differences between precipitation at definite time intervals for pluviograph and SEBA pluviograph are the lowest when they are used for interpreting pluviograms of changeable intervals of precipitation time. In the case of very intensive rainfalls, reaching the height of several millimeters during 5 min, it showed an underestimation of about 10–20% of the precipitation height by the SEBA pluviograph in comparison to the traditional pluviograph.

1. INTRODUCTION

In Poland, modelling of sewage systems, either existing or being designed, recommended by the standard PN-EN 752:2008, encounters a barrier of the lack of access to reliable and suitable precipitation databases [1–3]. As often as not, precipitation histograms are essential as the input to hydrodynamic models with at least 5 min time resolution. In Poland, the access to source precipitation data (recorded on paper pluviographs until 2007) is managed by the Institute of Meteorology and Water Management (IMGW), the proprietor of the most meteorological stations in the country.

*Institute of Environmental Protection Engineering, Wrocław University of Technology, Wybrzeże Wyspiańskiego 27, 50-370 Wrocław, Poland. E-mail: andrzej.kotowski@pwr.wroc.pl (corresponding author).

**Institute of Meteorology and Water Management, ul. Parkowa 30, 51-616 Wrocław, Poland. E-mail: andrzej.dancewicz@imgw.wroc.pl

It is possible to obtain a paid access to such databases at IMGW, however one can more often order a statistic analysis of precipitation (according to standard studies) for example with regard to the specification of local dependences of IDF or DDF type, that is, precipitation intensity or its amount with respect to time and frequency of occurrence.

Precipitation synthetic hietograms – randomly generated, but still in an experimental stage – can provide a solution, however, they also require high resolution source data [4–6]. The knowledge of recorded twenty four hours sums of precipitation amount, which are easily available, can be a starting point for their generation. A random generator is applied to carry out a classic down-scaling, that is, to isolate a twenty four hour precipitation into an equal time scale, a 5 min scale for example. In the case of short term data (few hours), the starting point for generation of synthetic hietograms also requires the knowledge of precipitation amount and duration for specific occurrence frequency, however the existing, local formulae of IDF or DDF type can be used here.

The paper is the authors' contribution to existing discussion on the choice of a new generation automatic pluviograph as the successor of the traditional float pluviograph (clock-driven and recording on a paper tape) for recording time dependences of precipitation. The most important criterion should be the most accurate recording of actual precipitation amounts, both (simultaneously) in long periods of time: a season, month or twenty four hours and particularly in shorter periods – from several minutes to a few hours. The problem concerns the assessment of accuracy, and thus, suitability of various types of commercially available automatic rain gauges: a tipping bucket type, such as the rain gauge RG 50 by SEBA (approved by The World Meteorological Organization – WMO) applied since 2007 in the observation network of IMGW in Poland [7] but also a scale or laser type – all of practical time resolution of one minute. Furthermore, this paper refers to papers [8–10] describing and comparing the accuracy of various types of rain gauges, including state of art measurement devices such as an electronic scale rain gauge OTT Pluvio² or a laser disdrometer Parsivel.

2. RESEARCH MATERIAL AND RESULTS OF MEASUREMENT

2.1. THE RECORD OF SEASONAL AND MONTHLY PRECIPITATION AMOUNTS

The analysis of accuracy of recording by means of a traditional float pluviograph (clock-driven) and a new generation pluviograph of a tipping bucket type (SEBA) in comparison to traditional Hellmann's rain gauge was carried out based on data from the IMGW meteorological station in Legnica (the station coordinates: 51-12 N, 16-13 E; altitude: 122 m above sea level; normal precipitation: 515 mm). Simultaneous measurements of precipitation amounts by means of the three various rain gauges

were carried out in the pluviometric season from May to October of 2009. The measurement devices were located on the site of the metrological station according to requirements in force that is, spaced in the distance of 2 ms between rain gauges. The measurements were taken on the height of 1 m above the ground (Fig. 1).



Fig. 1. Rain gauges in the IMGW meteorological station in Legnica (from left): a float and tipping bucket SEBA type, pluviographs and Hellmann's rain gauge (photo by J. Jadach)

In the entire measurement season from May to October of 2009, the total precipitation amount measured with rain gauges was similar (Table 1). However, the highest amount of precipitation of 472.3 mm was measured by means of Hellmann's rain gauge (the result was assumed to be 100%), average results of 469.9 mm ($P/H = 99.5\%$) were obtained with the float pluviograph, while the lowest results of 467.3 mm ($S/H = 98.9\%$) were given by the tipping bucket pluviograph SEBA. The highest absolute difference of measurement results amounted to 5.0 mm for the SEBA pluviograph, which differs by 1.1% from indications of Hellmann's rain gauge. The precipitation amount given by the float pluviograph was lower by 2.4 mm from indication of the traditional rain gauges, that is, was different by 0.5%.

The highest monthly precipitations occurred in June 2009, slightly exceeding 140 mm, while the lowest rainfall appeared in September, reaching slightly over 11 mm. By analyzing precipitation amounts measured in particular months, one can see a noticeable pattern in deviations of precipitation sums (Table 1). For example, Hellmann's rain gauge showed the highest precipitation amount sums in June – assumed being 100%, while the remaining devices indicated slightly lower values: 99.2% with the float pluviograph and 99.9% with SEBA. Only in May of 2009 for the float pluviograph and in August for both pluviographs, the measured precipitations were higher than for Hellmann's rain gauge (by the maximum of 2.3%). The highest

percentage deviations of monthly sums of precipitation amounts for both compared pluviographs with respect to a traditional rain gauge did not exceed $\pm 2.6\%$.

Table 1

Totals of monthly precipitations (in mm) and their deviations from Hellmann's rain gauge (100%) for the IMGW in Legnica from May to October of 2009

Month	Hellmann's rain gauge (H)	Float pluviograph (P)	P/H [%]	Pluviograph SEBA (S)	S/H [%]
May	81.5	82.1	100.7	79.7	97.8
June	141.4	140.3	99.2	141.3	99.9
July	126.3	124.9	98.9	124.0	98.2
August	52.3	53.5	102.3	52.4	100.2
September	11.5	11.2	97.4	11.2	97.4
October	59.3	57.9	97.6	58.7	99.0
Season May–October	472.3	469.9	99.5	467.3	98.9

Considering the nature of precipitation, especially its diversity of intensity in time and space, the analysis of operation of a device for recording precipitation amounts (with a constant recording) can be regarded equally accurate – equivalent.

2.2. RECORDING DAILY PRECIPITATION AMOUNTS

The number of days with precipitation (≥ 0.1 mm) indicated by the three rain gauges in the entire analyzed season was similar and amounted to 90 days according to the float pluviograph and 91 days according to the other rain gauges. The daily sums of precipitation amounts (in mm) recorded in June 2009 at the IMGW station in Legnica and their deviations (in %) in relation to Hellmann's rain gauge (whose indications were assumed to be 100%) were given in Table 2. The deviation of daily precipitation amounts for 16 rainy days in July for both pluviographs reached a similar level: $P/H \in [92.3; 166.7]\%$ and $S/H \in [88.9; 114.3]\%$, and on average for the entire month: $P/H = 98.9\%$ and $S/H = 98.2\%$. The highest values of relative differences concern mainly small precipitation amounts – within accuracy limits of the devices or the record readouts alone.

The maximum daily sum of precipitation amounts in the entire analyzed season occurred on 7 July 2009 and reached for particular rain gauges (Table 2): Hellmann's rain gauge – 45.2 mm (100%), the float pluviograph – 43.9 mm ($P/H = 97.1\%$) and the tipping bucket pluviograph SEBA – 42.2 mm ($S/H = 93.4\%$). These are deviations in the order of 3% and 7%, respectively – in relation to Hellmann's rain gauge. The

SEBA pluviograph is slightly less accurate in comparison to the traditional tipping bucket pluviograph for very high daily rainfall.

For example, the precipitation patterns for maximum daily rainfall on 7 July 2009 on both pluviograms are seemingly identical, however, those obtained with the SEBA pluviograph are understated by approximately 4% (43.9 mm and 42.2 mm). Considering all results of investigations – comparisons made so far for longer periods of time, the SEBA pluviograph can be recognized as sufficiently accurate and roughly equal to the traditional float pluviograph. It certainly falls into the accuracy class for the description of the investigated phenomenon, also for the period of twenty four hours (in relation to indications of Hellmann's rain gauge). However, the SEBA pluviograph shows significant inaccuracies for short durations (up to 6 h) of very intensive rainfall.

Table 2

Sums of daily precipitations (mm) in July 2009 and their deviations (%) in relation to Hellmann's rain gauge (100%) for the IMGW station in Legnica

Date	Hellmann's rain gauge (H)	Float pluviograph (P)	P/H [%]	SEBA pluviograph (S)	S/H [%]
2 July	0.7	0.8	114.3	0.8	114.3
4 July	18.6	18.6	100.0	19.3	103.8
5 July	0.9	1.1	122.2	0.8	88.9
7 July	45.2	43.9	97.1	42.2	93.4
8 July	2.5	2.4	96.0	2.3	92.0
10 July	9.3	8.7	93.5	8.5	91.4
11 July	2.6	2.4	92.3	2.7	103.8
15 July	2.8	2.8	100.0	2.8	100.0
18 July	19.4	19.2	99.0	19.4	100.0
19 July	0.3	0.5	166.7	0.3	100.0
20 July	2.8	2.8	100.0	2.9	103.6
21 July	1.0	1.0	100.0	1.0	100.0
23 July	10.6	11.1	104.7	11.3	106.6
24 July	5.5	5.5	100.0	5.5	100.0
25 July	3.1	3.1	100.0	3.1	100.0
28 July	1.0	1.0	100.0	1.1	110.0
Total in July	126.3	124.9	98.9	124.0	98.2
The share of the total in the May–October season [%]	26.7	26.5	–	26.6	–

It follows from the comparison of accuracy of other state rain gauges, that is, the electronic scale rain gauge OTT Pluvio² and laser disdrometer Parsivel, mutual dis-

crepancies in recording daily precipitation sums can reach even 50%, which was demonstrated elsewhere [10].

2.3. THE RECORDING OF INTERVAL AMOUNTS OF SHORT TERM RAINFALLS

The development of traditional (paper) pluviographs to record precipitation patterns in short periods ranging from 1 min up to 360 min give raise to a number of difficulties. A basic scale of a pluviogram strip covers hour sections divided into six 10 min parts. Readouts of rainfall amounts in one hour intervals are applied in traditional pluviographic studies [11]. Such accuracy is unacceptable in the assessment of short term rainfall (especially including durations of 5, 10, 15, 30 or 45 min). The basic scale of a pluviogram strip allows isolation of rainfall fragments of durations shorter than 10 min. In practice, it is possible to determine precipitations (accurately enough) in the minimum 5 min intervals. Data for shorter periods would be burdened with high readout inaccuracy, both for precipitation amount and isolation of successive minutes of its duration. However, the development of 5 min intervals brings a certain inconvenience of forcing constant time intervals: 1–5, 6–10, 11–15, ..., up to 56–60 min. Furthermore, such a manner of isolation and interpretation of interval precipitation amounts in constant 5 min intervals may make it impossible to capture the maximum rainfalls in specified (short) durations. Technically, the isolation of 5 min progressing-rolling intervals (changeable [12]), which begin and end on successive minutes is more difficult, even when using graphical enlargements of described pluviogram fragments. However, the latter method – in isolation from constant 5 min time intervals applied on the basic pluviogram scale – is more suitable for interpretation of measurement results (physically correct).

The situation is fundamentally changed in the case of the electronic recording of precipitation patterns in meteorology. In automatic pluviographs, such as SEBA (currently used in the IMGW network), the precipitation recording is carried out for each emptying of a tipping bucket of a small volume, whereas the tipping time is recorded with the accuracy of a second. Such a recording method makes it possible to specify precipitation amounts for any time intervals. Thus, two methods of the determination of the maximum 5 min rainfall sums can be used to develop precipitation patterns from SEBA pluviograms: the former – for constant 5 min time intervals and the other – for 5 min rolling intervals beginning in successive minutes of actual precipitation durations. As will be shown, the latter method yields more correct results, especially for shorter periods of time being analyzed.

The total of 40 days with precipitation of ≥ 5.0 mm, including 13 days with precipitation of ≥ 10.0 mm (according to Hellmann's rain gauge) were recorded in the Legnica station in the analyzed period from May to October 2009. The example of developed results for 10 selected cases of the highest rainfall – with the daily amount of

≥ 10.0 mm and duration up to 360 min is shown in Table 3. The development of pluviogram readouts for precipitations in 10 selected periods of time (5, 10, 15, 30, 45, 60, 90, 120, 180 and 360 min) was carried out separately for the float (clock) pluviograph and the tipping bucket pluviograph SEBA. Additional precipitation amounts in the interval of 1 min were specified for the SEBA electronic pluviograph, while the two mentioned methods for the development of pluviograms were used in the remaining time intervals, that is, readouts with constant time intervals (results: SEBA-1) and changeable intervals (results: SEBA-2).

The analysis of data presented in Table 3 allows formulation of the following conclusions – statements referring to the differences in recorded precipitations by comparing pluviographs:

- Mutual differences of interval precipitations for the developed rainfall durations from 5 to 360 min do not show a unique pattern, the advantage of precipitation amounts determined from the float pluviograph for the highest rainfall (on 7 July 2009) is only noticeable.
- Differences in interval precipitation amounts for the float pluviograph and the tipping bucket pluviograph SEBA at identical, constant durations reached the maximum of 3.3 mm (in minus) in the 5 min interval and the minimum of 1.5 mm in the 360 min interval (results: SEBA-1, Table 3, Fig. 3).
- Differences in interval precipitation amounts for the float pluviograph and the tipping bucket pluviograph SEBA at changeable intervals of rainfall durations were lower and reached the maximum of 2.3 mm (in minus) in the 5 min interval and the minimum of 1.5 mm in the 360 min interval (results: SEBA-2, Table 3, Fig. 3).
- Totals of short term precipitations determined based on digital records from the SEBA pluviograph at constant and changeable time intervals of rainfalls differed by the maximum of 2.4 mm in the 5 min interval, whereas the determined differences did not exceed ± 1.0 mm (tab. Table 3) in the remaining time intervals.
- The maximum one minute precipitation amount read out from the SEBA pluviograph amounted to 3.6 mm (on 7 July 2009).

Figure 3 illustrates mutual quantitative differences of interval precipitation amounts for the float pluviograph and SEBA pluviograph – for results SEBA-1 and SEBA-2, developed from pluviograms from 7 July 2009.

As was stated above, the highest differences between results of measurements of precipitation amounts concern mostly the first interval of their duration – 5 min (Table 3). In the case of a very intensive (high) rainfall reaching ca. 15 mm during 5 min (as on 7 July 2009), the difference of 2–3 mm indicates the underestimation of the precipitation amount of 10–20%. It should be emphasized that short and intensive rainfall pose a danger for functioning of sewage systems. Thus, the underestimation of 20% should be considered significant, hence further improvement of rainfall measurement instruments and methods is appropriate, especially for short durations, and essential for designing sewage systems.

Table 3

The breakdown of the highest precipitation amounts of durations from 1 to 360 min for the IMGW station in Legnica from May to October 2009^a

Day	Rain gauge ^b	Rainfall sum [mm]	Rainfall occurrence		Duration [min]	Rainfall duration intervals [min]										
			Beginning	End		1	5	10	15	30	45	60	90	120	180	360
1	2	3	4	5	6	7	8	9	10	11	12	13	14	15	16	17
20–21 May	Hellmann's pluviograph	15.5 15.7														
	SEBA-1	15.3					2.8	4.3	4.6	5.8	5.9	5.9	5.9	7.3	9.8	15.4
	SEBA-2	15.3	01-50	06-16	266	1.2	3.4	3.9	4.4	5.5	5.6	5.6	5.6	7.2	9.7	14.8
	SEBA-1	15.3	01-50	06-16	266	1.2	3.4	3.9	4.4	5.5	5.6	5.6	5.6	7.3	9.8	14.8
15 June	Hellmann's pluviograph	19.7 19.7														
	SEBA-1	20.5					1.8	2.9	3.8	5.6	6.7	9.0	11.9	12.8	13.1	
	SEBA-2	20.5	17-32	20-24	167	0.5	1.9	3.1	4.0	6.0	7.4	9.4	12.1	13.1	13.4	
	SEBA-1	20.5	17-32	20-24	167	0.5	1.9	3.1	4.0	6.0	7.4	9.4	12.1	13.1	13.4	
24 June	Hellmann's pluviograph	14.8 14.8														
	SEBA-1	15.4					0.9	1.7	2.1	3.0	4.0	4.3	6.6	8.1	11.2	14.4
	SEBA-2	15.4	16-26	21-58	332	0.4	1.1	1.8	2.2	3.0	4.1	4.4	6.8	8.0	11.7	15.3
	SEBA-1	15.4	16-26	21-58	332	0.4	1.1	1.8	2.2	3.0	4.1	4.5	6.8	8.1	11.8	15.3
25 June	Hellmann's pluviograph	18.1 17.8														
	SEBA-1	18.4					5.0	6.9	7.0	7.2	7.3	7.3	8.3	8.5	13.0	16.1
	SEBA-2	18.4	11-26	17-50	384	1.3	4.6	7.0	7.3	7.3	7.3	7.3	8.6	8.6	13.5	16.8
	SEBA-1	18.4	11-26	17-50	384	1.3	4.6	7.0	7.3	7.3	7.3	7.3	8.6	8.6	13.5	16.8
04 July	Hellmann's pluviograph	18.6 18.6														
	SEBA-1	19.3					1.9	3.3	4.3	6.0	8.1	8.7	10.8	13.3	15.4	17.7
	SEBA-2	19.3	00-56	04-50	234	1.0	3.0	4.3	5.4	7.3	8.8	9.4	11.8	14.7	16.8	19.2
	SEBA-1	19.3	00-56	04-50	234	1.0	3.0	4.3	5.4	7.3	8.8	9.4	11.8	14.7	16.8	19.2
07 July	Hellmann's pluviograph	45.2 43.9														
	SEBA-1	42.2					16.7	25.8	28.8	31.8	33.9	34.5	36.3	37.2	38.6	40.2
	SEBA-2	42.2	18-20	22-55	275	3.6	14.4	23.5	26.8	29.5	31.7	32.4	34.3	35.2	36.9	38.7
	SEBA-1	42.2	18-20	22-55	275	3.6	14.4	23.5	26.8	29.5	31.7	32.4	34.3	35.2	36.9	38.7

Table 3 continued

1	2	3	4	5	6	7	8	9	10	11	12	13	14	15	16	17
18 July	Hellmann's	19.4														
	Pluviograph	19.2					2.8	5.0	6.1	7.1	8.3	8.9	10.9	13.1	15.1	17.9
	SEBA-1	19.4					4.1	5.3	6.1	7.2	8.3	8.9	11.3	13.3	15.3	18.2
	SEBA-2	19.4	14-25	19-21	296	0.9	4.1	5.4	6.4	7.3	8.4	9.0	11.3	13.4	15.4	18.2
23 July	Hellmann's	10.6														
	Pluviograph	11.1					6.1	8.7	9.6	10.1	10.2	10.2	10.2	10.2	10.4	11.1
	SEBA-1	11.3					3.5	6.8	9.2	10.4	10.5	10.5	10.5	10.5	10.7	11.3
	SEBA-2	11.3	16-51	21-45	294	2.0	5.9	7.8	9.5	10.4	10.5	10.5	10.5	10.5	10.7	11.3
02 August	Hellmann's	13.6														
	Pluviograph	13.3					0.8	1.5	2.1	4.0	5.7	7.1	9.2	9.9	10.2	
	SEBA-1	13.7					0.8	1.6	2.3	4.3	5.8	7.3	9.6	10.2	10.5	
	SEBA-2	13.7	00-10	03-29	199	0.2	0.8	1.6	2.4	4.3	5.8	7.3	9.6	10.2	10.5	
10 August	Hellmann's	11.5														
	Pluviograph	11.9					1.7	2.4	2.6	2.8	3.3	4.0	5.8	7.2	8.7	8.9
	SEBA-1	11.5					1.2	2.2	2.4	2.7	3.3	4.0	5.4	6.8	8.5	8.8
	SEBA-2	11.5	22-14	01-43	209	0.4	1.6	2.2	2.5	2.7	3.3	4.0	5.5	6.8	8.6	8.8

^aThe rainfall sum also covers precipitation occurring beyond the described period; the time of rainfall beginning and end is given according to indications of the SEBA rain gauge.

^bSEBA-1 – for constant intervals of rainfall duration (1–5, 6–10, 11–15, ..., 56–60 min.), SEBA-2 – for progressing intervals.

Differences in recorded precipitations in the analyzed self-recording pluviographs are clearly visible in relation to indications of Hellmann's rain gauge, especially for short and intensive rainfalls, which occur rather seldom, but are essential in the process of dimensioning of sewage systems. The differences can be invoked by a number of causes. In the case of a float (clock) pluviometer during intensive rainfall, a certain part of precipitation is not recorded, when the storage container is emptied by means of a siphon. This results in a not entirely vertical diagram on a pluviogram, recording the moment of the float drop in the container which distorts measured total precipitations. In electronic recorders, precipitation losses may occur, when tipping buckets are dropped and water is splashed. Technical reasons such as irregularity of operation of a clockwork or voltage drops in a power supply battery, clogging of a beaker outlet, inaccurate placement of a pluviogram strip and a number of others (including the resolution of pluviogram scale and line thickness) may also deteriorate results of measurements.

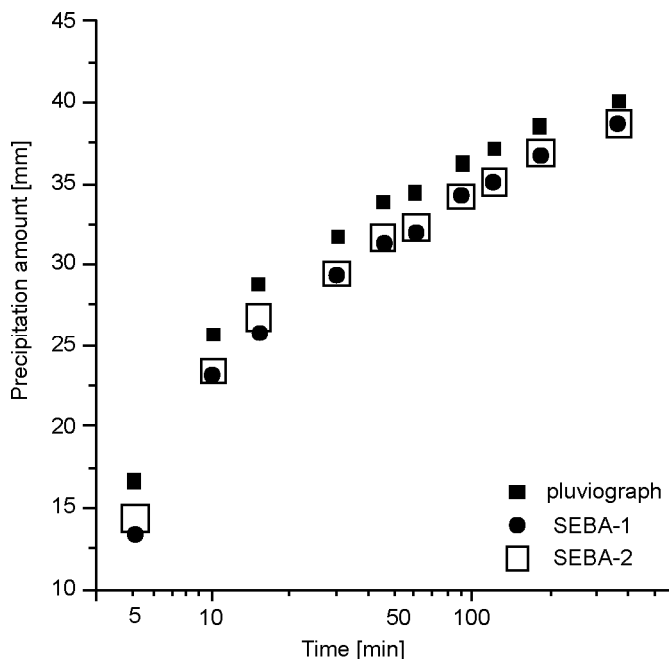


Fig. 2. Interval precipitation amounts for the float pluviograph and SEBA pluviograph; SEBA-1 and SEBA-2 results developed based on the pluviograms dated 7 July 2009

It should be noted that electronic recorders have also their drawbacks. In relation to traditional float pluviographs which may operate in a basically unchanged form for several dozen years and record relatively reliable rainfalls, automatic devices gradually lose adjustment and their indications become unreliable. The recommendation for

carrying out periodical simultaneous rainfall measurements by traditional and electronic pluviographs seems noteworthy, since having switched one's measurement system to electronic recording only, one cannot neglect periodical inspections and calibrations of such instruments based on traditional methods. Thus, obtained results can be compared to previous obtained data.

3. SUMMARY AND CONCLUSIONS

The analysis of accuracy of precipitation measurements using a traditional float pluviograph and a new generation pluviograph of a tipping bucket type (SEBA), in comparison to traditional Hellmann's rain gauge, was based on pluviographic material from the IMGW meteorological station in Legnica from a warm half year (May–October) 2009. The comparison was made for four typical balance periods that is: the May–October season, 1 month, 1 day and 6 hours.

The total precipitation amounts in the entire pluviographic period measured by means of three rain gauges were very close. However, the highest precipitation sum was recorded with Hellmann's rain gauge (100%), medium sums – with a float pluviograph (99.5%), while the lowest values were recorded using a tipping bucket pluviograph SEBA (98.9%). The maximum difference of results (for the SEBA pluviograph) in relation to Hellmann's rain gauge amounted to -1.1%.

A similar deviation pattern of measured rainfall amounts can be noticed from the analysis of monthly precipitations. The highest sums were indicated with Hellmann's rain gauge, while the remaining devices noted slightly lower relative values as a rule. The percentage deviations of monthly precipitation did not exceed $\pm 2.6\%$ both for the SEBA pluviograph and float pluviograph with respect to Hellmann's rain gauge.

Relative average daily sums of precipitation amounts for 16 days with rainfall in July 2009 were characterized by a similar pattern. In a twenty four hour interval with the highest rainfall, the relative precipitation sum was: 97.1% for the float pluviograph and 93.4% for the tipping bucket pluviograph SEBA – with respect to 100% (45.2 mm) for Hellmann's rain gauge. The added up rainfall amounts from self-recording pluviographs were different by approximately 4% to the disadvantage of the SEBA pluviograph for the highest daily rainfall during measurement season.

However, considering the nature of rainfall phenomenon, and especially the diversity of its intensity in time and space, the analyzed device for recording time dependences of precipitations can be recognized sufficiently accurate and approximately equivalent, certainly within the description accuracy class of the investigated phenomenon, especially for long periods of time, such as a season or a month, but also for a day. Nevertheless, the analysis of short term rainfalls – with durations ranging from 1 to 360 min – showed that the highest differences in precipitation amounts, recorded with compared pluviographs, occur mainly in the first 5 min of a rainfall. The mutual

differences of interval precipitation amounts for the float pluviograph and SEBA pluviograph are the lowest, when changeable intervals of precipitation durations are applied to interpret the pluviograms. Mutual differences of the value of 2–3 mm were indicated in the case of very intensive rainfalls reaching ca. 15 mm during 5 min (as on 7 July 2009) which shows an underestimation of the precipitation amounts by 10–20% by the SEBA pluviograph in comparison to the traditional float pluviograph. Short lived and intensive rains are usually dangerous to proper functioning of a sewage system – described in the initial curve sections of the precipitation amount (DDF) or intensity (IDF).

From the analysis carried out and literature data it follows that further improvement of instruments and methods for measurement of precipitation amounts is necessary, since currently used rain gauges, including new generation ones, have a number of flaws.

REFERENCES

- [1] KOTOWSKI A., Forum Ekspl., 2006, 1, 18.
- [2] KOTOWSKI A., Gaz, Woda Techn. Sanit., 2006, 6, 20.
- [3] KOTOWSKI A., *The discussion of recommendations of PN-EN 752 standard related to the rules for drainage area sizing in Poland*, [In:] Monogr. Environmental Engineering Committee PAS, 2007, 46, 27 (in Polish).
- [4] LICZNAK P., Gaz, Woda Techn. Sanit., 2009, 6, 19.
- [5] GAO J., CAO Y., TUNG W., HU J., *Multiscale analysis of complex time series, Integration of chaos and random fractal theory, and beyond*, Wiley, New Jersey, 2007.
- [6] LOVEJOY S., SCHERTZER D., J. Hydrol., 2006, 322, 59.
- [7] KOTOWSKI A., KAŽMIERCZAK B., DANCEWICZ A., *The modeling of precipitations for sewer system dimensioning*, [In:] Publ. Committee of Civil Engineering PAN, Institute of Fundamental Technological Research, Engineering Studies, No. 68. Warsaw,, 2010 (in Polish).
- [8] LEDNICKÝ V., PRIADKA O., *The comparison of measurement accuracy of different types of rain gauges*, [In:] Meteorologické Zprávy, ČHMÚ Praha, 1984, No. 1, 21–23.
- [9] LICZNAK P., ŁOMOTOWSKI J., ROJEK M., *Measurements and precipitation data processing for the designing and use of drainage systems*, FUTURA, Poznań, 2005 (in Polish).
- [10] LICZNAK P., Instal., 2009, 7–8, 43.
- [11] JANISZEWSKI F., Gazeta Obserwatora, 1976, 2–3, 7.
- [12] BOGDANOWICZ E., STACHY J., *Maximum rainfall in Poland. Design characteristics*, [In:] Hydrology and Oceanology, No. 23. Institute of Meteorology and Water Management, Warsaw, 1998 (in Polish).

ANDRZEJ BIELSKI*

MODELLING OF MASS TRANSPORT IN WATERCOURSES CONSIDERING MASS TRANSFER BETWEEN PHASES IN UNSTEADY STATES. PART I. MASS TRANSFER PROCESS FOR PERIODIC AND APERIODIC CHANGES OF CONCENTRATION

A model most often used for the description of the processes of mass transport through phase boundaries is the model of Whitman. Results of calculations obtained using this model may occasionally considerably differ from the results obtained using diffusion models. Thus an attempt has been made to correct the model proposed by Whitman. The dynamics of the processes of mass transport from a liquid phase (river water) to a solid phase (layer of material in the river bottom) has been analysed. Several equations have been derived describing the rate of absorption with a chemical reaction and periodical changes of the concentration of the analysed substance. An attempt has been made to determine the relation between the concentration gradient and concentration at the phase boundary. In dynamic conditions, the concentration gradient at the phase boundary can be approximated by means of time dependence of a linear combination of concentration, delayed concentration, and concentration derivative at the phase boundary. Analysis of the dynamics of the absorption process with the chemical reaction enabled one to derive an equation describing the stream of the substance penetrating to the inside of the solid phase. Such equations may be used to determine the error generated by the film model of Whitman for the process of mass penetration.

1. INTRODUCTION

More and more complex models have been developed to describe propagation of various kinds of substances in water environment. The models take into consideration transformation rates of substances as well as rates of their interactions with other components of the environment. Therefore, it is possible to describe, in a more accurate way, the actual processes to which the substances are subjected as well as to determine exact substance quantities in a definite place and time. All the models require that numerical values of some parameters be identified; more elaborate models require

*Cracow University of Technology, Department of Environmental Engineering, Warszawska 24, 31-155 Cracow, Poland. E-mail: abielski@riad.usk.pk.edu.pl

more parameters to be known. Identification of numerical values of the parameters is usually not easy. Most of the time both specific field investigations and laboratory tests are required. Some investigations and tests allow one to identify just one parameter while in the case of other parameters simultaneous determination of several numerical values is required. Such parameters include: motion resistance coefficient of a flow wave, coefficient of mass dispersion, rate constants of chemical or physical processes that influence that substance.

If biochemical, chemical and physical process rates are considered, appropriate kinetic equations have to be developed. Since the mass transport model for unsteady states (flows varying in time) is very complicated, kinetic equations should remain rather simple. It should be noted however that too much simplifications may result in poor model accuracy. Particularly demanding, in terms of good qualitative description, are processes of mass exchange between different phases (e.g.: atmospheric air–water, water–river sediment, water–algae etc.).

The Whitman model has been most frequently used for description of mass transport through a phase boundary [5, 8, 10, 11]. Results of calculations based on this model may occasionally considerably differ from the results obtained using diffusion models. The differences may be explained by concentration profiles directed along diffusion which are time dependent. Since the Whitman model does not consider such dependences, an attempt to improve the Whitman model has been made.

Kinetics of mass transport in sorption processes may be described by the pseudo second order model [3, 4, 6, 9], however it is useless for desorption processes, because the model does not provide possibility to change the sign of process rate. Consideration of adsorption-absorption effect in mass transport equations needs occasionally some modifications. In the paper, several equations will be derived taking into consideration adsorption-absorption effects, which influence mass transport in natural water systems.

Diffusion processes may be accompanied by chemical and biological ones. The rate of biological and chemical processes proceeding in a separate phase may have a major impact on the concentration of a substance in the liquid phase (water). Therefore, a number of new equations will be derived describing total diffusion rate of a substance into a separate phase accompanied with a simultaneous chemical reaction. The paper focuses on the problems of adsorption-absorption rates in unsteady states.

At the beginning, the concepts of: liquid phase (water) and solid phase (river sediment, e.g. mineral solids, organic solids, rock material, water bound in a sediment, etc.) have been defined. Then it was assumed that the solid phase consists of two compounds where either an adsorption process or chemical/biochemical processes take place but never both these processes occur simultaneously. It was also assumed that no mass transfer occurs between two compounds of the solid phase, and the adsorption refers only to mineral or organic solids deposited at the bottom of the river. On the other hand, absorption refers to water bound in material deposited at the bottom sediment.

It was also assumed that characteristic of river bottom material does not change in time (neither new sediment layers are built up nor erosion proceeds) and there is no water motion in river sediments. Moreover, accumulation of mass of the analyzed substance in cells of microorganisms present in both liquid and solid phases is ignored.

2. DIFFUSION MASS TRANSPORT WITHIN A PHASE

Diffusion of a substance of concentration C accompanied with a chemical or biochemical reaction in a solid phase of a watercourse following monomolecular first order mechanism is expressed by:

$$\frac{\partial C}{\partial t} = D \frac{\partial^2 C}{\partial y^2} - k_r C, \quad (1)$$

where the coordinate y is the distance from the phase boundary in the solid phase.

Let us assume for the solid phase:

- initial conditions:

$$C(t=0, y) = 0, \quad (2)$$

$$C(t, y=0) = C_i; \quad (3)$$

- boundary conditions:

– for a layer of unlimited thickness

$$C(t, y \rightarrow \infty) = 0, \quad (4a)$$

– for a layer of thickness L

$$\left. \frac{\partial C}{\partial y} \right|_{t, y=L} = 0. \quad (4b)$$

It is hard to precisely determine the thickness of a bottom sediment layer where diffusion process takes place; in theory, the layer may be of any thickness. It was assumed that the analyzed layer would have such thickness that the concentration distribution within the layer would be similar to the distribution in the layer of an infinite thickness.

Solution of Eqs. (1) with conditions: (2), (3), (4a) in the form of Laplace transformation is as follows:

$$\hat{C} = \frac{C_i}{s} \exp\left(-\sqrt{\frac{s+k_r}{D}} y\right), \quad (5)$$

whereas for conditions: (2), (3), (4b), the solution of Eq. (1) takes the form:

$$\hat{C} = \frac{C_i}{s} \frac{\exp\left(-\sqrt{\frac{s+k_r}{D}}y\right)}{1+\exp\left(-\sqrt{\frac{s+k_r}{D}}L\right)} + \frac{C_i}{s} \frac{\exp\left(-\sqrt{\frac{s+k_r}{D}}(2L-y)\right)}{1+\exp\left(-\sqrt{\frac{s+k_r}{D}}L\right)}, \quad (6)$$

where $y \in <0, L>$.

If only the thickness of a layer L is large enough and the concentration distribution next to the phase boundary ($y \ll L$) is examined, Eq. (6) may be approximated with the solution (5). If a complex variable s is substituted with a product: $I\omega$ ($I=\sqrt{-1}$), the transmittance $G = \hat{C}/\hat{C}_i$ can be calculated from Eqs. (5) and (6) as well as corresponding modules $|G|$ (coefficients of attenuation of a concentration amplitude M) and arguments $\arg(G)$ (phase shift φ) [7].

Assume that periodic changes of concentrations C_i at the phase boundary are represented by the function expanding in a trigonometric series in a form of:

$$C_i = \frac{1}{2} A_0 + \sum_{n=1}^{\infty} [A_n \sin(n\omega) + B_n \cos(n\omega)], \quad (7)$$

$$\omega = \frac{2\pi}{T}, \quad (8)$$

where: $(1/2)A_0$ is the average value of concentration C_i , A_n , B_n – the coefficients of trigonometric series, T – period of the concentration function C_i .

In such a case, stabilized changes of concentrations within the layer can be expressed by the following equation:

$$C(y, t) = \frac{1}{2} A_0 M(\omega=0) + \sum_{n=1}^{+\infty} \left\{ M(n\omega) \left[A_n \sin(n\omega + \varphi(n\omega)) + B_n \cos(n\omega + \varphi(n\omega)) \right] \right\}, \quad (9)$$

where:

$$M(\omega=0) = |G(\omega=0)|, \quad (10)$$

$$M(n\omega) = |G(n\omega)|, \quad (11)$$

$$\varphi(n\omega) = \arg(G(n\omega)). \quad (12)$$

When stabilized changes in time occur inside layers of unlimited size and the thickness L , concentration distributions calculated based on Eq. (9) would be similar in these locations where values M and φ are similar [1]. Based on a theoretical analysis of transmit-

tance, one may conclude that the concentration curves get close to each other upon L increasing, decreasing period T and increasing process rate constant k_r [1]. Further discussion focuses on layers for which Eq. (5) is valid.

3. CONCENTRATION GRADIENT AT A BOUNDARY OF LIQUID AND SOLID PHASES AT UNSTEADY STATES

Let us assume that changes of concentration C_i are stabilized in time at the phase boundary. They can be written as:

$$C_i = C_{i,m} + C_{i,a} \sin(\omega t), \quad (13)$$

where: $C_{i,m}$ – average concentration at the phase boundary, $C_{i,a}$ – concentration amplitude at the phase boundary, $\omega = 2\pi/T$, T is the period of the concentration wave.

If Laplace transformation is \hat{C}_i and the concentration at the phase boundary is C_i ($y = 0$) Eq. (5) may be written in a form:

$$\frac{\hat{C}}{\hat{C}_i} = G(s) = \exp\left(-\sqrt{\frac{s+k_r}{D}}y\right). \quad (14)$$

Equation (14) is a transmittance $G(s)$ of a solid phase that links the concentration transform at the phase boundary \hat{C}_i with the concentration transform \hat{C} inside the phase. In order to pass from a complex domain of Laplace transformations to a frequency domain it is necessary to substitute $s = I\omega$ [7] and then transmittance G will be expressed as:

$$G(I\omega) = \exp\left(-\sqrt{\frac{I\omega+k_r}{D}}y\right). \quad (15)$$

The module $M(y, \omega)$ and the argument $\varphi(y, \omega)$ of the transmittance G are:

$$M(y, \omega) = |G(I\omega)| = \exp\left(-\sqrt{\alpha_M} \cos(\gamma_M)\right), \quad (16)$$

$$\begin{aligned} \varphi(y, \omega) &= \arg(G(I\omega)) = \arctg \left[\frac{\sin(-\sqrt{\alpha_M} \sin(\gamma_M))}{\cos(-\sqrt{\alpha_M} \sin(\gamma_M))} \right] \\ &= \arctg \left[\operatorname{tg}(-\sqrt{\alpha_M} \sin(\gamma_M)) \right] = -\sqrt{\alpha_M} \sin(\gamma_M). \end{aligned} \quad (17)$$

(Note the sign of sine and cosine functions while determining argument φ).

$$\alpha_M = \frac{y^2}{D} \sqrt{k_r^2 + \omega^2}, \quad (18)$$

$$\gamma_M = \frac{1}{2} \operatorname{arctg} \left(\frac{\omega}{k_r} \right). \quad (19)$$

(There are two roots of a complex number $k_r + I\omega$. Since the second root ($\gamma_M + \pi$) represents modules $M(y, \omega) \geq 1$, it will not be considered in this case. Due to the presence of a diffusive resistance of mass transport, and since the amount of substance decreases due to the chemical reaction, $M(y, \omega) \leq 1$).

Knowing both the module and argument of transmittance, equation describing changes of concentration within the solid phase [7] may be formulated:

$$C = C_{i,m} M(y, \omega=0) + C_{i,a} M(y, \omega) \sin(\omega t + \varphi(y, \omega)) \quad (20)$$

and the concentration gradient:

$$\begin{aligned} \frac{\partial C}{\partial y} &= C_{i,m} \frac{\partial M(y, \omega=0)}{\partial y} + C_{i,a} \frac{\partial M(y, \omega)}{\partial y} \sin(\omega t + \varphi(y, \omega)) \\ &\quad + C_{i,a} M(y, \omega) \cos(\omega t + \varphi(y, \omega)) \frac{\partial \varphi(y, \omega)}{\partial y}. \end{aligned} \quad (21)$$

Especially at the phase boundary ($y = 0$), the gradient may be determined using the following relationship:

$$\left. \frac{\partial C}{\partial y} \right|_{y=0} = -\sqrt{\frac{k_r^2 + \omega^2}{D}} C_{i,m} + \sqrt{\frac{\sqrt{k_r^2 + \omega^2}}{D}} C_{i,a} \sin\left(-\omega \left(t + \frac{\gamma_M}{\omega}\right)\right). \quad (22)$$

In the case of a sinusoidal change of concentration eq. (13) a concentration gradient described by relationship (22) may also be presented in another equivalent form:

$$\begin{aligned} \left. \frac{\partial C}{\partial y} \right|_{y=0} &= a_1 C_i(t) + a_2 \left. \frac{\partial C_i}{\partial t} \right|_t + a_3 \\ &= a_1 (C_{i,m} + C_{i,a} \sin(\omega t)) + a_2 C_{i,a} \omega \cos(\omega t) + a_3. \end{aligned} \quad (22a)$$

After comparing right sides of Eqs. (22) and (22a) we have:

$$a_1 = -\sqrt{\frac{\sqrt{k_r^2 + \omega^2}}{D}} \cos(\gamma_M), \quad (22b)$$

$$a_2 = -\frac{1}{\omega} \sqrt{\frac{\sqrt{k_r^2 + \omega^2}}{D}} \sin(\gamma_M), \quad (22c)$$

$$a_3 = C_{i,m} \left(\sqrt{\frac{\sqrt{k_r^2 + \omega^2}}{D}} \cos(\gamma_M) - \sqrt{\frac{k_r}{D}} \right). \quad (22d)$$

Time dependences of both concentrations at phase boundary inside the solid phase and of the concentration gradient are presented in Fig. 1. It should be noted that the concentration gradient slightly accelerates (shift in time, type (γ_M/ω) , Eq. (22)) at the phase boundary, if compared with concentration C_i (Fig. 1).

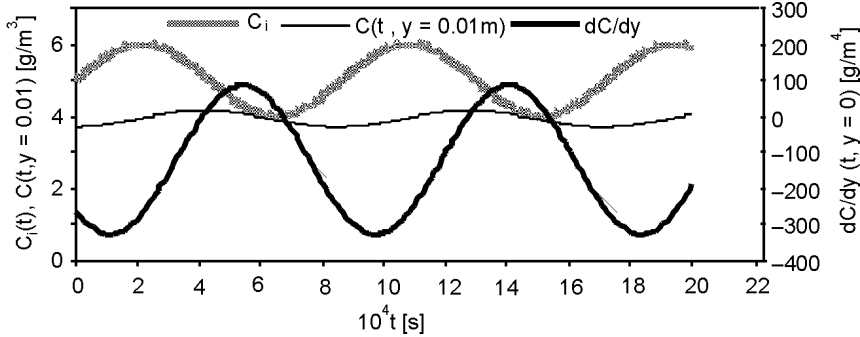


Fig. 1. Time dependences of concentration C_i , concentration gradient $\partial C / \partial y$ at the phase boundary and concentration inside the solid phase $C(t, y = 0.01 \text{ m})$; $k_r = 10^{-6} \text{ s}^{-1}$, $D = 1.7 \times 10^{-9} \text{ m}^2/\text{s}$, $C_{i,m} = 5 \text{ g/m}^3$, $C_{i,a} = 1 \text{ g/m}^3$, $T = 86\,400 \text{ s}$

Equation (22) or (22a) may be used to determine the mass flux of a substance diffusing through the phase boundary to a solid phase, based on the Fick Law [10]:

$$\frac{\partial m}{\partial t} = -DA^* \frac{\partial C}{\partial y}. \quad (23)$$

4. CONCENTRATION CHANGES UNSTABILIZED IN TIME

If changes of concentration of a certain substance do not change in time in a periodic way, the factor defining the value of the concentration gradient in equations describing the mass transfer rate requires modifications. Aperiodic changes of concentration may occur either in the case of occasional pollutant discharges to a watercourse or during tracer experiments, when a specific substance is introduced to a river in an impulse type manner.

In the case of stabilized changes of concentration, it is possible to determine the concentration C in the following moment (shift (γ_M/ω) type, Eq. (22)) just based on the change of concentration in the previous period T . If only a single concentration impulse occurs, determining of the concentration in the following moment is not possible.

An adequate picture of an aperiodic process may be obtained simply through the analysis of penetration into a solid phase when changes of the concentrations follow a function in a form of rectangular impulses. Time lapses between the subsequent concentration impulses next to the phase boundary should be long enough to enable equilibrium between the absorption process and a chemical reaction (Fig. 2).

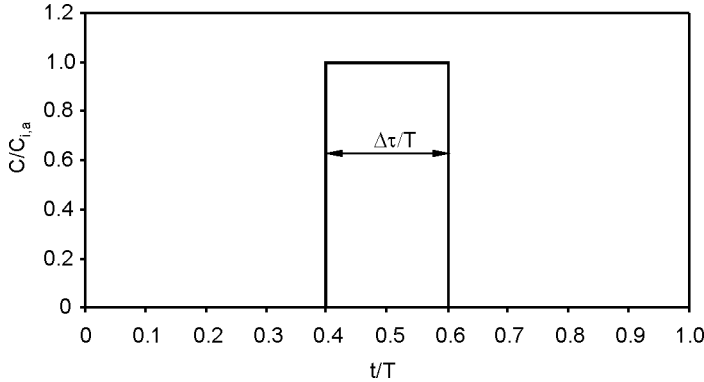


Fig. 2. Rectangular concentration impulse: T – period of function,
 $C_{i,a}$ – amplitude of impulse, $\Delta\tau$ – duration of impulse

Expansion of the function presented in Fig. 2 and symmetric to $t/T = 0.5$ in a trigonometric series is as follows:

$$C = \frac{\Delta\tau}{T} C_{i,a} + \sum_{n=1}^{+\infty} \frac{2C_{i,a}}{n\pi} (-1)^n \sin\left(\frac{n\pi}{T}\Delta\tau\right) \cos\left(\frac{2n\pi}{T}t\right), \quad (24)$$

where: T – period of a function, $C_{i,a}$ – amplitude of an impulse, $\Delta\tau$ – impulse duration, $2\pi/T = \omega_0$ – angular velocity for a main harmonic ($n = 1$, fundamental angular velocity).

Let us recall that Eq. (24) describes changes at the phase boundary. Knowing both module (16) and argument of transmittance (17), an equation may be formulated that describes changes of the concentration within the solid phase [7]:

$$C = M(y, \omega=0) \frac{\Delta\tau}{T} C_{i,a} + \sum_{n=1}^{\infty} M(y, n\omega) \frac{2C_{i,a}}{n\pi} (-1)^n \times \sin\left(\frac{n\pi}{T}\Delta\tau\right) \cos\left(\frac{2n\pi}{T}t + \varphi(y, n\omega)\right). \quad (25)$$

Equations (24) and (25) enable one to determine the concentration gradient at the phase boundary in a numeric way (analytical method makes calculations rather complicated in this case). Dependence of the gradient of concentration ($dC/dy(t)$) on $C_i(t)$ for the case presented in Fig. 1 is an ellipse (Fig. 3).

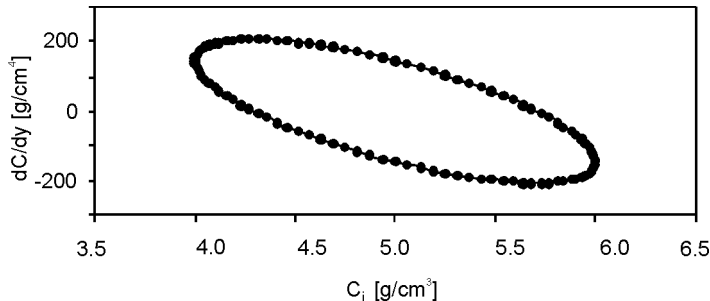


Fig. 3. Concentration gradient vs. concentration at the phase boundary according to $(dC/dy)(t)$ and $C_i(t)$ runs, as presented in Fig. 1

The same dependence developed considering the time lapse $(dC/dy)(t) = f(C_i(t + \Delta t))$ becomes a line segment at $\Delta t = T/8 = 0.125T$ – this is the maximum value (γ_M/ω) at $k_r = 0$ (for the average value of $C_{i,m} = 5 \text{ g/m}^3$ gradient $dC/dy = 0$). In case of $\Delta t = 10\ 368 \text{ s}$ ($\Delta t/T = 0.12$) a distinctly flattened ellipse is obtained (Fig. 4). The concentration gradient at the moment t may be estimated from the value of concentration at the moment $(t + \Delta t)$ or $(t - T + \Delta t)$, when stabilized periodical changes occur, based on the straight line equation. Upon increasing k_r values, the time lapse Δt decreases to zero. In the case of a single concentration impulse or impulses spread long time apart, the dependence of concentration gradient on the concentration is similar to the one described above although not such ideal.

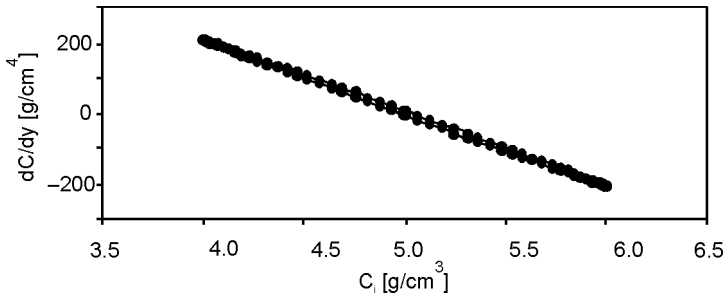


Fig. 4. Concentration gradient vs. concentration at the phase boundary according to $(dC/dy)(t)$ and $C_i(t+\Delta t)$ runs, as presented in Fig. 1 ($\Delta t = 10\ 368 \text{ s}$)

Assume that a series of concentration impulses at the phase boundary is defined using first seven components of the sum in Eq. (24). Concentration runs at the phase

boundary, concentrations at the distance $y = 10^{-6}$ m at the solid phase side and concentration gradients at the phase boundary are presented in Fig. 5. Dependences of concentration gradients on concentration $(dC/dy)(t) = f(C_i(t))$ and $(dC/dy)(t) = f(C_i(t + \Delta t))$ for various Δt are presented in Figs. 6–8.

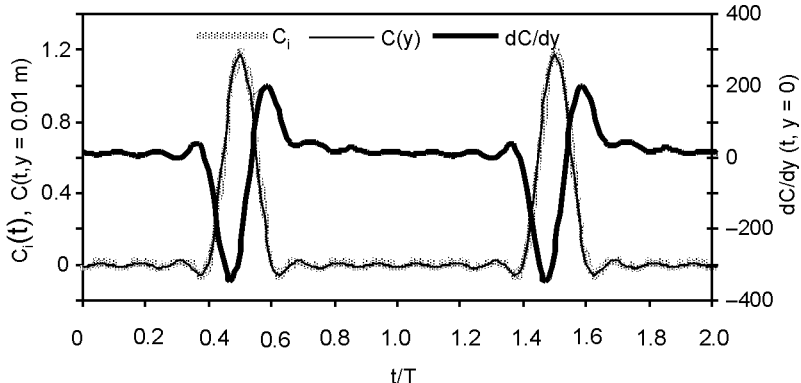


Fig. 5. Concentrations at the phase boundary, concentration at the distance $y = 10^{-6}$ m at the solid phase side and concentration gradient at the phase boundary:
 $T = 86400$ s, $C_{i,a} = 1$ g/m³, $\Delta\tau = T/16$, $k_r = 10^{-30}$ s⁻¹, $D = 1.7 \times 10^{-9}$ m²/s

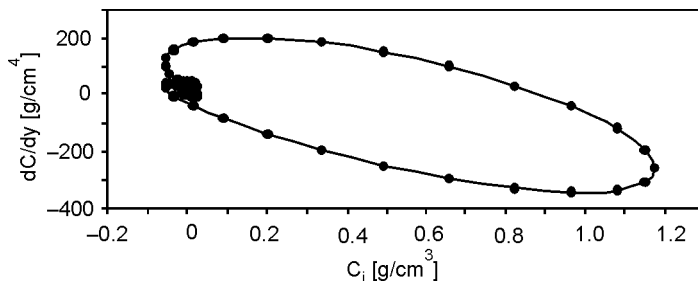


Fig. 6. Concentration gradient vs. concentrations at the phase boundary according to $(dC/dy)(t)$ and $C_i(t)$ runs, as presented in Fig. 5 ($\Delta t = 0$)

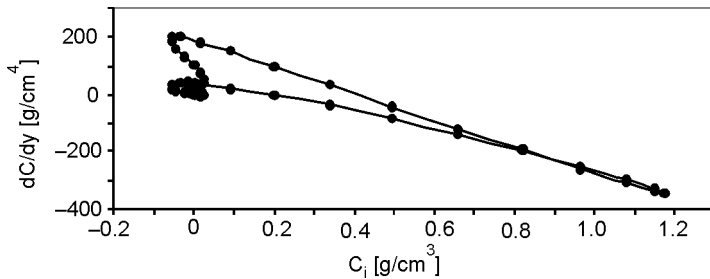


Fig. 7. Concentration gradient vs. concentration at the phase boundary according to $(dC/dy)(t)$ and $C_i(t + \Delta t)$ runs, as presented in Fig. 5 ($\Delta t = 0.03T$)

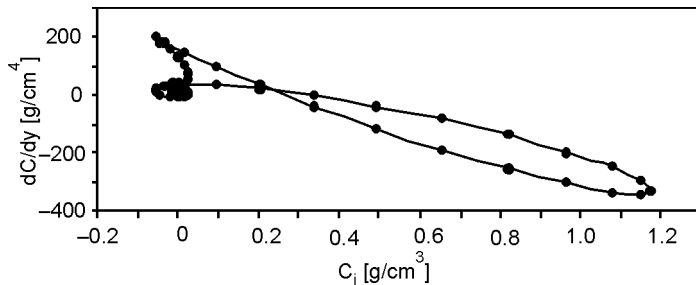


Fig. 8. Concentration gradient vs. concentration at the phase boundary according to $(dC/dy)(t)$ and $C_i(t + \Delta t)$ runs, as presented in Fig. 5 ($\Delta t = 0.04T$)

Plots presented in Figs. 7 and 8 form closed curves that are much more flat than the curve in Fig. 6. Irregular scatter of points close to the concentrations approaching zero is probably caused by oscillations and lack of ideal steady state conditions (Fig. 5).

Numerical experiments confirm that an increase of a chemical process rate constant k_r enhances the effect of flattening of the closed curves. Shapes of curves in Figs. 4, 7 and 8 suggest that the concentration gradient may be approximated by:

$$\frac{dC}{dy} = a'_1 [C_i(t + \Delta t_1) - C_{i,m}] + a'_3 [C_i(t - \Delta t_2) - C_{i,m}] + a'_4, \quad (26)$$

where: a'_1, a'_3 and a'_4 – constants, $\Delta t_1, \Delta t_2$ – time shifts.

Since during a single impulse the subsequent concentration values are not known, their values may be estimated by differentiating the concentration with respect to time:

$$\begin{aligned} \frac{dC}{dy} &= a'_1 \left[C_i(t) + \frac{dC_i}{dt} \Big|_{t_1} \Delta t_1 - C_{i,m} \right] + a'_3 \left[C_i(t - \Delta t_2) - C_{i,m} \right] + a'_4 \\ &= a'_1 C_i(t) + a'_1 \frac{dC_i}{dt} \Big|_{t_1} \Delta t_1 + a'_3 C_i(t - \Delta t_2) + a'_4 \\ &= a'_1 C_i(t) + a'_2 \frac{dC_i}{dt} \Big|_{t_1} + a'_3 C_i(t - \Delta t_2) + a'_4, \end{aligned} \quad (27)$$

where: a_1, a_2, a_3, a_4 – constants.

Calculation of the previous values using a derivative dC_i/dt may not give accurate results when Δt_2 is too high. In the case of an impulse function, its approximated average value $C_{i,m}$ should be assumed zero, since the function is a positive fraction of another function that has been developed as a result of an odd analytical impulse continuation (impulse oscillation around zero). If any oscillation around the non-zero value would occurred, the average value would have varied along the watercourse length (x – linear coordinate). Let us assume that the concentration of the substance in

the core of the liquid phase is equal to the concentration at the phase boundary of liquid and solid phases ($C_i \approx \tilde{C}$). In such a case, the values $C_{i,m}(x)$ should be calculated from appropriate stationary mass transport models referring to a liquid phase. A detailed discussion on this topic has been presented elsewhere [1].

If sinusoidal concentration changes occur (Fig. 1), the theoretical concentration gradient calculated from Eqs. (24) and (25) ($\Delta y = 10^{-6} \text{ m}$) may be precisely approximated with the model (27) (Fig. 9). In this particular case we have:

$$\frac{dC}{dy} = -141.653839581284(C_i(t) - C_{i,m}) - 201.210089726553 \times 10^4 \left. \frac{d(C_i(t) - C_{i,m})}{dt} \right|_t, \quad (28)$$

where $\Delta t = 864 \text{ s}$ is the time step used for numerical calculations of a derivative with respect to time.

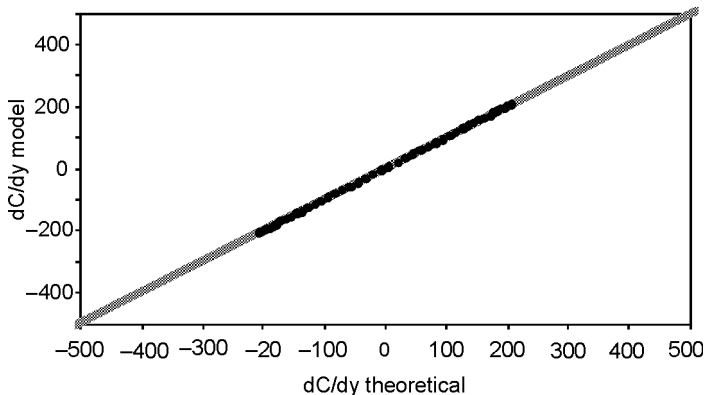


Fig. 9. Fitting of the gradient model (27) to the gradient calculated numerically using Eqs. (24) and (25) (theoretical gradient) for a sine concentration curve, as presented in Fig. 1 (the average absolute error for a single value of gradient is $3.78 \times 10^{-7} \text{ g/m}^4$)

Coefficients of Eq. (28) are approximately equal to the respective theoretical ones: $a_1 = -146.25 \text{ m}^{-1}$, Eq. (22b), $a_2 = -201.11 \times 10^4 \text{ s/m}$, Eq. (22c), $a_3 = 0 \text{ g/m}^4$, Eq. (22d) (a_3 is equivalent of a_4 in Eq. (27); a_3 approaches zero since a difference between concentration and the average was used in calculations).

For an impulse concentration change (Fig. 5), the following equations were obtained:

$$\frac{dC}{dy} = -210.78C_i(t) - 90.27 \times 10^4 \left. \frac{dC_i}{dt} \right|_t + 77.782C_i(t-8640) + 16.718, \quad (29)$$

$$\frac{dC}{dy} = -201.83C_i(t) - 110.46 \times 10^4 \left. \frac{dC_i}{dt} \right|_t + 25.229. \quad (30)$$

Values of the coefficients in Eqs. (29) and (30) were determined after minimizing of a sum of squared deviations between theoretical gradient values, calculated from Eqs. (24) and (25), and the values calculated from the model (27).

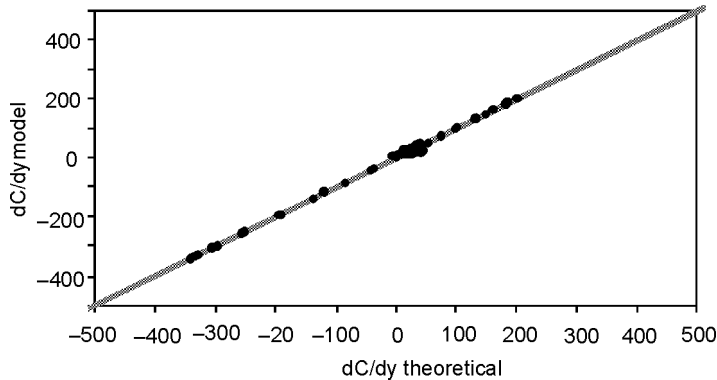


Fig. 10. Fitting of the gradient model (27) to the gradient calculated numerically using Eqs. (24) and (25) (theoretical gradient) for an impulse of concentration, as presented in Fig. 5 (the average absolute error for a single value of gradient is 7.36 g/m^4)

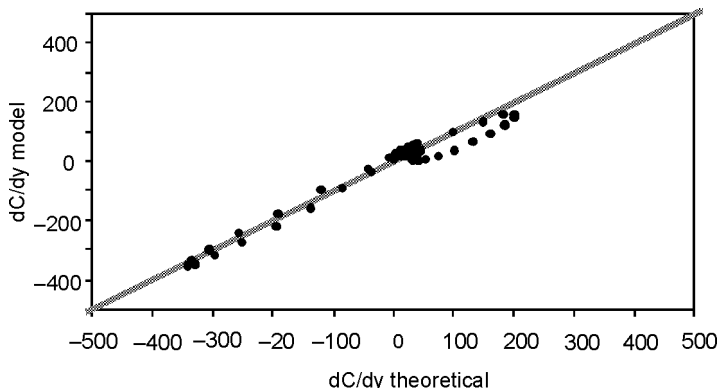


Fig. 11. Fitting of the gradient model (27) to the gradient calculated numerically using Eqs. (24) and (25) (theoretical gradient) for an impulse of concentration, as presented in Fig. 5 (the average absolute error for a single value of gradient is 21.69 g/m^4)

Figures 10 and 11 show the results of gradient calculations from Eqs. (29) and (30), respectively. The equations approximate a theoretical value of gradient with a different accuracy; in practice, poor accuracy of Eq. (30) seems quite sufficient. The equation is much easier to use since it does not require memorizing a series of concentrations delayed with respect to a current time t by Δt_2 in all river cross-sections x_i during numerical solving of the mass transport equation.

In model (27) term a_4 is responsible for a substance desorption for a single concentration impulse and its value is proportional to the average desorption rate. Due to desorption from a solid phase, some concentrations in a liquid phase remain different from zero, irrespective of time of impulse duration. Such an effect is a consequence of the assumption that a series of concentration impulses at the phase boundary is described using seven first elements of the sum in Eq. (24).

During identification of the mass transport model, based on the concentration measurements of a tracer fed into a watercourse in an impulse-type mode and using Eq. (27), it is necessary to introduce some complementary functions. The functions depend on such parameters as distance coordinate x , time t and tracer hydraulic detention time; all the parameters attenuate a desorption effect related to the value of the coefficient a_4 ($a_4 \neq 0$) [2]. Equations like (27) may also be used in models describing both absorption and desorption with a chemical reaction in a solid phase. [2].

4. SUMMARY AND CONCLUSIONS

The first part of the paper focuses on a detailed analysis of dynamics of mass transport from a liquid phase (river water) to a solid phase (river sediment). A series of relationships was developed describing concentration gradient for a periodic concentration changes of the substance. From theoretical analysis of transmittance for a solid phase it may be concluded that changes of concentration within solid phases of different thickness would become similar in the case when: solid phase thickness increases, concentration wave period decreases, rate constant of a substance decay within the solid phase increases.

At the phase boundary (solid phase side), the concentration gradient increases upon time shifts, with respect to the concentration function assuming that a substance decay takes place or none process occurs. A time shift varies within the range of $<0, 1/8>$ of a concentration function period.

The concentration gradient at the phase boundary (solid phase side) may be calculated based on the concentration changes and a derivative of a concentration with respect to time at the phase boundary. In the case of sine concentration changes, concentration gradients (Eq. (22a)) calculated using this method are accurate. Such a method of estimation of the concentration gradient may also be used when the concentration at the phase boundary changes in other than a sinusoidal mode.

Knowledge of concentration gradient enables one to develop an equation describing the mass flux penetrating into the solid phase. Such an equation may also be used to estimate the error in the mass penetration model if calculated using the Whitman film model. Neglecting the dispersion effects along the river bed in natural water bodies at a steady state results in serious errors. Then, application of advection models may be just accurate in many cases.

When cyclic concentration changes at the phase boundary may be described with a single harmonic function, the points of graph developed based on the concentration values and the concentration gradient at the same time instant form a closed curve – an ellipse. It may be noticed that the curve of the concentration gradient vs. delayed concentration gets more flat or it becomes a line segment. When time dependence of concentration can be described as couple of harmonics, the effect of curve flattening also occurs though it is not as ideal as in case of a single harmonic. The effect of curve flattening was used in construction of the model describing a relationship between the concentration gradient and concentration. The proposed model may also be used for description of the dependence of the concentration gradient on concentration when both absorption and desorption processes occur with a chemical reaction. In some specific cases, the model structure may be simplified just by ignoring an element referring to a delayed concentration. A simplified model is slightly less accurate than its complete version. In dynamic conditions, the concentration gradient at the phase boundary may be approximated using combination of linear concentration, delayed concentration and concentration derivative, all at the phase boundary with respect to time.

Numerical experiments showed that an increase of the constant rate of a chemical process enhanced the effect of curve flattening. Following the increase of the rate constant, the accuracy of model (27) improves while the coefficients a_2 and a_3 approach zero.

Increase of chemical process rate causes that changes of the concentration gradient at the phase boundary follow the changes of the concentration at the phase boundary.

The mass exchange problems presented in the paper focused on continuous changes of concentration at the phase boundary. The problems related to mass exchange when concentrations at the phase boundary are not continuous (e.g., absorption and adsorption processes occur) will be discussed elsewhere.

SYMBOLS

$(1/2)A_0$	– average concentration C_b , g/m ³
A	– surface area, m ²
A^*	– surface normal to diffusion direction, m ²
A_n, B_n	– coefficients of a trigonometric series, g/m ³
C, c	– concentration, g/m ³
C'	– concentration in the phase core, g/m ³
C_m'	– average concentration within a phase core, g/m ³

$\tilde{C}_{m,0}$	– average concentration in the phase core at an initial river cross-section, g/m ³
$\tilde{C}_{m,srd}$	– average value of the average concentration in the phase core for watercourse segment, g/m ³
\tilde{C}_a	– concentration amplitude in the phase core, g/m ³
\hat{C}	– Laplace transformation of a concentration function
C_i	– concentration at the phase boundary, g/m ³
$C_{i,m}$	– average concentration at the phase boundary, g/m ³
$C_{i,a}$	– concentration amplitude at the phase boundary, g/m ³
\hat{C}_i	– Laplace transformation of a concentration at the phase boundary, g/m ³
D	– diffusion coefficient, m ² /s
E_x	– longitudinal dispersion coefficient, m ² /s
E_z	– coefficient of vertical turbulent diffusion (perpendicular to the solid phase surface), m ² /s
G	– transmittance
h	– water level or the average water level in a river, m
i	– drop of a water level in a watercourse, unless stated otherwise
I	– imaginary unit, $I = (-1)^{1/2}$
k_r	– process rate constant, 1/s
k_w	– mass transfer coefficient at a liquid phase side, m/s
$k_{z,og}$	– overall equivalent rate constant for all processes occurring in both liquid and solid phases, s ⁻¹
L, L_0	– thickness of a solid phase layer, m
L_{odc}	– length of watercourse segment, m
M	– transmittance module $ G $
m	– weight, g
$r(C)$	– process rate in the liquid phase core, g/(m ³ ·s)
r_{og}	– total process rate, g/(m ³ ·s)
R_h	– hydraulic radius, m
$\text{re}(\dots)$	– real part of complex variables
$\text{im}(\dots)$	– imaginary part of complex variables
s	– complex variables
t	– time, s,
t_{01}, t_{02}	– time of appearing and disappearing of a concentration impulse in a initial river cross-section, s
t_{k1}, t_{k2}	– time of appearing and disappearing of concentration impulse in a final river cross-section, s
T	– period of a function, s
V	– velocity, m/s
V_{srd}	– average velocity, m/s
V^*	– liquid phase volume, m ³
x	– linear coordinate (longitudinal for a river), m
y	– linear coordinate, m

GREEK SYMBOLS

α_M, γ_M	– complementary parameters
$\Delta t_1, \Delta t_2$	– time shifts, s,
$\Delta t_0, \Delta t_k$	– time differences, s,
$\Delta\tau$	– impulse time, s
φ	– argument of transmittance G , rad
ω	– angular velocity, rad/s
ω_0	– angular velocity for the main harmonic, rad/s
Ω_1, Ω_2	– integration constant

SUBSCRIPTS AND SUPERSCRIPTS

- i – concentration at the phase boundary
- a – amplitude
- m – average value
- \sim – phase core, in the case of concentration
- \wedge – Laplace transformation

REFERENCES

- [1] BIELSKI A., *Selected aspects of mass transfer rate determination between phases in the watercourse. Part I. Analysis of the influence of periodical concentration changes on mass transport through phase boundary*, Cracow University of Technology, Techn. Bull., 2, 2006.
- [2] BIELSKI A., *Selected aspects of mass transfer rate determination between phases in the watercourse. Part II. Analysis of the influence of aperiodical concentration changes on mass transport through phase boundary*, Cracow University of Technology, Techn. Bull., 2, 2006.
- [3] DALI-YOUCEF N., OUDDANE B., DERRICHE Z., J. Hazardous Mater. A, 2006, 137, 1263.
- [4] JIMENEZ- CEDILLO M.J., OLGUIN M.T., FALL C., J. Hazardous Mater. 2009, 163, 939.
- [5] KEMBŁOWSKI Z., MICHAŁOWSKI S., STRUMIŁŁO C., ZARZYCKI R., *Theoretical basis of chemical and process engineering*, WNT, Warsaw, 1985 (in Polish).
- [6] KULA I., UĞURLU M., KARAOGLU H., CELIK A., Biores. Techn., 2008, 99, 492.
- [7] LUYBEN W.L., *Process modeling, simulation, and control for chemical engineers*, McGraw-Hill, New York, 1973.
- [8] *Management of Health and Environmental Hazards*, web adress: <http://www2.cyf.gov.pl>, files addresses: <http://www2.cyf.gov.pl/przewodnik>
- [9] ZHANG M.H., ZHAO Q.L., ZHENG X.B., YE F., Coll. Surf.A, Physicochem. Eng. Aspects, 2010, 362, 140.
- [10] POHORECKI R., WROŃSKI S., *Kinetics and thermodynamics of chemical process engineering*, WNT, Warsaw, 1977 (in Polish).
- [11] SZARAWARA J., SKRZYPEK J., *Basics of chemical reactor engineering*, WNT, Warsaw, 1980 (in Polish).

ZONGYIN DUAN*

MICROBIAL DEGRADATION OF PHENOL BY ACTIVATED SLUDGE IN A BATCH REACTOR

Biodegradation of phenol in a batch reactor was investigated using activated sludge. The sludge was able to degrade phenol of initial concentrations up to 1.500 mg/dm³. The optimum temperature and pH for the reaction were determined in extensive tests. The optimum pH was around 6, whereas the temperature showed no significant impact on the biodegradation rates over the investigated conditions. This activated sludge degraded phenol at the maximum rate of 0.048 g phenol/(g VSS-h) at pH 6 and 30 °C, whereas inhibitory effects existed at concentrations higher than 100 mg/dm³. The Haldane kinetic model was used to elucidate the kinetics of phenol degradation in an activated sludge. The kinetic parameters were estimated to be $q_{\max} = 0.4695$ g phenol/(g VSS-h), $K_1 = 28.4860$ mg/dm³, and $K_S = 603.9869$ mg/dm³, with the correlation coefficient (R^2) of 0.9599. The high q_{\max} value for phenol biodegradation shows that the activated sludge exhibited high resistance to phenol.

1. INTRODUCTION

Phenols and phenolic compounds originated from oil refineries, pulp and paper manufacturing plants, resins and coke manufacturing, steel and pharmaceutical industries are toxic to human beings, fish and to several biochemical functions [1–5]. Increasing presence of phenols represents a significant environmental toxicity hazard. Wastewaters including phenols and phenolic compounds must be treated in order not to be a threat with human health and not to lead to serious ecological risks [6–8]. Increasingly stringent restrictions have been imposed on the concentrations of these compounds in wastewaters for safe discharge. Thus, the approach for the removal of phenols from industrial wastewater has generated significant interest [9–14].

Several methods with different removal performance and cost levels are available for the treatment of phenolic wastewaters. Either conventional physicochemical [9, 10] or biological [15–19] techniques may be used. However, these treatments are very complex and expensive. This situation is triggering the development of new

*Department of Mechanical Engineering, Tongling University, Tongling, 244000 China, e-mail: dzy@tlu.edu.cn

treatment technologies for phenolic wastewater. Biological treatment has been shown to be economical, practical and the most promising and versatile approach as it leads to complete mineralization of phenol with low possibility of the production of byproducts [15, 16, 19]. In this viewpoint, the application of biodegradation process to metabolize the phenolic wastewater appears to be an alternative to conventional treatment processes.

However, the toxicity of phenolic compounds may inhibit or even reduce microorganisms in municipal biological wastewater treatment plant [20]. The presence of phenols strongly reduces biological biodegradation of other components which makes the process of degradation of phenols so difficult. It is the reason why activated sludge reactors have been widely used for phenol removal from industrial wastewater. Batch reactor processes employing either suspended or immobilized cultures are in use for the degradation of toxic compounds. The activated sludge process is generally a preferred biological process for the treatment of industrial wastewaters including phenols [15, 16, 19, 21–24].

Presently, great restrictions to application of biological processes are related to the acclimation of the biomass to phenol biodegradation and variability of wastewater composition. A simple and effective method to obtain a specified biomass from activated sludge for phenols treatment is highly desired, which provides selection and multiplication of specialized microorganisms. Furthermore, phenol degradation seems to be influenced by some environmental factors such as temperature and pH. This issue should also be explored for its full application, as well as the substrate inhibition effect and the related biodegradation kinetics. Thus, to acclimatize bacteria to phenol under experimental conditions easier to implement and to investigate the possibility of phenol biodegradation at high initial concentrations and to study the phenol biodegradation kinetics motivates this work.

Therefore, the aim of this work was to evaluate the microbial degradation of phenol by activated sludge in a batch reactor. The kinetics of phenol removal in a batch reactor was investigated in order to develop activated sludge process that could effectively treat phenols. The microbial process reported here could potentially be applied to remove phenols and phenolic compounds in industrial effluents.

2. MATERIALS AND METHODS

Experimental system. The experimental system was a fully mixed bench scale reactor with a constant temperature water circulator and monitoring device for temperature, dissolved oxygen (DO) and pH. The working volume of the reactor was 2 dm³. The reactor had a water jacket for controlling the temperature which was kept constant at each test. The air velocity of 0.3 m³·h⁻¹ was applied to the reactor. The DO concentration of the mixed liquor was controlled using the aeration ON/OFF controller. Air

was introduced by an air pump from the reactor bottom. The dissolved oxygen (DO) level was kept over 4 mg/dm³ in the aeration phase. The reactor was operated under batch operation and the stirring speed was adjusted to 100 rpm. The reactor was operated sequentially within a 6 h cycle, including 5 min of influent filling, 325 min of aeration, 20 min of settling, and 10 min of effluent discharging. Effluent was drawn from the middle port of the reactor column (1 dm³), and the resulting hydraulic retention time (HRT) was 12 h. Samples were taken from the reactor at predetermined time intervals using a peristaltic pump. The desired SRT was set by controlling the amount of sludge wasted from the reactor in each cycle. About 1.5 dm³ of seeding sludge were inoculated into the SBR, resulting in a mixed liquor suspended solid (MLSS) concentration of about 4.5 g/dm³ in the reactor, and correspondingly the loading rate was about 0.1 kg phenol/(m³·d).

Source of sludge and wastewater. The phenol removing sludge used in the experiments was developed from an activated sludge collected from a wastewater treatment plant in China. The seeding sludge had a sludge age of 10 d, a mixed liquor suspended solids (MLSS) concentration of 6.0 g/dm³ and the sludge volume index (SVI) of 70 cm³/g. The sludge was acclimatized for 40 days in aerobic and phenol containing wastewater before being used in experiments. The acclimatized culture was brown in colour and had fluffy, irregular and loose structure floc morphology, and filamentous bacteria could be well observed in the flocs. The synthetic contaminated wastewater was prepared from distilled water using phenol as the contaminant. The synthetic wastewater used in the batch growth studies comprised (dm⁻³): 227 mg (NH₄)₂SO₄, 100 mg MgSO₄·7H₂O, 0.5 mg FeCl₃, 100 mg MnSO₄·H₂O, 7.5 mg CaCl₂, 250 mg KH₂PO₄, and 500 mg K₂HPO₄.

Phenols biodegradation tests. The presence of phenols in wastewater varied widely from over ten to thousands in concentrations (mg/dm³). In addition, the toxicity of phenols that inhibit microorganisms might increase upon increasing concentration of phenols [1]. Thus, in this work, the concentrations of phenol for biodegradation tests were selected in a wide range based on reported literature values. The tests were started by inoculating synthetic wastewater containing 50–1500 mg/dm³ of phenol and the acclimatized sludge to the reactor at 30 °C. Thus, the initial phenol /biomass (F/M) ratios were 0.007–0.2 mg phenol /mg VSS (VSS is volatile suspended solid). The pH, biomass amount, and phenol concentrations of samples in reactors were measured at predetermined time intervals. The optimum temperature and pH for the biodegradation were determined in extensive tests. The pH values adjusted by phosphate buffer were in the range 5.0–8.0. The phosphate buffers were prepared by mixing various volume fractions of 0.375 g/dm³ of K₂HPO₄ and 0.42 g/dm³ of KH₂PO₄ solutions in deionized water (Millipore, Milli-Q). Control experiments, in a sludge-free medium which only included phenol and other constituents, were also done in order to evaluate the possi-

ble degree of phenol removal with volatilization and it was found that the phenol concentration almost remained unchanged. All the experiments were run in triplicate and the averaged results were reported here.

Analytical methods. Phenol concentration in suspension was measured using 4-aminoantipyrine colorimetric approach on supernatant drawn from samples centrifuged at 8000 rpm for 10 min. pH was determined by using a pH meter. Measurements of VSS were conducted in accordance with the standard methods [25]. Determination of biodegradation rates and parameters of the Haldane equation were done on a personal computer by using a spreadsheet program (Microsoft Excel 2003).

3. RESULTS AND DISCUSSION

3.1. PERFORMANCE OF BIODEGRADATION OF PHENOLS

The activated sludge was grown in the presence of phenol as the sole carbon source and adapted to increasing concentrations of phenol over a period of 40 days; the reactor was continuously operated during this period. The sludge is supposed to be acclimated to the system when phenol is completely degraded in repeated uses in fixed time intervals. The performance of the activated sludge to degrade phenol was evaluated by monitoring phenol disappearance at its various concentrations in the batch reactor. Figure 1 shows results of batch tests for phenol degradation by activated sludge at 30 °C. At initial phenol concentrations of 50–1500 mg/dm³, phenol concentration quickly decreased for all tests when phenol concentration was sufficient. For example, at an initial phenol concentration of 200 mg/dm³, the degradation reached 75% in 3 h. However, phenol concentrations in the batch reactor decreased with time rather steeply at low initial phenol contents as compared to those containing high levels of phenol. Since the phenol contents of the control reactors did not change significantly (<3%) during the course of experiments, the extent of non-biological degradation of phenol was negligible. These observations are in accordance with previous results [12, 26–28].

3.2. EFFECT OF INITIAL CONCENTRATION OF PHENOLS

Batch tests for phenol biodegradation using the activated sludge were conducted in the phenol containing synthetic wastewater with phenol concentrations of 50–1500 mg/dm³ at pH 6 and 30 °C. Based on Fig. 1, the average phenol biodegradation rates with various initial phenol concentrations (were determined to be 60, 60, 41, 40, 36, and 35 mg/(dm³·h), respectively. The sludge began degrading phenol without a time lag at an initial phenol concentration of 50 and 100 mg/dm³, and completely degraded phenols

in 0.8 and 1.8 h, respectively. At 200, 400, and 800 mg/dm³, the time lag of 2, 4, and 8 h was observed, after which phenol was completely degraded. At the initial concentration of 1500 mg/dm³, the lag time was 15 h and the time needed for complete phenol biodegradation was prolonged to 40 h. Furthermore, the average phenol biodegradation rates decreased upon increasing initial phenol concentrations from 50 mg/dm³ to 1500 mg/dm³, suggesting the inhibition to bacteria by high initial concentrations of phenols.

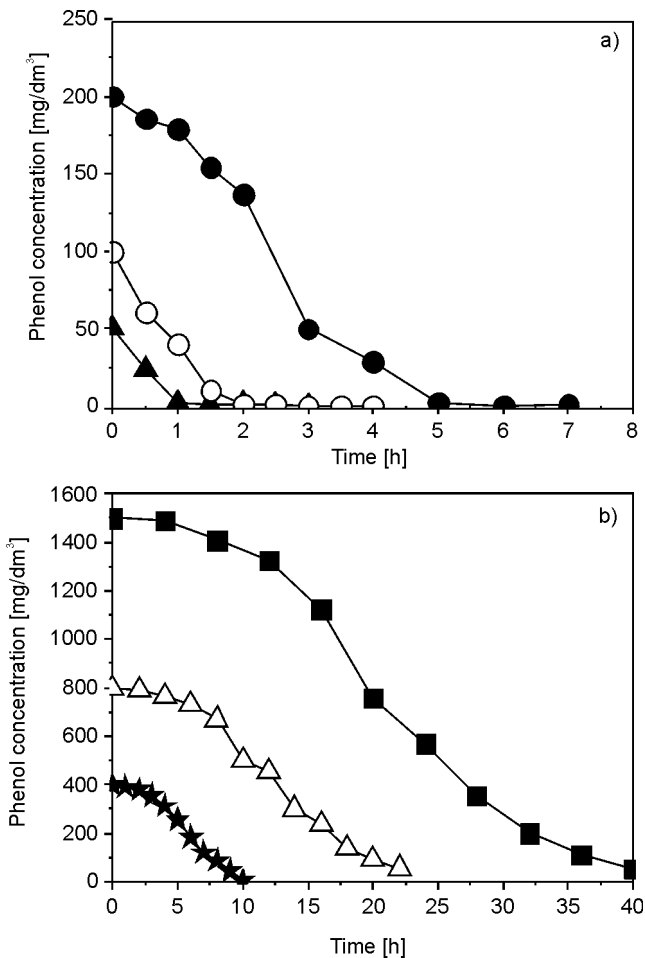


Fig. 1. Batch tests results of phenol biodegradation by activated sludge with various initial phenol concentrations at 30 °C and pH of 6:
a) 50, 100, 200 mg/dm³, b) 400, 800, 1500 mg/dm³

Figure 1 also shows that for the same initial biomass concentration the higher the concentration of phenol is the more time it takes to be consumed. The phenol concen-

tration in the culture medium decreases clearly due to utilization by microorganisms as they grow. The growth rate should be higher when phenol concentration decreased because of a substrate inhibition phenomenon. The extent of phenol degradation and the time required depends on the initial phenol concentration in the medium.

3.3. EFFECT OF TEMPERATURE AND PH TO BIODEGRADATION OF PHENOLS

Degradation of phenol seems to be dependent on some environmental factors such as temperature and pH [2, 29, 30]. Effect of temperature and pH was performed to explore their optimum values for biodegradation of phenols by the activated sludge in the batch reactor.

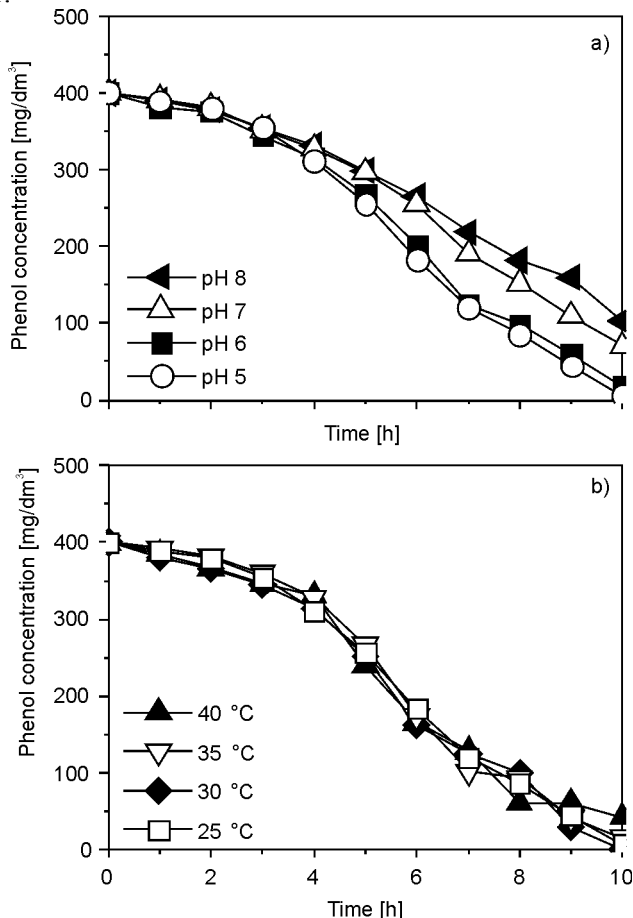


Fig. 2. Batch tests for phenol biodegradation by the activated sludge at the initial phenol concentration of 400 mg/dm³: a) effects of pH (5–8), b) effects of temperature (25–40 °C)

Figure 2 shows the results of batch tests at various pH and temperatures at the initial phenol concentration of 400 mg/dm³. Phenol was completely biodegraded at pH 5–6 and at 30 °C while not depleted at pH 7–8. In comparison, the biodegradation of phenols performance did not change much at 25–40 °C. The optimum pH for phenol degradation is around 6, whereas the temperature has shown no significant impact on the reaction rates over the investigated conditions.

Regarding the temperature effect, there are opposite experimental results in previous work [2, 19, 26, 31]. It has been reported that temperature could play an important role in the degradation of phenol [31]. Many authors find higher efficiency of phenol removal near 30 °C [2, 26, 28]. Chung et al. [28] found an optimum temperature of 30 °C for the two processes for immobilized cells and free cells. It is probably due to the higher production of metabolites at this temperature [29]. However, the rate and the extent of degradation is relatively sensitive to deviations outside the optimum range [26]. Adav et al. [19] found that temperature of 25–40 °C had no noticeable effect on the growth rate when using a strain with maximum ability to degrade phenol and a high tolerance to phenol toxicity isolated from an aerobic granule identified as *Candida tropicalis*. In short, it appears that biodegradation of phenol could occur at room temperature. Different sludge system might be a reason for different experimental results. Additionally, different wastewater characteristics, reactor operating conditions and microbial communities also are responsible for the differences.

The follow-up of the medium pH can be an indicator of the phenol degradation and one of the factors significant in the success of the biological treatment. A slight reduction is observed as biomass grows and pH variation increases when the initial phenol concentration increases [12, 32]. The decrease in pH suggests that biological degradation of phenol occurs and with a stable pH phenol is successfully degraded as shown in this work. pH significantly affects biochemical reactions required for phenol degradation. For instance, pure *P. putida* could not efficiently resist pH change [2]. Consequently, phenol degradation may be deteriorated as medium pH deviates. Aksu and Gonen [33] found that pH affects the surface charge of cells of the activated sludge biomass. Thus, the electrostatic attraction between phenol and activated sludge biomass would be impacted [33]. In conclusion, it seems that the best pH range for the phenol degradation does exist. It is possible that enzymes for phenol degradation have their optimum enzymatic activities at an optimum pH. However, the optimum pH for differs from one bacterium to another. For example, pH ranges between 8 and 11 were found for the bacterium *Halomonas campialis* and for the biodegradation of phenol by *Klebsiella oxytoca*, pH was 6.8 [34].

3.4. KINETICS OF BIODEGRADATION OF PHENOLS

Kinetic analysis of the biodegradation data was performed based on the Haldane equation for describing biodegradation of an inhibitory substrate [5]

$$q = \frac{q_{\max} S}{K_S + S + \frac{S^2}{K_I}}, \quad (1)$$

where q and q_{\max} are the specific and the maximum specific substrate degradation rates ($\text{g phenol}/(\text{g VSS}\cdot\text{h})$ in this work), respectively, and S , K_S and K_I are the substrate concentration, half-saturation constant, and inhibition constant (mg/dm^3), respectively.

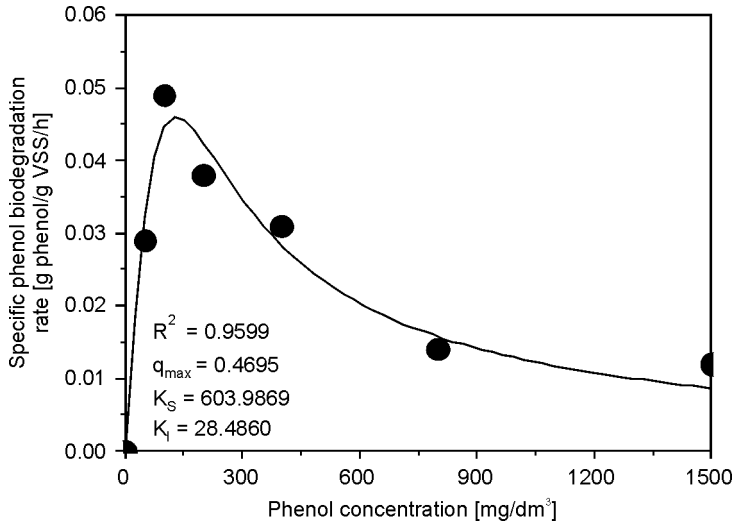


Fig. 3. Specific phenol biodegradation rates of the activated sludge at various phenol concentrations

Figure 3 shows the dependence of initial phenol biodegradation rate on its initial concentration. It increases upon the increasing initial phenol content up to $100 \text{ mg}/\text{dm}^3$, reaches maximum at $0.048 \text{ g phenol}/(\text{g VSS}\cdot\text{h})$ and then decreases for the initial phenol contents between 100 and $1500 \text{ mg}/\text{dm}^3$ for the inhibitory effect of phenol at concentrations above $100 \text{ mg}/\text{dm}^3$. The Haldane equation was used to model the phenol biodegradation data to evaluate the phenol biodegradation kinetics. The least-square error method was used to estimate the kinetic parameters to be $q_{\max} = 0.4695 \text{ g phenol}/(\text{g VSS}\cdot\text{h})$, $K_I = 28.4860 \text{ mg}/\text{dm}^3$, and $K_S = 603.9869 \text{ mg}/\text{dm}^3$, with the correlation coefficient (R^2) of 0.9599 .

These values are different from those obtained by Adva et al. [19]. In the study involving strains isolated from aerobic granules for phenol removal by Adva et al. [19], the kinetic parameters of q_{\max} , K_I and K_S were found to be $0.385 \text{ g phenol}/(\text{g VSS}\cdot\text{h})$, $185 \text{ mg}/\text{dm}^3$ and $7.1 \text{ mg}/\text{dm}^3$, respectively. The maximum specific phenol degradation rate was $0.47 \text{ g phenol}/(\text{g VSS}\cdot\text{h})$ in this work, higher than that in studies using strains

isolated from aerobic granules [4, 19]. The high q_{\max} value for phenol biodegradation shows that activated sludge exhibits high resistant ability to phenol.

3.5. IMPLICATIONS TO INDUSTRIAL TOXICITY REMOVAL

Ultimately this research aims to develop an effective activated sludge process to remove phenols and phenolic compounds in industrial effluents. This work demonstrates that the mixed culture (activated sludge from WWTP) can grow in a simple batch reactor using phenol as the limiting substrate, which is convenient, uncostly and easily operated. The experimental results show that it is possible to treat effluents containing high phenol concentration (up to 1500 mg/dm³) by activated sludge, indicating that the developed process can potentially be applied to removal of high extent of relate industrial toxicity. Furthermore, it is well known for the importance of the acclimatization for supporting the microorganisms which have the enzymatic material necessary to the degradation of phenol and revealing a new population which is adapted to this toxic agent and is able to consume it like substrate. This acclimatization may relatively easy realize the conditions of temperature and pH which is the most favourable for the development of these microorganisms and the increasing degradable phenol concentration. Thus, the results of this work might significantly benefit the real industry in terms of the extent of toxicity removal and cost of treatment. In addition, the model developed in this study has been applied successfully to phenol biodegradation data obtained from short-term batch experiments. The obtained kinetics for phenol biodegradation can be used for better understanding the activated sludge processes in full scale WWTPs. The high q_{\max} value for phenol biodegradation shows that activated sludge can exhibit high resistance to industrial toxicity with proper acclimatization as demonstrated in his work. To this end, a particular emphasis should also be given to develop a practical and easy implement methodology to facilitate its full scale application. The model and the obtained kinetics of phenol biodegradation can deliver a better insight into the system, which can be used to improve design, operation and control of the activated sludge processes for industrial toxicity removal. For example, the approaches and kinetic model presented in this paper could be employed for the design of a batch reactor system for the biodegradation of phenolic wastewater in petrochemical and oil refining industries.

4. CONCLUSIONS

This study demonstrates that activated sludge could be successfully applied in a batch reactor for phenol biodegradation. The sludge was able to degrade initial phenol concentrations up to 1500 mg/dm³. Results of batch tests show that the optimum pH was around 6, whereas the temperature showed no significant impact on phenol

biodegradation rates over the investigated conditions. Specific phenol biodegradation rates in the sludge followed the Haldane model because of substrate inhibition, and reached maximum at 0.048 g phenol/(g VSS·h) at the phenol concentration of 100 mg/dm³ at pH 6 and 30 °C. The least square error method was used to estimate the kinetic parameters of the reaction. The high q_{\max} value for phenol biodegradation shows that activated sludge exhibited high resistance to phenol. Therefore, this study demonstrated the technical feasibility of utilization of activated sludge for the effective biodegradation of phenols or phenolic compounds.

ACKNOWLEDGEMENTS

This work has been supported by the Department of Mechanical Engineering, Tongling University.

REFERENCES

- [1] ALEMZADEH I., VOSSOUGHI F., HOUSHMANDI M., Biochem. Eng. J., 2002, 11, 19.
- [2] ANNADURAI G., JUANG R., LEE D.J., Waste Management, 2002, 22, 703.
- [3] LIN S.H., WANG C.S., J. Hazardous Mater., 2002, 90, 205.
- [4] JIANG H.L., TAY J.H., MASZENAN A.M., TAY S.T.L., Appl. Environ. Microbiol., 2004, 70, 6767.
- [5] YI S., ZHUANG W.Q., WU B., TAY S.T.L., TAY J.H., Environ. Sci. Technol., 2006, 40, 2396.
- [6] BANDHYOPADHYAY K., DAS D., BHATTACHARYYA P., MAITI B.R., Biochem. Eng. J., 2001, 8, 179.
- [7] BOSZCZYK-MALESZAK H., CHORAZY M., BIESZKIEWICZ E., KACIESZCZENKO J., Acta Microbiol. Polon., 2002, 51, 183.
- [8] KAVITHA V., PALANIVELU K., Chemosphere, 2004, 55, 1235.
- [9] YANG R.D., HUMPHREY A.E., Biotechnol. Bioeng., 1975, 17, 1211.
- [10] LIN S.H., CHUANG T.S., Technol. Environ. Chem., 1994, 44, 243.
- [11] BASTOS A.E.R., MOON D.H., ROSSI A., TREVORS J.T., TSAI S.M., Arch. Microbiol., 2000, 174, 346.
- [12] MONTEIRO A.M.G., BOAVENTURA A.R., RODRIGUES A.E., Biochem. Eng. J., 2000, 6, 45.
- [13] ALEKSIEVA Z., IVANOVA D., GODJEVARGOVA T., ATANASOV B., Process Biochem., 2002, 37, 1215.
- [14] JIANG Y., WEN J.P., LI H.M., YANG S.L., HU Z.D., Biochem. Eng. J., 2005, 24, 243.
- [15] ROZICH A.F., GAUDY JR. A.F., ADAMO P.D.D., Water Res., 1985, 19, 481.
- [16] ACUNA-ARQUELLES M.E., OLGUIN-LORA P., RAZO-FLORES E., Biotechnol. Lett., 2003, 25, 559.
- [17] RAMOS M.S., DIVILA J.L., THALASSO E.F., ALBA J., GUERRERO A.L., AVELAR F.J., Water Sci. Technol., 2005, 51, 257.
- [18] HERNANDEZ-ESPARZA M., DORIA-SERRANO M.C., ACERO-SALINAS G., RUIZ-TREVINO F.A., Biotechnol. Process, 2006, 22, 1552.
- [19] ADAV S.S., CHEN M.Y., LEE D.J., REN N.Q., Biotechnol. Bioeng., 2007, 96, 844.
- [20] WANG S.J., LOH K.C., Enzyme Microb. Technol., 1999, 25, 177.
- [21] YAMAGISHI T., LEITE J., UEDA S., YAMAGUCHI F., SUWA Y., Water Res., 2001, 35, 3089.
- [22] VAZQUEZ I., RODRIGUEZ J., MARANON E., CASTRILLON L., FERNANDEZ Y., J. Hazard. Mater., 2006, 137, 1681.
- [23] VAZQUEZ I., RODRIGUEZ J., MARANON E., CASTRILLON L., FERNANDEZ Y., J. Hazard. Mater., 2006, 137, 1773.
- [24] KONYA I., EKER S., KARGI F., J. Hazard. Mater., 2007, 143, 233.

- [25] APHA. *Standard Methods for the Examination of Water and Wastewater*, 20th Ed., Washington, D.C., American Public Health Association, 1998.
- [26] MORDOCCHI A., KUEK C., JENKINS R., Enzyme Microb. Technol., 1999, 25, 530.
- [27] GONZALEZ G., HERRERA M.G., GARCIA M.T., PENA M.M., Bioresour. Technol., 2001, 76, 245.
- [28] CHUNG T.P., TSENG H.Y., JUANG R.S., Process Biochem., 2003, 38, 1497.
- [29] SA C.S.A., BOAVENTURA R.A.R., Biochem. Eng. J., 2001, 9, 211.
- [30] PAZARLIOGLU N.K., TELEFONCU A., Process Biochem., 2005, 40, 1807.
- [31] NUHOGLU A., YALCIN B., Process Biochem., 2005, 40, 1233.
- [32] PAI S.L., HSU Y.-L., CHONG N.-M., SHEU C.-S., CHEN C.H., Bioresour. Technol., 1995, 51, 37.
- [33] AKSU Z., GONEN F., Process Biochem., 2004, 39, 599.
- [34] MARROT B., BARRIOS-MARTINEZ A., MOULIN P., ROCHE N., Biochem. Eng. J., 2006, 30, 174.

S.M. SHIRAZI*, S. WIWAT**, H. KAZAMA**, J. KUWANO**, M.G. SHAABAN*

SALINITY EFFECT ON SWELLING CHARACTERISTICS OF COMPACTED BENTONITE

Swelling characteristics of compacted bentonite is the most important factor for nuclear waste disposal facilities. Salinity effect on swelling behaviour of compacted bentonite was investigated experimentally. A series of one dimensional swelling deformation tests have been performed. The tests were conducted for various initial dry densities from 1.33 g/cm^3 to 1.90 g/cm^3 for compacted bentonite saturated with NaCl of various concentrations in solution from 0 to 4.0 M. It was found that initial dry density and concentration of NaCl strongly influence the swelling rate of bentonite. The swelling rate of bentonite decreases with increasing the concentration of NaCl. Swelling rate depends on the concentration of NaCl more than on initial dry density and loading effect. Bentonite may change from highly swelled material to coagulate in saline water. Liquid limit of bentonite is also remarkably decreased with the change of liquid from distilled water to saline one, while the plastic limit is slightly increased.

1. INTRODUCTION

Bentonite has attracted attention as buffer and backfill materials for high level radioactive waste (HLW) disposal. High level radioactive and hazardous wastes are required to be buried in deep underground facilities. The buffer material is filled in a partially saturated form as compacted block. After waste emplacement, buffer material hydrate and swell, being submitted to heat from radioactive waste decay. Combined effects of heat generated by radioactive decay and solutes supplied from the surrounding rock will take place several hydromechanical processes in the field. These processes may change mechanical, hydraulic, and geochemical properties of buffer materials. Bentonite is often a key component of the engineered barrier system because it has good sorption properties, microporous structure, low hydraulic conductivity, and high cation exchange capacity [1].

*Department of Civil Engineering, Faculty of Engineering, University of Malaya, 50603 Kuala Lumpur, Malaysia. Corresponding author S. M. Shirazi, e-mail: smshirazi@gmail.com

**Saitama University, 255 Shimo-okubo, Sakura-ku, Saitama-shi, 338-8570 Japan.

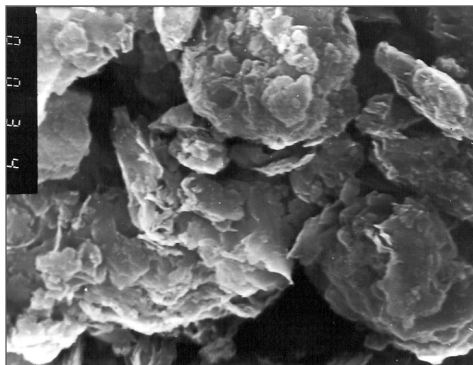


Fig. 1. Microstructure of compacted Kunigel VI bentonite

Microstructural view of compacted bentonite is presented in Fig. 1. It restricts the movement of nuclides from the waste packages after canister failure. Mechanical properties of compacted bentonite under combined effect of water from surrounding rock and heat from canister have been reported by many researchers [2–6]. The experimental information on the properties of compacted bentonite was mainly saturated with distilled water as a test fluid. However, some HLW disposal sites are constructed at the coastal area, e.g. HLW site at Horonobe in Hokkaido prefecture of Japan. At the coastal area, groundwater is blended with sea water and affects the mechanical properties of compacted bentonite. For this problem, a series of laboratory tests were performed to investigate the effect of salinity on swelling behaviour of compacted bentonite.

2. MATERIALS AND METHODS

Kunigel VI bentonite is used in this experiment which is considered to be applied as buffer material for HLW disposal in Japan. Specific gravity and montmorillonite content in Kunigel was 2.79 and 64%, respectively. Kunigel VI was compacted by a special compaction device. The specimen height and required density were maintained by the variation of mass and compaction pressure. Initial dry densities of the samples were 1.30, 1.50, 1.70 and 1.90 g/cm³. The height of the sample was ca. 1 cm with the diameter of 6 cm. NaCl solutions were prepared by dissolving powdered NaCl in distilled water to a desired concentration. The concentrations of the solutions were 0.5, 1.0, 2.0 and 4.0 M.

Swelling deformation tests. Free swelling deformation tests of compacted bentonite were carried out with a special swelling box apparatus by absorbing saline solution under approximately zero vertical pressure except the cap plate. Swelling deformation tests were also conducted with an oedometer test apparatus under loading condition. The vertical swelling deformation of compacted specimens was measured under static

load of 0.16 MPa. Saline solution was supplied at the bottom and simultaneously prescribed vertical pressure was applied to the specimen. Both tests were carried out at room temperature. Degree of saturation was about 100% for all specimens at the end of experiment. Swelling rate of the compacted specimens was calculated by the following equation.

$$S_R = \frac{\Delta h}{h_0} \times 100, \quad (1)$$

where S_R is the swelling rate, Δh is the vertical deformation and h_0 is the initial height.

Maximum swelling rate ratio was calculated by the following equation:

$$\text{Maximum swelling rate ratio} = \frac{\text{Maximum swelling rate with NaCl}}{\text{Maximum swelling rate with distilled water}}. \quad (2)$$

3. RESULTS AND DISCUSSION

3.1. LIQUID LIMIT AND PLASTIC LIMIT

The liquid limit and plastic limits of bentonite with various concentrations of NaCl solution are presented in Fig. 2.

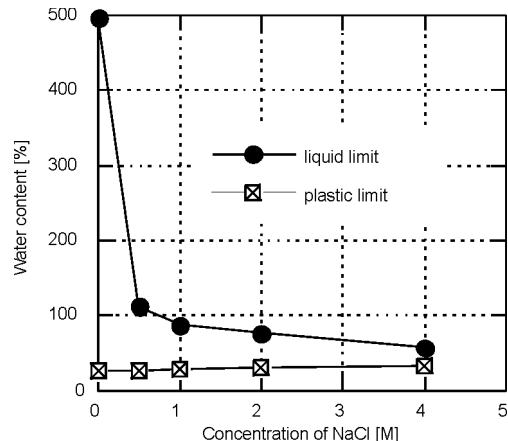


Fig. 2. Dependence of water content on concentration of NaCl for liquid and plastic limits

The liquid limit of bentonite strongly decreases after changing solution from distilled water to 0.5 M NaCl and then gradually decreases with the increasing of concentration of NaCl. The plastic limit slightly increases when the concentration of the NaCl solution is increased. This shows that salinity strongly affects the adsorption capacity of bentonite and bentonite becomes more sensitive when the concentration of NaCl

increases. One may expect that squeezing out of the liquid by applied forces during rolling has more effect than interparticle repulsion within the particle. Mishra et al. [7] reported the effect of salinity of low concentration ($0 \sim 1 \text{ mol}/\text{dm}^3$) on liquid limit of various types of bentonite. They found that the liquid limit of all type of soil decreased with increasing salt concentration. This trend can be explained in terms of the interparticle forces that play a prominent role in determining the liquid limit. In clay paste with water content equivalent to the liquid limit, the forces of interaction between clay particles become sufficiently weak to allow easy movement of particles relative to each other. In high swelling clays like montmorillonite, the dominant interparticle force is repulsion, which determines the distance between particles. Upon the increasing salt concentration, interparticle repulsion in montmorillonite decreases and the particle becomes free to move at lower interparticle distance [8–10].

3.2. FREE SWELLING

A schematic diagram of free swelling deformation of compacted bentonite is presented in Fig. 3. Swelling materials like montmorillonite gradually receive water and can be swelled against the overburden pressure (p_c).

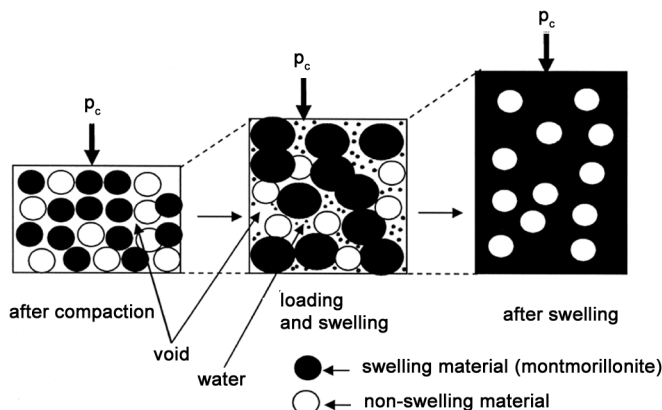


Fig. 3. Model of swelling deformation at high density

Detailed swelling mechanism was also explained by Shirazi and Kazama [4] in a previous study. Time dependences of free swelling rate of compacted bentonite of the initial dry density of $1.90 \text{ g}/\text{cm}^3$ at various NaCl concentrations is shown in Fig. 4. Free swelling rate of compacted bentonite markedly decreases with increasing concentration of NaCl. Figure 5 shows that the maximum swelling rate noticeably decreased upon increasing concentration of NaCl (from 0 to 1 M) for various dry densities. However, with a further increase in the concentration from 1.0 to 4 M, the swelling

rate gradually decreases. Time dependences of free swelling rates of bentonite in 1 M NaCl with various initial dry densities are presented in Fig. 6.

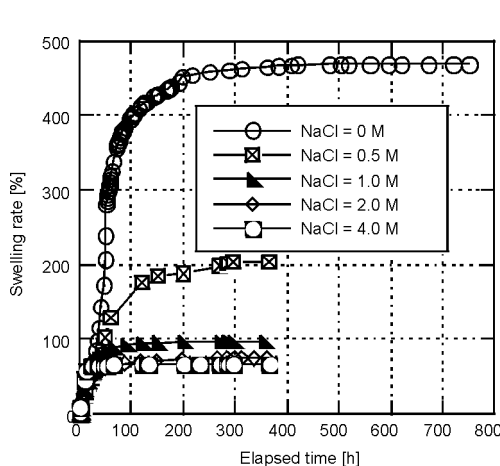


Fig. 4. Time dependences of free swelling rate for initial dry density of 1.9 g/cm^3 and various NaCl concentrations

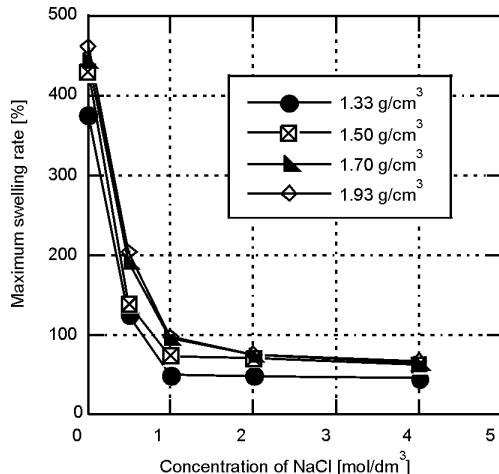


Fig. 5. Dependences of maximum swelling rate of bentonite on NaCl concentration for various dry densities

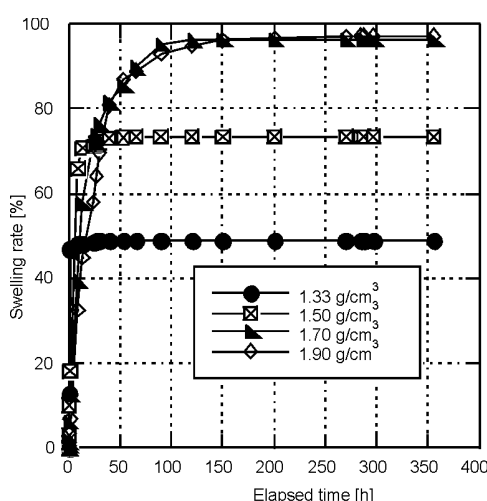


Fig. 6. Time dependences of free swelling rate of bentonite of various dry densities in 1 M solution of NaCl

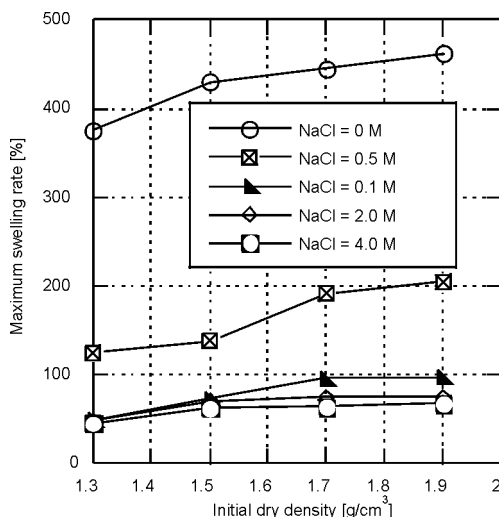


Fig. 7. Dependences of maximum swelling rate of bentonite on initial dry density for various NaCl concentrations

The swelling rate markedly increases upon increasing initial dry density of bentonite. Figure 7 shows that the maximum swelling rate of bentonite increases upon

increasing initial dry density for various concentrations of NaCl. It might be due to the montmorillonite content in the specimen. Thickness of the diffuse double layer is dependent on the concentration of electrolyte and the valence of the exchanged cations. Van Olphen [11] also indicated that *increasing NaCl concentration is interpreted as being due to a decrease in double-layer swelling between quasicrystals. As the electrical double layer adjacent to the quasicrystal surface is compressed with increasing NaCl concentration, the aggregate swell may decrease.*

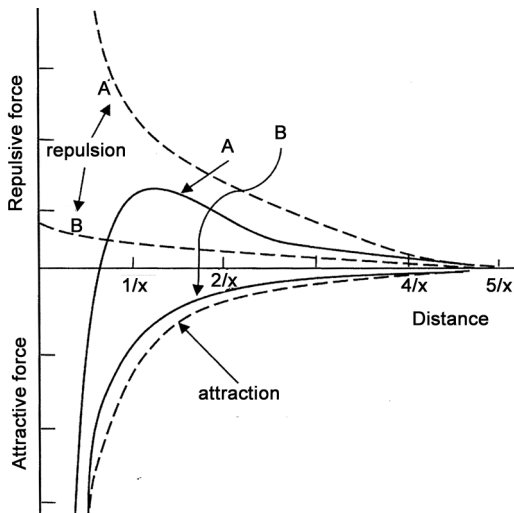


Fig. 8. Interaction forces in DLVO theory [12];
 $1/x$ – thickness of the diffuse double layer,
A – low concentration, B – high concentration

Figure 8 shows the interactions forces according to the Derjaguin Landau, Verwey and Overbeek (DLVO) theory [12]. DLVO theory suggests that the stability of a particle in solution depends upon balance of attractive and repulsive interactions. The figure shows the difference between the resultant forces in low and high concentration of electrolytes in solution. The attractive forces at the surfaces of clay particles stay constant but repulsive forces are dependent on the concentration of electrolytes. Lower concentration induced greater repulsive forces and finally held sufficiently repulsive force. Whereas, the higher concentration induced lower repulsive force and finally resulted in attractive force at the particle surfaces. Therefore, due to low concentration of salt, the particles have sufficiently high repulsion, the dispersion will resist flocculation and the colloidal system will be stable. However, repulsion mechanism does not exist in solutions of high concentrations of electrolyte and then flocculation or coagulation eventually takes place. The results of the present study are in agreement with the findings of the DLVO theory.

3.3. SWELLING UNDER LOADING CONDITIONS

The swelling rates of compacted bentonite under static load of 0.16 MPa for various initial dry densities and NaCl concentrations (0–4 M) are shown in Figs. 9–12.

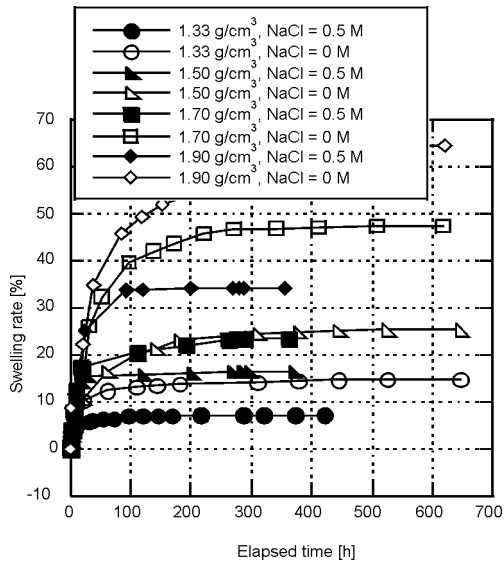


Fig. 9. Time dependences of the swelling rate of bentonite in distilled water and 0.5 M NaCl

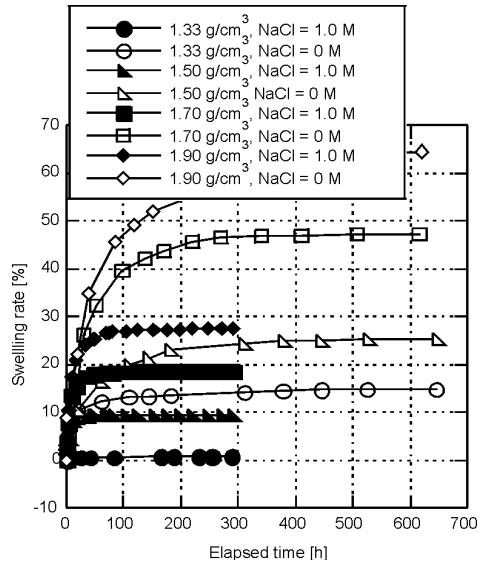


Fig. 10. Time dependences of the swelling rate of bentonite in distilled water and 1 M NaCl

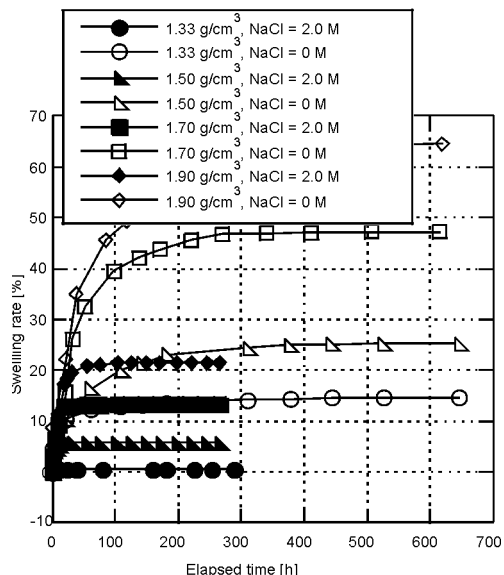


Fig. 11. Time dependences of the swelling rate of bentonite in distilled water and 2.0 M NaCl

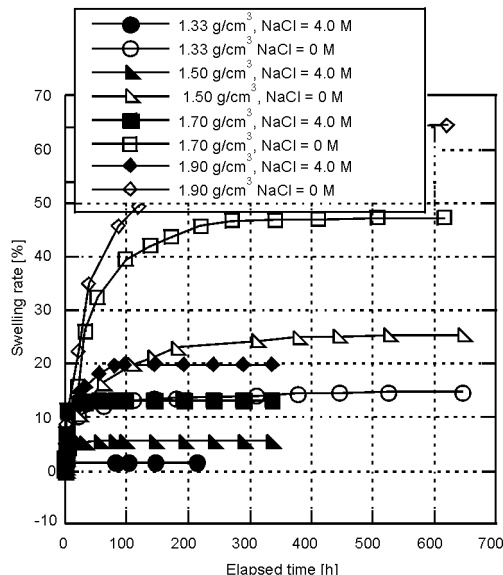


Fig. 12. Time dependences of the swelling rate of bentonite in distilled water and 4.0 M NaCl

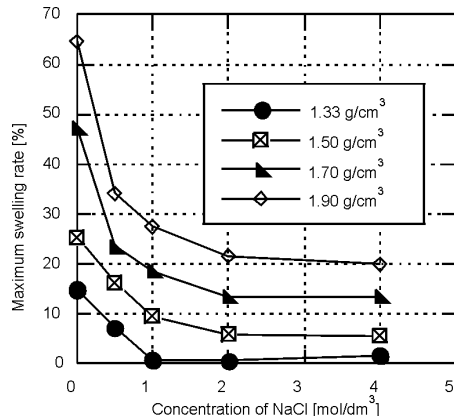


Fig. 13. Dependences of maximum swelling rate on NaCl concentration for various dry densities

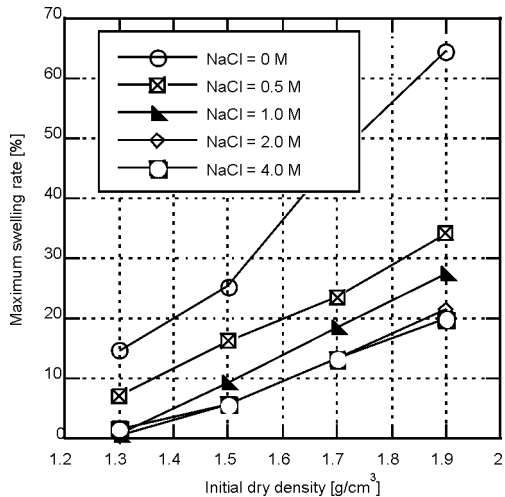


Fig. 14. Dependences of maximum swelling rate on initial dry density for various NaCl concentrations

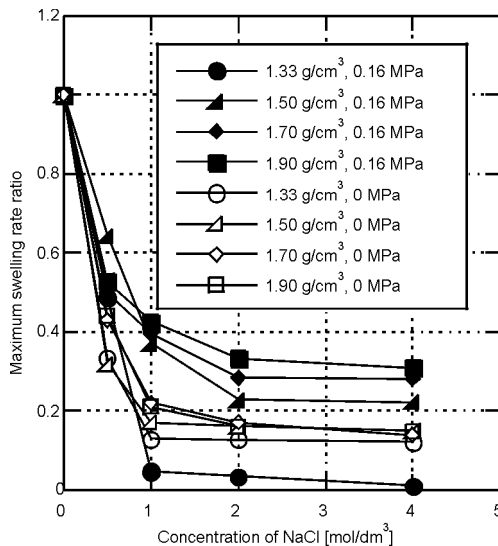


Fig. 15. Dependences of maximum swelling rate ratio on NaCl concentration for various dry densities and static loads 0 or 0.16 MPa

It is clearly seen that salinity has enormous effect on the swelling rate of compacted bentonite. Suzuki et al. [13] indicated that it might be due to a decrease in double layer swelling between quasicrystals by NaCl. As the electronic double layer adjacent to the quasicrystal surface is compressed with increasing NaCl concentration, the aggregate swelling may decrease. Thus, aggregate swelling for NaCl solution is possibly controlled by both crystalline swelling and double layer swelling between quasicrystals. The maximum swelling rate of the same initial dry density specimen at vari-

ous NaCl concentrations decreased noticeably compared to distilled water. For the initial dry density of 1.33 g/cm^3 , the specimen showed negative swelling rate at the beginning due to the applied static loads and become positive nearly zero after a few hours. However the maximum swelling rate of these specimens was markedly low. The maximum swelling rates of high initial dry density specimens is higher compared to lower initial dry density.

Figure 13 shows the dependence of the maximum swelling rate on the NaCl concentration at various densities of bentonite under static load of 0.16 MPa. The maximum swelling rate of bentonite sharply decreases for an increase in the NaCl concentration of 0 to 1.0 M. However, with a further increase in the concentration from 1.0 to 4 M, the maximum swelling rate gradually decreases. The specimen of lower initial dry density (1.33 g/cm^3) hardly shows the swelling behaviour as the final maximum swelling rate was lower than 1% at higher concentration of NaCl. Swelling rate markedly increases with the increasing initial dry density of bentonite and decreasing NaCl concentration as shown in Fig.14. It is due to the content of montmorillonite in specimens of higher initial dry density compared to those of lower initial dry densities.

The maximum swelling rates are normalized with respect to the swelling rates in distilled water and re-plotted against concentration of NaCl as shown in Fig. 15. The swelling rate ratio of bentonite markedly decreased for an increase in the concentration of NaCl from 0 to 1.0 M. The maximum swelling rate ratio decreases from 1.0 to almost 0.2. It is clearly observed that when the test fluid is blended with NaCl, the maximum swelling rate noticeably decreases. However, with a further increase in the concentration from 1.0 to 4 M, the swelling rate ratio was gradually decreased. The trend line of these curves is similar to the result of liquid limit test.

4. CONCLUSIONS

Liquid limit of bentonite remarkably decreased from 497% to 112% when the test liquid changed from distilled water to 0.5 M of NaCl solution. Then it gradually decreases upon the NaCl concentration increasing from 0.5 to 4 M while plastic limit slightly increased upon the increasing salt concentration. The controlling parameters of the swelling deformation of compacted bentonite are not only initial dry density and content of bentonite but also the salinity. The maximum swelling rate is less than 1% for lower dry density specimens with high concentration of NaCl. Maximum swelling rate of the specimens in various NaCl solutions is about 50–80% lower than in distilled water. Therefore, if the groundwater surrounding the bentonite barrier is blended with salt, the bentonite might change its characteristics from highly swelled material to coagulate in saline water. Special attention should be paid on using bentonite in nuclear waste disposal, when salt of high concentration is present in groundwater.

ACKNOWLEDGEMENT

Financial support for JSPS Postdoctoral Fellowship and Grant-in-Aid Scientific Research No. 19-07393 of first author by Japan Society for the Promotion of Science (JSPS) is gratefully acknowledged. Helpful comments of referees are greatly appreciated, which significantly improved the quality of original manuscript.

REFERENCES

- [1] JAEA. *Research and development on radioactive waste disposal*, 2–4, Shirakata-Shirane, Tokaimura, Ibaraki, Japan, 2008, 319–1195.
- [2] KOMINE H., OGATA N., Can. Geotech. J., 1994, 31 (4), 478.
- [3] SHIRAZI S.M., KAZAMA H., Austr. Geomech., 2004, 39 (4), 63.
- [4] SHIRAZI S.M., KAZAMA H., Austr. Geomech., 2004, 39 (4), 71.
- [5] SHIRAZI S.M., KAZAMA H., OSHINBE M., Austr. Geomech., 2005, 40 (4), 27.
- [6] SHIRAZI S.M., KAZAMA H., CHIM-OYE W., KUWANO, Austr. Geomech., 2008, 43 (2), 9.
- [7] MISHRA A.K., OHTSUBO M., LI L.Y., Environ. Geol., 2008, 57, 1145–1153.
- [8] SHIRAZI S.M., KUWANO J., KAZAMA H., WIWAT S., ISMAIL Z., Disaster Adv., 2011, 4 (1), 41.
- [9] SRIDHARAN A. AND RAO G.V. *Mechanism controlling liquid limit of clays*, [In:] Proc. the Istanbul Conf. Soil Mechanics and Foundation Engineering, 1975, 75.
- [10] WARKENTIN B.P., Nature, 1961, 190, 287.
- [11] VAN OLPHEN H., *An introduction to clay colloid chemistry*, 2nd Ed., Wiley, New York, 1997.
- [12] SZILVÁSSY Z., *Soils engineering for design of ponds, canals and dams in aquaculture*, Ch. 5, Food and Agricultural Organization, Research Centre for Water Resources Development, Budapest, Hungary, 1984.
- [13] SUZUKI S., SOMCHAI P., ICHIKAWA Y., CHAE B.G., Appl. Clay Sci., 2005, 29, 89–98.

MAŁGORZATA KABSCH-KORBUTOWICZ*, MAŁGORZATA KUTYŁOWSKA*

USE OF ARTIFICIAL INTELLIGENCE IN PREDICTING THE TURBIDITY RETENTION COEFFICIENT DURING ULTRAFILTRATION OF WATER

The artificial neural network (ANN) is widely used as new mathematical tool offering an alternative way of dealing with complex problems. To predict water quality after coagulation/ultrafiltration processes using an immersed membrane, various structures of multilayer perceptrone with one hidden layer were created. Feed water turbidity, turbidity in a tank, pH and temperature in the tank as well as transmembrane pressure and permeate flux were treated as input signals. Based on the best network chosen, prognosis of water quality was done. The created ANN was able to predict very accurately behaviour of a real system with relative errors of turbidity retention coefficient equal to 2.16×10^{-2} .

1. INTRODUCTION

According to strict regulations of water quality, in order to achieve the assumed level of purification, among water treatment technologies integrated membrane processes are applied. Hybrid processes being a combination of several physicochemical processes are believed to achieve a very high efficiency of water treatment. The processes of coagulation/ultrafiltration or ion exchange-sedimentation/ultrafiltration are state of art and nowadays are widely applied for drinking water treatment [1, 2]. Despite substantial progress made in recent years in membrane sciences, many initial problems associated with these processes such as limitations in the ability to control and predict water quality after the treatment process remain unresolved. Unfortunately, there is a lack of a traditional mathematical model solving the problem of permeate quality and no data are available on prediction permeate quality using artificial networks. Thus a suitable method of optimization should be developed to model the

*Institute of Environmental Protection Engineering, Wrocław University of Technology, Wybrzeże Wyspiańskiego 27, 50-370 Wrocław, Poland. Corresponding author M. Kabsch-Korbutowicz, e-mail: malgorzata.kabsch-korbutowicz@pwr.wroc.pl

most important membrane parameters. The method of modelling based on an artificial neural network (ANN) is lately very popular in chemical and environmental engineering. Predicting the permeate quality using ANN will be a useful approach.

1.1. BASIC INFORMATION ABOUT ARTIFICIAL NEURAL NETWORKS

Human nervous system performance is the base of information transferring in artificial neural networks. The neurons in the network are data processors and are responsible for summarizing input signals. ANN just computes output values from input values. The sum of transferred information is weighted. These weighted connections are modified during the learning process. Nowadays, the most popular type of network is multilayer perceptron, characterized by one input layer, one or more hidden layers and one output layer. It should be remembered that ANN modelling is like a “black box” approach and that is why it is impossible to penetrate deeply inside the way of forming the network structure, especially in the hidden layer. It is needed to create the artificial network for each problem separately. The solved problem extorts the number of neurons, the kind of activation function and the training methods. ANN has the ability to generalize and to approximate optimized matter. This issue is very important, due especially to the forecasting of membrane parameters because the changes during the separation are difficult to locate and to describe.

1.2. APPLICATION OF ANN IN MODELLING MEMBRANE PARAMETERS

Water quality variables which are complex and nonlinear need the application of alternative techniques of modelling [3]. In recent years, artificial neural networks were often used to model and forecast parameters of low-pressure membrane processes. The full literature review has been already summarized in the paper [4]. A lot of elaborations concern the modelling parameters of membrane processes in food industry (e.g., milk ultrafiltration and microfiltration or purification of juices) [5–7]. It is possible to use artificial intelligence to predict hydraulic parameters during membrane water and wastewater treatment [8]. Until now mainly the values of the quantity parameters were modelled [9, 10] (e.g., permeate flux or fouling rate). ANN were used also for predicting the quality parameters (retention coefficient of humic substances) [11] but such investigations are rather rare.

2. EXPERIMENTAL. COAGULATION/ULTRAFILTRATION OF WATER

In the experiments (done at University of Technology in Dresden, Institute of Urban Water Management, Chair of Water Supply Engineering by Professor Uhl's scientific group) the coagulation/ultrafiltration process was used to treat reservoir water

[12, 13]. The system was equipped with 3 submerged capillary modules ZeeWeed 500c produced by the Zenon company. The total surface of the membranes amounted to 60 m^2 . Nominal pore size of the membrane was $0.04\text{ }\mu\text{m}$ and cut-off 200 kDa.

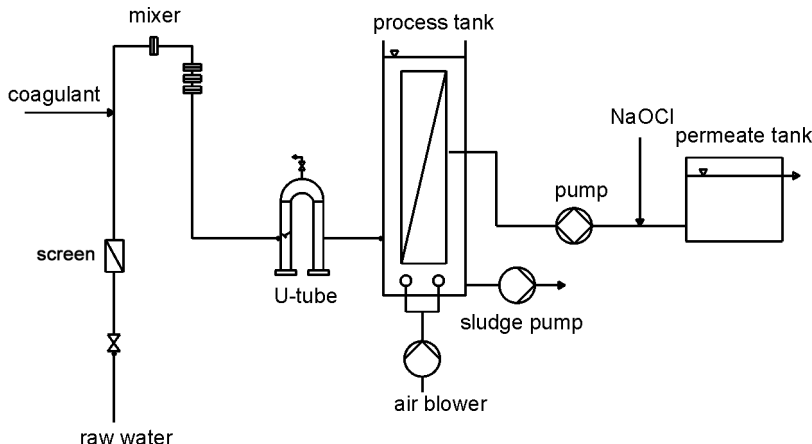


Fig. 1. Pilot plant set-up [13]

Figure 1 shows the set up of the pilot installation. Prior to coagulant ($\text{Al}_2(\text{SO}_4)_3$) dosage raw water was filtered by a screen filter in order to remove mechanical impurities. The coagulant ($0.5\text{ g Al}^{3+}\cdot\text{m}^{-3}$) was added before the tank and mixed precisely by cross-sectional changes to obtain a homogeneous solution. The first step of coagulation proceeded in a U-tube which had the diameter sixfold larger than the diameter of the pipe. This device provided the retention time of 9 min for aggregation of micro- and macroflocule complexes. Water with flocks fed the tank with immersed membranes. During the filtration, water from the tank was sucked to the fibre using partial vacuum in the range 15–55 kPa. Filtration time was equal to 10 min. When the trans-membrane pressure (partial vacuum) reached the level of approximately 55 kPa (after ca. 6–12 weeks of work), the chemical cleaning of the membrane with hydrochloric acid and/or citric acid was performed. While cleaning other equipment was disinfected with sodium hypochlorite. The total solids from the container were carried away by special sludge pump and stored. The results of experiments carried out in the pilot plant were used for creating, learning and verification of an artificial neural network.

3. ASSUMPTIONS OF ANN STRUCTURES FOR MODELLING OF THE TURBIDITY RETENTION COEFFICIENT

The approach of the artificial neural network was performed using the program Statistica 8.0. The aim of the work was to forecast, using ANN, the turbidity retention

coefficient after integrated process coagulation/ultrafiltration of reservoir water on the submerged membrane Zenon ZeeWeed 500c. Continuously (every 5 min) such parameters as transmembrane pressure (ΔP , kPa), temperature (T_t , K) and pH (pH_t) in the tank, real permeate flux in normal conditions 293.15 K (J , $m^3 \cdot m^{-2} \cdot d^{-1}$) and inlet turbidity of raw water (M_i , NTU) were measured. Turbidity in the tank (M_t , NTU) and permeate turbidity (M_p , NTU) were measured only pointwise (ten times during the whole experimental cycle). The coagulant dose (D) was constant and amounted to $0.5 \text{ g Al}^{3+} \cdot m^{-3}$. Variable D , being constant, was not included in the input signals. During the training of the network input parameters were changing in the range: 10.13–14.76 NTU for M_i ; 22.60–46.10 NTU for M_t ; 32.12–33.61 kPa for ΔP ; 278.00–278.01 K for T_t ; 7.01–7.02 for pH_t ; $1.62\text{--}1.67 \text{ } m^3 \cdot m^{-2} \cdot d^{-1}$ for J . Experimental output signal (R_e – turbidity retention coefficient) varied between 0.9970 and 0.9977. During the prognosis, input parameters were changing in the range: 10.13–14.76 NTU for M_i ; 22.60–46.10 NTU for M_t ; 32.27–33.70 kPa for ΔP ; 278.00–278.01 K for T_t ; 7.02–7.05 for pH_t ; $1.62\text{--}1.67 \text{ } m^3 \cdot m^{-2} \cdot d^{-1}$ for J . Experimental output signal (R_e) varied between 0.9970 and 0.9977. To obtain reliable results of forecasting, it was required to dispose the parameters with similar scopes of changes. It is worth pointing out that the practical significance of knowing the turbidity retention coefficient is really important because water turbidity allows us to classify the water quality and the quantity of natural organic matter which seems to be very crucial when technological processes of water treatment are planned.

Twenty neural network models have been created. Five models characterized by the smallest mean square error during the modelling were chosen as optimum. These models were used to make the prognosis. Then the best model (with the lowest error during the forecasting process) was chosen as most advantageous and useful in the future.

During the analysis of the network structure, there were investigated:

A. Choice of subsets. A random sampling method was used. From all 18 data used for network learning, 50% were chosen for training, 25% for testing and 25% for validation. In prognosis, the best created network used 100% of 12 values for testing.

B. Type of network. Only multilayer perceptrone (MLP I-H-O) with I number of input neurones, H number of hidden neurones and O number of output neurones was examined. It is the most popular network architecture used nowadays.

C. Minimum number of hidden neurons. To have reliable boundary conditions, the lowest number of the hidden neurons was established at the level of 2.

D. Maximum number of hidden neurons. To have reliable boundary conditions, the highest number of hidden neurons was established at the level of 30. More neurons lead to overfitting the network [14].

E. Activation functions in the hidden and output layer. Typical and simple activation functions were chosen: linear, logistic, hyperbolic tangent, exponential.

F. Methods of learning. For training the following algorithms were investigated: BFGS (quasi-Newton approach), fastest decline, conjugated gradient descent.

G. Number of learning epochs. It was reasonable to choose the range of training epochs in the range 1–65.

4. RESULTS AND DISCUSSION

20 models of neural networks were realized. The most important variables (listed in Table 1) i.e. learning errors and quality of learning, number of training epochs, activation functions, relative and absolute error, Pearson and determination coefficients were determined.

Table 1

Influence of used network architecture on the learning quality

Network type	Learning quality	Learning error	No. of training epochs	Activation function – neurones in a layer		Mean square error		Correlation coefficient	Determination coefficient
				hidden	output	absolute $\times 10^4$	relative $\times 10^{-2}$ [%]		
MLP6-10-1	0.6120	0.0000	1	log	log	2.63	2.64	0.6507	0.4234
MLP6-12-1	0.5941	0.0000	21	log	log	2.58	2.58	0.6394	0.4088
MLP6-30-1	0.9831	0.0000	9	lin	exp	2.01	2.01	0.7083	0.5017
MLP6-16-1	0.7903	0.0000	4	tan	log	1.78	1.78	0.8180	0.6691
MLP6-24-1	0.5781	0.0000	3	lin	exp	2.28	2.29	0.6116	0.3741
MLP6-27-1	0.9938	0.0000	21	tan	log	1.56	1.56	0.8496	0.7218
MLP6-12-1	0.9916	0.0000	19	tan	exp	1.30	1.31	0.9216	0.8494
MLP6-8-1	0.6690	0.0000	3	lin	tan	1.99	2.00	0.7183	0.5160
MLP6-15-1	0.7497	0.0000	4	lin	tan	1.70	1.71	0.8082	0.6531
MLP6-15-1	0.7861	0.0000	5	lin	tan	1.65	1.65	0.8317	0.6917
MLP6-28-1	0.7432	0.0000	4	lin	tan	1.94	1.95	0.7928	0.6285
MLP6-11-1	0.9519	0.0000	19	exp	log	0.756	0.758	0.9645	0.9303
MLP6-20-1	0.9865	0.0000	33	exp	log	0.831	0.833	0.9682	0.9375
MLP6-14-1	0.6595	0.0000	3	exp	tan	2.03	2.04	0.7116	0.5064
MLP6-20-1	0.5768	0.0000	11	log	log	2.61	2.61	0.6163	0.3798
MLP6-24-1	0.9092	0.0000	60	log	log	1.20	1.20	0.9183	0.8432
MLP6-14-1	0.5822	0.0000	5	lin	exp	2.35	2.35	0.6137	0.3766
MLP6-5-1	0.7741	0.0000	65	log	log	1.86	1.87	0.8136	0.6619
MLP6-2-1	0.9114	0.0000	13	log	lin	1.24	1.24	0.9056	0.8201
MLP6-22-1	0.7463	0.0000	4	tan	tan	1.85	1.85	0.7924	0.6278

Abbreviations: logistic – log, exponential – exp, tangential – tan, linear – lin.

Five models were chosen as the best ones. These optimum models (bold letters in Table 1) were determined by the lowest absolute mean-square errors (even very small

of the order of 10^{-5}) and the highest correlation coefficients in the range 90–96%. As can be seen, only 13–60 epochs of learning were sufficient to obtain consistent results of modelling. These selected models were characterized by all possible (used during the training of the network) activation functions. None of the function predominates. This fact suggests that the problem is quite complicated and should be solved by the combination of various mathematical relationships.

Table 2

Results of forecasting of the turbidity retention coefficient

Model	Absolute mean square error	Relative mean square error [%]	R_p	Correlation coefficient	Determination coefficient
MLP 6-12-1	2.16×10^{-4}	2.16×10^{-2}	0.9970–0.9978	0.8295	0.6881
MLP 6-11-1	2.67×10^{-4}	2.68×10^{-2}	0.9970–0.9977	0.5189	0.2692
MLP 6-20-1	2.96×10^{-4}	2.97×10^{-2}	0.9970–0.9976	0.5035	0.2535
MLP 6-24-1	2.20×10^{-4}	2.20×10^{-2}	0.9970–0.9976	0.6419	0.4120
MLP 6-2-1	2.35×10^{-4}	2.35×10^{-2}	0.9967–0.9976	0.6388	0.4081

In Table 2, results of prognosis for the turbidity retention coefficient (R_p) are shown for 5 optimum network models (cf. Table 1). The optimum model (bold letters) characterized by the lowest absolute mean square error (2.16×10^{-4}) had two times more hidden neurons than numbers of inputs. This fact is directly connected with the solved problem. Probably such a great hidden vector was necessary just to train the network correctly and to generalize the matter of forecasting the turbidity retention coefficient. As can be seen, all five models were characterized by the relative error at the level of 2×10^{-2} but generally in optimizing problems we approach the best solution. That is why the selected network was described by the relative mean square error equal to 2.16×10^{-2} . The range of changes of forecasted retention coefficient (R_p) is almost the same as the experimental one (R_e), which suggests that the prognosis is very precise. It is obvious that in learning the error is lower than in forecasting because the prognosis was done on a different data set. These data were not known previously during forecasting and that is why the correlation is a little bit worse in comparison to the training. The structure of the optimum network model is presented in Fig. 2.

Absolute and relative errors have been compared in the prognosis step because only in this process it was reasonable to check if the network results were convergent with experimental values. In all network models, the method of training based on the quasi-Newton approach was used as the best in comparison to fastest decline and conjugated gradient descent algorithms. The method seems to be the most effective. Unfortunately, the number of data used for training (18) and also in forecasting (12) was small and thus the errors were not as small as expected and the correlation coefficient equalled only to 82.95% in the forecasting step.

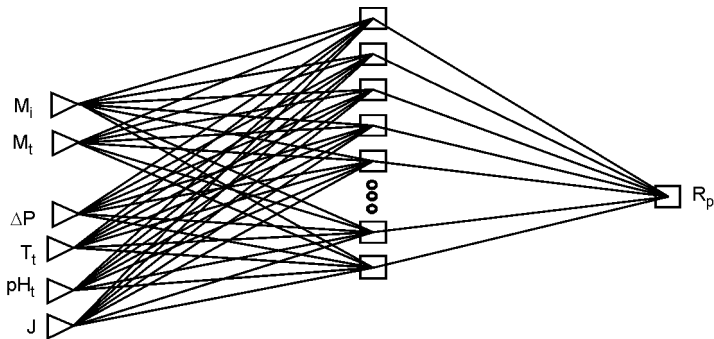


Fig. 2. Structure of the best network model

To obtain more reliable results, the network should be trained on the minimum one hundred data [15]. Only in such a case it could be possible to show the network great range of changes in the input signals. Despite usage of quite simple activation functions (hyperbolic tangent and exponential), the problem was solved with insufficient convergence (Fig. 3). Modelling using an artificial neural network has one disadvantage – the size of the training vector should be great enough to show the model the correct pattern of parameters and to obtain convergent results and small errors. Figure 3 shows only this quite great scatter of results because of an insufficient size of the learning vector. In the training process as well as in the forecasting step, the dispersion between experimental and predicted values of the retention coefficient is quite high. The conclusion drawn from Fig. 3 is obvious: the more experimental data, the greater the learning quality and the better results of forecasting are. Predicting the turbidity retention coefficient seems to be a crucial problem because knowledge about such a parameter allows us to design (having the information about the quantity of natural organic matter in water) the technological water treatment process properly. Probably the number of learning epochs should be higher than 19 to train properly in such cases when the number of variables is not sufficient. But in the case presented (the size of the learning vector is not significant) it is also a problem of overtraining: the network should be learnt to approximate but not to fit exactly the shown pattern just to predict in the future reliable results when the range of the input signals will change a little bit. The number of hidden neurons (12) seems to be sufficient because it is twofold more than the magnitude of input vector. It is not recommended to create the model which is too complicated in the structure. Nowadays the way of creating, learning and changing the model architecture is optimized. Hence the most important issue in ANN modelling is to receive the optimum (quite simple) model which could be adapted to only one problem. It is not possible to use the above created model to predict permeate turbidity after the ultrafiltration process without coagulation. It is a completely different optimizing problem due to changes in the operation conditions. The model is an assignment to only one kind of optimized question.

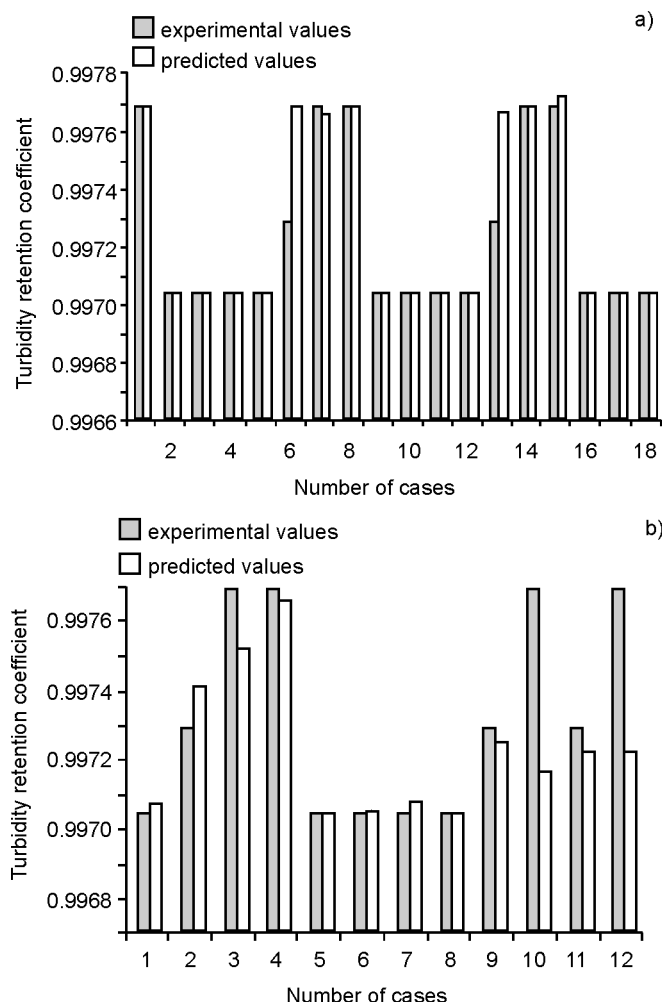


Fig. 3. Dispersion between experimental and predicted values during: a) learning, b) prognosis

It is clear that during the network learning the neurons were placed at various activation positions. Some neurons were activated more than others. The behaviour of the network is determined by changes in the activity of each single neuron. Negative values mean less active behaviour of the neuron. The higher was the value of the weight, the stronger influence and impact on the neuron. Very interesting is the fact that the highest value of weight (4.8748) was obtained between the transmembrane pressure and the first hidden neuron, while the lowest (-3.6701) was between pH in the tank and seventh hidden neuron. Probably this means that to forecast the turbidity retention coefficient data about the quality of raw water is not needed but rather the information

about the operation conditions (e.g. ΔP). As can be seen, pH has no influence (negative weight value) on satisfactory prediction of turbidity retention coefficient even when the ultrafiltration process is integrated with the coagulation.

5. CONCLUSIONS

The modelling of the turbidity retention coefficient using artificial neural networks might be summarized as follows:

- The optimum neural network model seems to be the great method of mathematical modelling due to lack of typical mathematical models solving problems of forecasting water quality after the treatment process.
- Absolute mean square error equal to 2.16×10^{-4} and the correlation coefficient at the level of 82% in the forecasting process can be acceptable from the engineering point of view, but the agreement between experimental and predicted values will be higher when the model is trained by the higher and more accurate variables.
- The most important role in predicting the turbidity retention coefficient is played by the transmembrane pressure because the value of the weight is in this case the highest.
- It should be remembered that ANN modelling is like a “black box” approach. Hence to achieve reliable solutions it is sometimes required to apply a “trial and error method” during creation of the network model.
- A created network could be used in the future for forecasting quality parameters of permeate in hybrid processes of reservoir water purification but only when the conditions of the membrane processes and the input signals are similar.

ACKNOWLEDGEMENTS

The authors express their gratitude to the Chair of Water Supply Engineering at the University of Technology in Dresden, especially to Andre Lerch, Susanne Müller and Professor Wolfgang Uhl for making available their experimental data for artificial neural network modelling.

SYMBOLS

ANN – artificial neural network

D – coagulant dose, g Al³⁺·m⁻³

J – real permeate flux in normal conditions, m³·m⁻²·d⁻¹

H – number of hidden neurons

I – number of input neurons

M_i – inlet turbidity of raw water, NTU

MLP – multilayer perceptron

M_p – permeate turbidity, NTU

M_t	– turbidity in the tank, NTU
O	– number of output neurons
ΔP	– transmembrane pressure, Pa
pH_t	– pH in the tank
R_e	– experimental turbidity retention coefficient
R_p	– predicted turbidity retention coefficient
T_t	– temperature in the tank, K

REFERENCES

- [1] KONIECZNY K., RAJCA M., BODZEK M., KWIECIŃSKA A., Environ. Prot. Eng., 2009, 35 (1), 5.
- [2] KOWALSKA I., Environ. Prot. Eng., 2010, 36 (3), 33.
- [3] MERDUN H., ÇINAR Ö., Environ. Prot. Eng., 2010, 36 (2), 95.
- [4] KABSCH-KORBUTOWICZ M., KUTYŁOWSKA M., Environ. Prot. Eng., 2008, 34 (1), 15.
- [5] RAZAVI S. M., MOUSAVI S. M., MORTAZAVI S. A., Chem. Eng. Sci., 2003, 58, 4185.
- [6] RAI P., MAJUMDAR G. C., DASGUPTA S., DE S., J. Food Eng., 2005, 71, 273.
- [7] GUADIX A., ZAPATA J., ALMECIJA C., GUADIX E., Desalination, 2010, 250, 1118.
- [8] STRUGHOLTZ S., PANGLISCH S., GEBHARDT J., RIMBEL L., J. Water Supply: Res. Techn. – AQUA, 2008, 57, 23.
- [9] CURCIO S., CALABRO V., IORIO G., Desalination, 2009, 236, 234.
- [10] HWANG T., CHOI Y., NAM S., LEE S., OH H., HYUN K., CHOUNG Y., Des. Water Treat., 2010, 15, 134.
- [11] AL-ABRI M., HILAL N., Chem. Eng. J., 2008, 141, 27.
- [12] MÜLLER S., UHL W.J., Water Supply: Res. Techn. – AQUA, 2009, 58, 170.
- [13] WÖLLNER A., *Untersuchungen zur Ultrafiltration von Uferfiltrat sowie deren Auswirkung auf eine nachfolgende Aktivkohlefiltration*, Master Thesis, Institute for Urban Water Management, Dresden University of Technology, 2004.
- [14] KABSCH-KORBUTOWICZ M., KUTYŁOWSKA M., Ochr. Środ., 2010, 32 (2), 23.
- [15] KABSCH-KORBUTOWICZ M., KUTYŁOWSKA M., Chem. Proc. Eng., 2009, 30, 307.

KATARZYNA PIEKARSKA*, MARZENA ZACIERA**,
ANNA CZARNY***, EWA ZACZYŃSKA***

APPLICATION OF SHORT-TERM TESTS IN ASSESSMENT OF ATMOSPHERIC AIR POLLUTION

Results of analyses of airborne particulates collected in winter and summer seasons from two locations of Wrocław (city centre and the outskirts area) have been presented. Samples of particulate matter were collected on sintered-glass filters, using a high performance air aspirator Staplex-PM10. Extraction with dichloromethane was carried out in a Soxhlet apparatus. Mutagenicity of dichloromethane extracts was studied based on a conventional *Salmonella* assay. Two *Salmonella typhimurium* strains TA98 and YG1041 were employed in the assay. Genotoxicity of organic air pollutants was detected using a miniaturized SOS chromotest obtained from EBPI (Brampton, Ontario, Canada). Bacterial assays were carried out with and without metabolic activation by the S9 microsomal fraction. Cytotoxicity of the particulate extracts was studied by the method of their direct contact with one-layer culture of human lung carcinoma epithelial cells – A549.

1. INTRODUCTION

Atmospheric air is a carrier for xenobiotics, action of which human organism is exposed to through a respiratory tract [1]. Most of air pollutants are gaseous. Another group of pollutants constitutes of particular matter (PM), which is a complex mixture of organic and inorganic substances. Particulate matter can take the form from submicro particle aerosols to easy visible dust particles. Depending on size of particles, the following PM fractions can be distinguished: PM10 – with particles diameters below 10 µm, PM5 – with particle diameters below 5 µm, PM2.5 – with particle diameters below 2.5 µm, and PM1 – with particles smaller than 1 µm [2]. Pollutants present in air adsorb on airborne particulates of different sizes. The fine particle fraction, of grain

*Institute of Environmental Protection Engineering, Wrocław University of Technology, Wybrzeże Wyspiańskiego 27, 50-370 Wrocław, Poland. Corresponding author, e-mail: katarzyna.piekarska@pwr.wroc.pl

**Institute of Occupational Medicine and Environmental Health, ul. Kościelna 13, 41-200 Sosnowiec, Poland.

***Institute of Immunology and Experimental Therapy, ul. Weigla 12, 53- 114 Wrocław, Poland.

size below 5 µm, shows the highest biological activity as it is able to penetrate to alveoli in the human and animal respiratory systems. Chemical compounds having effects on alveoli epithelial cells are gradually released from particulates retained in the alveoli. Then through the alveoli they get into the circulatory system and this way spread over the entire organism [3]. A major group, one relatively well recognized, includes polycyclic aromatic hydrocarbons (PAHs) – which are known of mutagenic and cancerogenic activity. It has been found that aromatic hydrocarbons are not the only cyclic compounds showing genotoxic effects and able to adsorb on dust particles. Also nitro-, chloro- and oxy- PAH derivatives as well as other yet unidentified chemical substances show significant mutagenic activity [3, 4].

Standard air tests do not cover determination of biological activity of pollutants present in the air. Assessment of air pollution level involves determination of concentrations for particulate matter and USEPA listed PAHs, followed by comparison of obtained values with those permitted by legal regulations. Such procedure provides knowledge only on current environment condition and does not give any indications as to the pollution effects on living organisms. Full chemical analysis of air pollution would be impracticable because of complexity of pollutant mixture composition and mutual interactions of pollutants in the mixture. Therefore a full chemical analysis cannot be taken as a basis for forecasting biological effects that might be produced by pollutants in humans and animals. Examination of atmospheric air particulate matter pollution using short-term tests may become an excellent tool in assessment of health hazard linked to the presence of chemical compounds adsorbed on airborne particulates [3, 4].

The purpose of this work was to determine genotoxicity and cytotoxicity of chemical pollutants adsorbed on particles from PM10 fraction collected in the Wrocław urban area. Wrocław is an urban-industrial agglomeration where air pollution comes from three sources: so called low-level emission, industrial nuisances and passenger car and goods traffic. The *Salmonella* plate test (Ames assay) of high forecasting power in relation to mutagenic and potentially cancerogenic agents was used in investigations and was considered the first short term test among the methods applied in genetic toxicology [5]. It is the most widely used bioassay in investigations on mutagenicity of atmospheric air particulates pollution [4]. Genotoxicity of organic air pollutants was detected by using the SOS chromotest. Few applications of the SOS chromotest have been reported in examination of particulate matter extracts and compared with respective results from the *Salmonella* assay [6, 7]. Cytotoxic effects of the particulate extracts in turn were investigated by the method of direct contact of the extracts with one layer culture of human lung carcinoma epithelial cells – A549. Lung epithelium cells are the first defense of the organism, ready to remove fine particles and bacteria from the respiratory system. Fitness of cell lines to evaluate cytotoxic properties of respirable particles was confirmed in numerous studies, and the recent investigations in Europe indicate that the smaller diameter of tested particles, the greater cytotoxic effect

is and thus their role in formation of DNA oxidative defects. The greatest cytotoxic effect can be observed in the case of particles from the PM0.2 fraction, and then the PM2.5–0.2 fraction; the least effect is produced by PM10–2.5 particles [8, 9].

2. MATERIALS AND METHODS

Air samples were collected using a high performance air aspirator Staplex PM-10, FC-2ETM model. The samples were taken during summer (samples I and II) and winter (samples III and IV) seasons from two city locations. The former sampling point was located in the Wrocław outskirts, at Strachocińska St. (samples I and III), in the low-rise residential housing area, close to quite a busy exit route from the town. The area has not been connected to a utility gas supply system, thus kitchen ranges are used in many houses all year round. The other sample collection point was located in the city centre, at Grunwaldzki Sq. which is cut along its long axis by the only transit route towards Warsaw. Heavy traffic is noted here 24 hours a day. Times of sample collection and sample volumes are presented in Table 1.

Table 1
List of data on collected PM10 samples

Type of sample	Collection time [h]	Air volume [m ³]	Mass of particulate matter [µg/m ³]	Mass of tar substances [µg/m ³]
I. Summer (Strachocińska St.)	67	4 542.6	57.17	19.90
II. Summer (Grunwaldzki Sq.)	96	6 474.9	38.33	26.68
III. Winter (Strachocińska St.)	119	8 035.0	138.93	145.15
IV. Winter (Grunwaldzki Sq.)	105	7 069.0	87.32	51.04

Antihygroscopic glass filters together with particulates from individual test cycles were combined into one sample, cut and placed in a Soxhlet apparatus. Then extraction was carried out using dichloromethane for 16 h plus 15 min reflux, without access of light. Extracts were thickened until dry in a vacuum evaporator and the dry residue was weighed in order to determine the amount of tar substances in samples. Obtained dry extracts were analysed to find PAH, nitro-PAH and dinitro-PAH content, they also were used in bioassays [4, 10, 11]. PAHs in the samples were determined by a high performance liquid chromatography technique using fluorescence detection, whereas the nitro-PAH content – by the gas chromatography using mass detection [12–14].

Mutagenicity of the particulate matter was evaluated based on a bacterial *Salmonella* test (Ames assay) [15]. It consists in checking whether the tested material causes reverse mutation (reversion) of special histidine dependent (*his*⁺) strains of *Salmonella*

typhimurium LT2 bacteria. Two test strains were used in investigations: *Salmonella typhimurium* TA98 and YG1041*. The TA98 strain detects mutagens of the reading frame shift type. The YG1041 strain is a derivative of the TA98 strain and shows increased sensitivity to nitro-, amino- and hydroxylamino-PAH derivatives [16]. The assay was carried out in experiment versions without metabolic activation, and with the metabolic activation by a microsomal fraction S9 activated with Aroclor 1254, and derived from Wistar rat liver. The microsomal fraction S9 was used in assays to induce metabolic activation of promutagens. Protein content in the fraction, as determined by Lowry's method, was 64.44 mg/cm³. S9-mix containing 4 vol. % of S9 was used in experiments. Each time before starting the experiments, genotypes of test strains were checked. Also the number of spontaneously induced revertants was determined (negative check) as was the number of revertants induced by the action of diagnostic mutagens (positive check). As diagnostic mutagens in experiments without metabolic activation by S9 fraction served: 2,4,7-trinitro-9-fluorenone (for TA 98 strain) and 2,6-dinitrotoluene (for YG 1041 strain), and in the case of experiments in the presence of the S9 fraction – 2-aminofluorene (TA98, YG1041).

Mutagenic effect of airborne particulates was presented in the form of the mutagenicity ratio (*MR*) calculated from the formula:

$$MR = \frac{n_i}{n_s},$$

where n_i denotes the number of induced revertants, and n_s – the number of spontaneous revertants. Samples were considered mutagenic if their mutagenicity ratios *MR* were equal or higher than 2.

Genotoxicity of organic air pollutants was detected using a miniaturized SOS Chromotest obtained from EBPI (Brampton, Ontario, Canada). The principle of the test is based on activation of DNA repair process – so called “SOS system”, in cells of *Escherichia coli* K12 PQ37 bacteria. Activation of the process indicates that DNA has been damaged. In the test strains, the SOS system operator's gene had been fused with a structural gene of the β-galactozidase enzyme. Expression of the SOS system genes is measured in the test under contact with the tested sample. Their action is measured by the β-galactozidase activity [17]. Individual dilutions of organic extracts of air pollutants were dissolved in DMSO and placed in microwells on test plates. The test was performed following the instructions attached to the test set. Experiments were carried with and without metabolic activation with the microsomal fraction S9. As diagnostic mutagens were used 4-nitroquinoline-N-oxide and 2-aminoanthracene. Absorbance was measured at 615 nm (genotoxic activity) and 405 nm (bacteria survival) on

**Salmonella* test strains were obtained from Dr. T. Nohmi, Division of Genetics and Mutagenesis, National Institute of Hygienic Sciences, Tokyo, Japan.

a spectrophotometer Sunrise (Tecan, Austria). The genotoxic effect of airborne particulates was evaluated in the form of induction factor (*IF*):

$$IF = \frac{R(C)}{R(0)},$$

where: $R(C)$ – specific activity of β -galactozidaze at a given concentration c of the tested sample, $R(0)$ – specific activity of β -galactozidaze for the negative control. The tested sample was considered genotoxic if the *IF* value was higher than 1.5.

Cytotoxicity of the particulate extracts was studied by the method of their direct contact with one-layer culture of human lung carcinoma epithelial cells – A549 (American Type Culture Collection, Cell Culture Line – ATCC CCL 185). Cultures of A549 cells were grown in Dulbecco culturing medium with addition of 10% inactivated (30 min, 56 °C) veal serum and 100 u/cm³ penicillin, 100 µg/cm³ streptomycin and 2×10⁻³ M L-glutamine. One-layer culture of A549 cells, of the density 2×10⁶/cm³, was placed on plastic 96-well plates and incubated for 24 h at 37 °C, in the ambient atmosphere of 5% CO₂. After that time the fluid from above the cells was removed, and tested extracts in corresponding concentrations were placed over one-layer cultures of the A549 cells. Then the cultures were incubated for 24, 48 and 72 h at 37 °C, in the atmosphere of 5% CO₂. Cell cultures without addition of tested samples, and the cell cultures with addition of DMSO in the same amount as in tested samples served as reference. Quantitative and morphological changes that occurred as the effect of addition of tested extracts were estimated after 24, 48 and 72 h using an inverted microscope. Minimum concentration of tested samples, yet producing degeneration in 50% of cells, was considered a toxic dose (Tissue Culture Cytotoxic Dose – TCCD₅₀) [18]. Results of the cytotoxic tests were presented as volumes of tested air (in m³) sufficient for obtaining the extracts that still would induce toxic effects.

3. RESULTS AND DISCUSSION

Concentrations of airborne particles in selected test points ranged from 38.33 µg/m³ (II) to 138.93 µg/m³ (III). Concentrations of tar substances ranged from 19.9 µg/m³ (I) to 145.15 µg/m³ (III). The highest amounts of particulates (138.93 µg/m³) and tar substances (145.15 µg/m³) were found in sample III (Table 1). The observed seasonal differences in those concentrations corresponded with literature reports [19, 20]. For the most part, the differences result from increased emission of particulates in urban agglomerations during winter seasons, due to combustion processes for heating purposes. Obtained PM10 amounts (38.33–57.17 µg/m³ in summer and 87.32–138.93 µg/m³ in winter) were close to the levels measured in spring–summer and

autumn–winter seasons in various European cities (Czech Republic, Italy, Belgium) [10, 21–23].

Table 2

PAH concentration in PM10 organic extracts [ng/m³]

Controlled WWA	Summer (I)	Summer (II)	Winter (III)	Winter (IV)
Fen	0.106	0.374	6.252	3.792
A	0.016	0.034	0.856	0.562
Flu	0.270	0.574	4.336	5.314
Pyr	0.150	0.360	11.244	4.58
B[a]A	0.088	0.174	4.24	1.32
Chr	0.120	0.220	3.1	2.28
B[b]F	0.518	0.654	2.8	0.372
B[k]F	0.164	0.222	1.844	0.85
B[a]P	0.514	0.438	7.788	2.65
D[a,h]A	0.242	0.194	0.364	0.224
B[g,h,i]P	0.154	0.366	0.984	2.19
I[1,2,3-c,d]P	n.d.	n.d.	0.384	1.69
Total	2.342	3.610	44.192	25.824

n.d. – not detected

Tested samples (Table 2) contained the same twelve PAHs as those in the list of regulated aromatic hydrocarbons. The highest PAH amount adsorbed on airborne particles was noted in winter season. Total PAH amount detected at that time ranged from 25.824 ng/m³ to 44.192 ng/m³, whereas in PM samples collected in summer – from 2.342 ng/m³ to 3.61 ng/m³. Three PAHs among those present in the samples, namely (benzo[a]anthracene, benzo[a]pyrene, dibenzo[a,h]anthracene) were classified by IARC in 2A group as probably carcinogenic to humans, and another three PAHs: (benzo[b]fluoranthene, benzo[k]fluoranthene, indeno[1,2,3-c,d]pyrene) were classified in 2B group, as possibly carcinogenic to humans [24]. All PM samples contained high percentage of benzo[a]pyrene, and its concentration ranged from 0.438 ng/m³ (II) to 7.788 (III) ng/m³. Benzo[a]pyrene is an indicator compound in relation to which compared is carcinogenic potential of other PAHs [24, 25]. A relative carcinogenicity index for that compound has been assumed 1. The only compound found to have higher carcinogenic potential is benzo[a]anthracene ($k = 5$), and its presence was also confirmed in the tested extracts. Benzo[a]pyrene content reached 1/5–1/10 of total content of all PAHs, i.e. from 10.3% (IV) to 21.9% (I) of total PAH concentration in tested extracts. Determined concentrations of individual PAHs were within the limits reported in the literature, and were very close to those detected in urban areas in Belgium and Prague [10, 22].

Also content of nitro-PAH derivatives was determined in tested PM samples (Table 3). Nitro-PAH derivatives because of their mutagenic activity are ranked among most hazardous chemicals for human health. The studies carried out so far indicate that the nitro-PAH concentration in the air is low, which brings about considerable analytic problems [12, 14]. Certain nitro-PAHs can be formed during combustion processes. They are present for instance in extracts of particles sampled from exhaust gas of diesel engines (e.g. nitrofluorene, nitroanthracene, nitrofluoranthene, nitrobenzo[a]pyrene). However, majority of them are produced in atmospheric air as a result of PAH reaction with nitrogen oxides in gaseous phase.

Table 3

Table 3. Nitro-PAH concentration in PM10 dust extracts [ng/m³]

Controlled nitro-PAH	Sample			
	Summer (I)	Summer (II)	Winter (III)	Winter (IV)
1-Nitronaphthalene	0.45	n.d.	0.83	0.45
2-Nitrofluorene	0.28	0.29	3.36	1.41
9-Nitroanthracene	n.d.	n.d.	1.84	0.74
3-Nitrofluoranthene	n.d.	n.d.	0.6	0.3
1-Nitropyrene	n.d.	n.d.	0.42	0.26
1,3-Dinitropyrene	n.d.	n.d.	n.d.	n.d.
1,6-Dinitropyrene	n.d.	n.d.	n.d.	n.d.
1,8-Dinitropyrene	n.d.	n.d.	n.d.	n.d.
Total	0.73	0.29	7.05	3.16

n.d. – not detected.

Nitro-PAHs occur in lower concentrations than non-substituted aromatic hydrocarbons, nevertheless they are very stable in solid phase, and as compared with PAHs – some of them have higher mutagenic (2×10^5 times) and cancerogenic (10 times) power [14]. Total content of those compounds in tested samples ranged from 0.29 ng/m³ (II) to 7.05 ng/m³ (III). The selected dinitro-PAHs were not found in extracts within their determination limits. Although observed were PAH mononitroderivatives, among others 2-nitrofluorene and 1-nitropyrene, both ranked in the 2B group. 2-Nitrofluorene was present in all tested samples, while 1-nitropyrene was found only in winter-collected samples. Large amounts of 2-nitrofluorene were detected in winter-collected samples. That compound comprised near half of the nitro-PAH content in those extracts. Its amount in the sample collected in summer (I) reached ca. 38%. Its largest amount was found in sample II (summer), even 100%, as it was the only mononitroderivative detected in that collection point. The largest number of compounds classified as PAH nitro derivatives was detected in winter-collected PM samples. Their highest concentration was found in sample III collected in winter at the Strachocińska St. The concentration reached 7.05 ng/m³.

Table 4

MR ± S.D. for various concentrations of PM extracts from tested air samples, determined by *Salmonella* assay in TA 98 strain conducted in the presence and in the absence of S9 fraction^a

Sample concentration [m ³ /plate]	Sample							
	Summer (I)		Summer (II)		(Winter (III))		Winter (IV)	
	-S9	S9	-S9	S9	-S9	S9	-S9	S9
50	3.49±0.2	2.62±0.2	0.43±0.2	0.57±0.1	9.29±0.3	17.7±0.4	31.73±0.6	18.28±0.4
25	2.2±0.2	2.32±0.2	1.78±0.3	0.85±0.2	12.49±0.5	13.14±0.2	28.52±0.5	15.98±0.5
12.5	1.82±0.1	1.35±0.1	2.05±0.1	11.04±0.2	13.63±0.4	11.52±0.2	20.68±0.7	13.41±0.3
6.25	1.55±0.2	1.35±0.2	2.67±0.2	17.9±0.3	9.19±0.3	10.29±0.3	10.31±0.4	10.9±0.4
3.125	1.45±0.2	1.15±0.2	15.5±0.3	16.34±0.4	5.91±0.3	4.85±0.4	10.15±0.4	6.95±0.2
1.56	1.35±0.1	1.08±0.2	8.41±0.2	9.64±0.2	4.27±0.2	3.85±0.2	5.93±0.2	6.8±0.1
0.78	1.29±0.1	1.04±0.3	2.94±0.4	8.5±0.2	3.7±0.3	2.87±0.2	5.1±0.2	6.34±0.3
0.39	1.25±0.1	0.92±0.2	1.43±0.1	5.12±0.2	2.76±0.2	2.77±0.2	5.09±0.3	4.73±0.4
0.195	1.19±0.2	0.92±0.2	1.16±0.1	3.13±0.1	1.83±0.2	2.23±0.1	4.6±0.1	2.94±0.2
0.097	1.12±0.2	0.77±0.3	1.09±0.1	2.27±0.1	1.71±0.2	1.81±0.1	4.04±0.2	1.6±0.2
0.049	1.06±0.1	0.77±0.2	1.01±0.1	1.16±0.1	1.67±0.1	1.45±0.1	2.41±0.2	1.29±0.1
0.0245	1.06±0.3	0.73±0.2	0.93±0.1	0.67±0.1	1.07±0.1	1.25±0.1	1.42±0.1	1.08±0.1

^aNegative check 22–36 revertants per plate. Positive check 3242–4552 revertants per plate (-S9), 1645–1886 revertants per plate (S9).

Table 5

MR ± S.D. for various concentrations of PM extracts from tested air samples, determined by *Salmonella* assay in YG 1041 strain conducted in the presence and in the absence of S9 fraction^a

Sample concentration [m ³ /plate]	Sample							
	Summer (I)		Summer (II)		(Winter (III))		Winter (IV)	
	-S9	S9	-S9	S9	-S9	S9	-S9	S9
50	2.96±0.4	2.63±0.4	2.85±0.2	2.34±0.1	3.69±0.3	1.16±0.1	9.54±0.4	10.45±0.3
25	7.29±0.2	4.56±0.2	4.84±0.3	2.86±0.3	6.06±0.2	5.06±0.2	15.81±0.5	11.9±0.4
12.5	4.75±0.3	2.52±0.3	6.4±0.4	3.66±0.2	8.57±0.4	7.33±0.4	16.48±0.4	12.52±0.3
6.25	2.34±0.2	1.92±0.2	3.21±0.1	1.05±0.1	5.96±0.3	6.61±0.3	13.71±0.3	15.0±0.2
3.125	1.93±0.1	1.66±0.2	2.42±0.1	0.99±0.1	5.39±0.2	4.25±0.3	10.64±0.2	14.49±0.3
1.56	1.53±0.2	1.49±0.1	1.95±0.1	0.99±0.2	4.35±0.2	3.58±0.2	10.36±0.2	12.43±0.2
0.78	1.32±0.2	1.43±0.1	1.51±0.1	0.93±0.1	3.92±0.2	3.41±0.2	10.33±0.2	11.92±0.3
0.39	1.16±0.1	1.32±0.1	1.22±0.1	0.9±0.1	2.91±0.2	2.39±0.2	9.23±0.3	6.3±0.2
0.195	1.14±0.1	1.18±0.1	0.95±0.2	0.85±0.2	2.58±0.1	1.87±0.1	7.75±0.4	5.2±0.2
0.097	1.11±0.1	0.92±0.1	0.84±0.1	0.85±0.1	2.41±0.1	1.55±0.1	4.89±0.2	4.3±0.2
0.049	0.91±0.1	0.99±0.1	0.75±0.1	0.8±0.1	1.22±0.1	1.37±0.1	3.87±0.2	3.64±0.2
0.0245	0.83±0.1	1.00±0.1	0.74±0.2	0.86±0.1	1.10±0.1	1.01±0.1	2.51±0.2	3.05±0.2
0.0061	0.95±0.1	0.97±0.1	0.8±0.1	0.89±0.1	1.09±0.1	0.93±0.1	2.11±0.1	2.32±0.1
0.0015	0.97±0.1	1.00±0.1	0.9±0.1	0.91±0.1	1.11±0.1	0.94±0.1	1.23±0.1	1.36±0.1

^aNegative check 128–179 revertants per plate. Positive check 1165–1396 revertants per plate (-S9), 1126–1216 revertants per plate (S9).

Tested extracts produced mutagenic effects in both used strains (Tables 4 and 5). The winter-collected PM samples showed higher mutagenic activity than those collected in summer, which is in line with results reported by other authors [4]. The tested samples contained pollutants able affect genetic material indirectly or directly as well. As the evidence for that can be considered high mutagenicity ratios (*MR*) obtained in experiments carried out in the presence of the microsomal fraction S9 and without it as well. For the YG1041 strain higher *MR* values were obtained from assays carried out without using the S9 fraction. Thus that strain was the most sensitive to direct mutagens present in the tested samples. Higher *MR* values were obtained for samples collected in the city centre than for samples from the outskirts of the town. Only from assays carried out for pollutants collected in summer and using the YG1041 strain, higher *MR* values were obtained for the sample collected on the outskirts of the town (I). The highest *MR* values were obtained for extracts of particulates collected in winter in the city centre, when the TA98 strain was employed in assays. The respective values were: 31.73 ± 0.6 in the case of assays carried out without the S9 fraction and 18.28 ± 0.4 in assays carried out in the presence of the S9 fraction. For that sample also the highest *MR* values were obtained from assays carried out using the YG1041 strain, respectively: 16.48 ± 0.4 ($-S9$) and 15.0 ± 0.2 (S9). Maximum *MR* values for individual tester strains were obtained at various concentrations of particulates introduced into assays which is evidence for their differentiated sensitivity to tested compounds. Within the tested range of air extract concentrations (50 – $0.0015\text{ m}^3/\text{plate}$), a distinct dose–response curve was observed, describing fully the biological effects of pollutants present in extracts, depending on their concentration. Owing to a broad range of tested air sample concentrations in case of YG1041 strain (Table 6), it was possible to determine an inflexion point on the dose-response curve (toxic effect). In case of TA98 strain such effect was obtained with the sample II (summer – city centre) and the sample III (winter – town outskirts) from assays carried out in the absence of S9 fraction. In case of other extracts even at pollutant concentrations derived from 50 m^3 of air the threshold points of their toxic effects and thus the air volumes producing maximal mutagenic effect. The least volumes of polluted air, producing mutagenic effect in strains used in assays varied greatly. Detection threshold of the TA98 strain was in the order of 0.049 – 0.39 m^3 for winter conditions and 0.097 – 25 m^3 for summer conditions. And the respective detection thresholds of the YG1041 strain were 0.0061 – 0.39 m^3 for winter conditions and 3.125 – 12.5 m^3 for summer conditions. There was no significant relation between the PM concentration and the polluted air volume that produced mutagenic effect. The highest particulate matter concentration, $138.93\text{ }\mu\text{g/m}^3$, was obtained for the sample III (winter – town outskirts), whereas the highest concentration of adsorbed mutagenic compounds was found for the sample IV (winter – city centre). The particulates concentration for that sample was 1.5 times lower, i.e. $87.32\text{ }\mu\text{g/m}^3$. Similar situation was observed for pollutants collected in summer. The highest particulate matter concentration was obtained for the sample I (summer – town out-

skirts): 57.17 µg/m³, while the least volume of polluted air, producing mutagenic effect was found for the sample II (summer – city centre). The concentration of particulates for that sample was also about 1.5 times lower, which was 38.33 µg/m³. Particulate matter collected in the city centre area (samples II and IV) contained higher total PAH amount, although percentages of individual PAHs in the samples varied considerably.

Table 6

IF values for particulate pollution extracts determined with SOS Chromotest^a

Sample concentration [m ³ /well]	Sample							
	Summer (I)		Summer (II)		Winter (III)		Winter (IV)	
	-S9	S9	-S9	S9	-S9	S9	-S9	S9
50	1.89	1.32	4.12	3.80	TOX	TOX	TOX	TOX
25	1.56	1.24	3.90	2.50	TOX	3.78	TOX	5.27
12.5	1.40	1.14	3.20	1.95	5.12	3.46	TOX	5.01
6.25	1.32	1.09	2.45	1.54	4.97	2.57	9.34	4.56
3.125	1.27	1.12	1.65	1.40	3.20	1.80	7.17	3.12
1.56	1.20	1.08	1.30	1.38	2.69	1.65	5.61	2.01
0.78	1.17	1.00	1.21	1.25	1.68	1.45	3.98	1.76
0.39	1.12	0.98	1.15	1.20	1.54	1.21	2.19	1.40
0.195	1.10	1.05	1.05	1.15	1.40	1.19	1.63	1.32
0.097	1.00	0.95	0.95	1.05	1.34	1.13	1.42	1.30
0.049	1.05	0.91	1.10	0.95	1.25	1.17	1.41	1.23
0.0245	1.10	1.03	1.00	1.00	1.19	1.08	1.32	1.10
0.0061	0.97	1.11	0.89	1.00	1.05	1.00	1.11	1.07
0.0015	1.00	1.00	0.95	1.05	0.97	1.05	1.02	1.01

^aTOX – toxic sample.

Results of investigations on genotoxic activity of PM extracts, carried out using a miniaturized bacterial screening test called the SOS Chromotest are presented in Table 6. Tested extracts revealed genotoxic properties in the *Escherichia coli* K12 PQ37 strain used in the test. The *IF* values obtained from all conducted tests for samples collected in summer and in winter alike exceeded 1.5 and showed a linear dose-response relationship. For pollutants present in tested extracts, higher *IF* values were obtained from tests carried out without metabolic activation, and furthermore, the obtained *IF* values were higher for samples collected in winter as compared to the *IF* values for summer-collected samples. Thus the results indicate that chemical compounds effecting directly on genetic material prevail in tested extracts. The direct genotoxicity of organic air pollution is related to the presence of such compounds as nitro-, hydroxy- and oxy- PAH derivatives in the tested extracts [4, 26, 27]. Moreover, higher *IF* values were obtained for extracts of particulate matter collected in the city

centre area (II, IV – Grunwaldzki Sq.) as compared with the *IF* values obtained for samples collected on outskirts of the town (I, III – Strachocińska St. Volumes of polluted air that induced the mutagenic effect were larger than those obtained from the *Salmonella* assay; they oscillated around 3.125–25 m³ in summer and 0.195–1.56 m³ in winter.

Table 7

Effects of particulate pollution extracts on A549 line
human lung cells, obtained from *in vitro* tests^a

Contact duration	Type of sample	Toxic effect [m ³]							
		50	25	12.5	6.25	3.13	1.56	0.78	0.39
24	Summer (I)	t	t	n	n	n	n	n	n
	Summer (II)	t	t	t	n	n	n	n	n
	Winter (III)	t	t	t	t	t	n	n	n
	Winter (IV)	t	t	t	t	t	t	n	n
	Control sample A549	n	n	n	n	n	n	n	n
48	Summer (I)	t	t	n	n	n	n	n	n
	Summer (II)	t	t	t	n	n	n	n	n
	Winter (III)	t	t	t	t	t	n	n	n
	Winter (IV)	t	t	t	t	t	t	n	n
	Control sample A549	n	n	n	n	n	n	n	n
72	Summer (I)	t	t	n	n	n	n	n	n
	Summer (II)	t	t	t	t	n	n	n	n
	Winter (III)	t	t	t	t	t	t	t	n
	Winter (IV)	t	t	t	t	t	t	t	n
	Control sample A549	n	n	n	n	n	n	n	n

^an – non-toxic sample, t – toxic sample.

Investigations on organic air pollution by application of the SOS chromotest have been reported in the literature by far less in comparison with those based on the *Salmonella* assay. However all such reports emphasize great usefulness of this test in monitoring of air pollution. Research conducted in Czech Republic and in Bosnia and Herzegovina by Škarek et al. [6, 7] has shown considerable variation of results obtained in the test. In Czech Republic, particulates were sampled in July 2002 in heavily urbanized regions (2 locations) and poorly urbanized regions (2 locations). Positive results of the tests were obtained only in two urban locations, from tests carried out without metabolic activation. Although in tests carried out in May 2004 in a poorly industrialized Sarajevo and heavily industrialized Tuzla – all tests yielded positive results, irrespectively of whether the S9 fraction was present or not. However, similar as in the research presented here, greater genotoxic power was observed for samples collected in heavily industrialized area and tested without metabolic activation.

Results of investigation regarding the effect of tested PM extracts in the lung carcinoma cells of the A549 line have been given in Table 7. According to many researchers, in the assessment of harmful effects of chemical compounds on human organism, results of mutagenicity and genotoxicity studies should be considered in correlation with corresponding results from toxicity studies. When testing substances that penetrate the organism through a respiratory tract, cell lines derived from pulmonary alveoli epithelial cells as well as the lines derived from macrophages are used. Epithelial cells of the respiratory system and macrophages of the pulmonary alveoli, through the process of respirable particle phagocytosis, constitute the organism defense against penetrating pollutants. Cytotoxicity and mutagenicity studies under *in vitro* conditions have proved that the human A549 cell line produced from neoplastic cells of pulmonary carcinoma will be useful in examination of properties of respirable particles [9, 11, 28]. The essence of mutation consists in irreversible damage in genetic material of a cell, which leads to changes in its functioning, which in turn results in its insusceptibility to mechanisms that regulate the rate of cell division, growth and differentiation. If the modified cells that build the human body are not eliminated in the early phase by the immune system, they will begin to proliferate, which may lead to a neoplasm formation [12].

The research covered toxic effects of organic pollutants adsorbed on particular matter collected in winter and in summer alike on cells of the A549 line under *in vitro* conditions. Air concentrations that caused toxic effects varied, depending on sampling season and contact time of the tested pollutants with the cell line. Stronger toxic effect was noted in the case of PM extracts collected in winter as compared with those summer-collected. Similar seasonal variability of the cytotoxic effect was observed in other cities [9, 11, 28]. After 24, 48, as well as after 72 h in observation, the lethal effect in 50% of tested cells was caused by smaller doses of winter-sampled air versus the air doses collected in summer. In the case of extracts of airborne particulates sampled in winter the air volumes were: 1.56 m³ (IV) and 3.13 m³ (III) after 24 and 48 h of contact, and 0.78 m³ for both samples after 72 h of contact. In the case of samples collected in summer, the toxic effect in A549 cells was observed after 24 and 48 h of exposure to pollutants derived from 12.5 m³ of air collected at Grunwaldzki Sq. location (II) and from 25 m³ of air collected at Strachocińska St. (I). The strongest toxic effect induced by the summer-collected samples was observed for sample II after 72 h in exposure. The air dose inducing such effect after that time of exposure was 6.25 m³. Whereas the dose of PM pollutants collected at Strachocińska St. and inducing the toxic effect was 25 m³, which is the same as after 24 and 48 h exposure.

4. SUMMARY

The investigations have confirmed high sensitivity of employed *Salmonella typhimurium* TA98 and YG1041 tester strains as well as the *Escherichia coli* K12 PQ37 to

organic pollutants adsorbed on airborne particulates of the PM10 fraction, which provided evidence for occurrence of PAHs and their nitro-, amino- and hydroxylamino-derivatives in atmospheric air. *MR* and *IF* values obtained in both bacterial tests indicated that chemical compounds of both promutagen and direct mutagen nature were present in tested samples, and moreover, similar *MR* values were obtained in the *Salmonella* assay from experiments carried out with metabolic activation by the microsomal fraction S9 as well as in the absence of the S9 fraction. By including the YG series strains in the assays, it was possible to confirm that moderately and highly polar classes of compounds are responsible for the mutagenic effect of air pollutants, and besides that, to detect the presence of mutagens in very small volumes of sampled air, of the range of 0.0061–0.049 m³. Considering the results obtained from the SOS Chromotest, higher genotoxicity was found in tests carried out without metabolic activation than in the presence of the microsomal S9 fraction. Among chemical compounds capable of producing such effects are nitro- and amino PAH derivatives, polar aromatic compounds, heterocyclic compounds and phenols.

It was also confirmed in the presented studies that organic pollutants adsorbed on airborne particulate matter and sampled in winter and in summer alike show toxic effects in A549 line cells under *in vitro* conditions. After 24, 48, as well as after 72 h in observation, the lethal effect in 50% of tested cells was caused by smaller doses of air when the air samples were collected in winter than in the case of air samples collected in summer.

The only way to provide integrated and quick estimation of human exposure to chemicals adsorbed on airborne particulate matter is implementation of biological monitoring. Because of complexity of the carcinogenesis, it is necessary to adopt suitable organisms, cells and short-term test systems. Use of human cell cultures in research, along with bacterial assays, will provide opportunity to get a correct response of mammal cells to organic compounds that are pollutants of the atmospheric air.

ACKNOWLEDGEMENTS

The project was carried out within the grant No. N N523 612939 (2010–2013) awarded by the Polish Ministry of Science and Higher Education.

REFERENCES

- [1] BRUNEKREEF B., HOLGATE S.T., Lancet, 2002, 360, 1233.
- [2] DE KOK T.M.C.M., DRIECE H.A.L., HOGERVORST J.G.F., BRIEDE J.J., Mutat. Res.-Rev. Mut. Res., 2006, 613 (2–3), 103.
- [3] COHEN A.J., Environ. Health Persp., 2000, 108 (4), 743.
- [4] CLAXTON L.D., MATTHEWS P.P., WARREN S.H., Mutat. Res., 2004, 567, 347.
- [5] MORTELMANS K., ZEIGER E., Mutat. Res., 2000, 455, 29.

- [6] ŠKAREK M., JANOŠEK J., ČUPR P., KOHOUTEK J., NOVOTNÁ-RYCHETSKÁ A., HOLOUBEK I., Environ. Int., 2007, 33, 859.
- [7] ŠKAREK M., ČUPR P., BARTOŠ J., KOHOUTEK J., KLÁNOVÁ J., HOLOUBEK I., Sci. Total Environ., 2007, 384, 182.
- [8] RISOM L., MØLLER P., LOFT S., Mutat. Res., 2005, 592, 119.
- [9] GÁBELOVÁ A., VALOVICOVÁ Z., BACOVÁ G., LÁBAJ J., BINKOVÁ B., TOPINKA J., SEVASTYANOVA O., ŠRÁM R.J., KALINA I., HABALOVÁ V., POPOV T.A., PANEV T., FARMER P.B., Mutat. Res., 2007, 620, 103.
- [10] BINKOVÁ B., ČERNA B., PASTORKOVÁ A., JELÍNEK R., BENEŠ I., NOVÁK J., ŠRÁM R.J., Mutat. Res., 2003, 525, 43.
- [11] PIEKARSKA K., ZACIERA M., CZARNY A., ZACZYŃSKA E., Environ. Prot. Eng., 2009, 35 (1), 37.
- [12] ZACIERA M., *Nitro-PAH determination in air*, [In:] *Protection of Air in Theory and the Practice*, J. Konieczyński (Ed.), Institute of Environmental Engineering of the Polish Academy of Sciences, Zabrze, Poland, 2006, p. 212, (in Polish).
- [13] PRYČEK J., CIGANEK M., ŠIMEK Z., J. Chromatogr., 2004, 1030, 103.
- [14] BAMFORD H.A., BEZABEH D.Z., SCHANTZ M.M., WISE S.A., BAKER J.E., Chemosphere, 2003, 50, 575.
- [15] MARON D.M., AMES B.N., Mutat. Res., 1983, 113, 173.
- [16] HAGIWARA Y., WATANABE M., ODA Y., SOFUNI T., NOHMI T., Mutat. Res., 1993, 291, 171.
- [17] QUILLARDET P., HOFNUNG M., Mutat. Res., 1985, 147, 65.
- [18] MENDYKA B., RADEK P., WARGACKA A., CZARNY A., ZACZYŃSKA E., PAWLIK M., Med. Środ., 2005, 8 (2), 139.
- [19] CREBBELLI R., FUSELLI S., BALDASSARRI L.T., ZIEMACKI G., CARERE A., BANIGNI R., Int. J. Environ. Health Res., 1995, 5, 19.
- [20] WOROBIEC A., ZWOŹDZIAK A., SÓWKA I., ZWOŹDZIAK J., STEFANIAK E. A., BUCZYŃSKA A., KRATA A., VAN MEEL K., VAN GRIEKEN R., GÓRKA M., JĘDRYSEK M.-O., Environ. Prot. Eng., 2008, 34 (4), 81.
- [21] GILLI G., TRAVERSI D., ROVERE R., PIGNATA C., SCHILIRO T., Environ. Res., 2007, 103 (1), 1.
- [22] DU FOUR V.A., JANSSEN C.R., BRITS E., LAREBEKE N.V., Mutat. Res.-Genet. Toxicol. Environ. Mutag., 2005, 588 (2), 106.
- [23] DU FOUR V.A., VAN LAREBEKE N., JANSSEN C.R., Mutat. Res., 2004, 558, 155.
- [24] NISBET I.C.T., LAGGY P.K., Reg. Toxicol. Pharmacol., 1992, 16, 290.
- [25] ATKINSON R., AREY J., Environ. Health Perspect., 1994, 102, 117.
- [26] ČERNA M., POCHAMANOVA D., PASTORKOVÁ BENEŠ I., LENIČEK J., TOPINKA J., BINKOVÁ B., Mutat. Res., 2000, 469, 71.
- [27] BRITS E., SCHOETERS G., VERSCHAEVE L., Environ. Res., 2004, 96, 109.
- [28] GÁBELOVÁ A., VALOVICOVÁ Z., HORVÁTHOVÁ E., SLAMEŇOVÁ D., BINKOVÁ B., ŠRÁM R.J., Farmer P.B., Mutat. Res., 2004, 563, 49.

MICHał GŁOMBA*, ELŻBIETA SZMIGIELSKA*

IMPACT OF LIMESTONE GRINDING DEGREE ON THE VOLUME OF THE ABSORPTION SUSPENSION TANK IN FLUE GAS DESULPHURIZATION SYSTEMS

The impact of the reagent (limestone) grinding degree, of its dissolution rate and pH of the absorption suspension used in flue gas desulfurization systems on the working volume of the reactor tank in the flue gas SO₂ absorption unit has been discussed. A correlation equation, defining the dependence of the reactor tank working volume on the parameters under investigation has been presented.

1. INTRODUCTION

Overly low tank volumes may result in excessive circulation of the absorption suspension in the SO₂ absorption unit (increased *L/G* ratio), and therefore in increased demand for electrical power consumed by the circulation pump engines, and in reduced degree of exploitation of the ground limestone in the absorption suspension. On the other hand, overly high tank volumes lead to increased investment costs and spatial demands with regard to the location of the tank in the flue gas desulfurization (FGD) systems. The retention time of the suspension in the tank and the volume of the tank working together with the absorber must be appropriately integrated.

From the analysis of unit processes occurring in the tank (dissolution of the ground limestone, oxidation of sulfites in the suspension, crystallization of calcium sulfate – synthetic gypsum) and the conclusions from the practice in the field of flue gas desulfurization, it may be inferred that the desulfurization degree depends on: the size of the sprayed droplets of the absorption suspension, the droplet residence time in the absorption zone, the amount of the suspension flowing down the absorber walls, the distribution of flue gas velocities within the absorber, chemical composition of the

*Research and Didactic Unit of Atmosphere Protection, Institute of Environmental Engineering, Wrocław University of Technology, Wybrzeże Wyspiańskiego 27, 50-370 Wrocław, Poland. Corresponding author M. Głomba, e-mail: michał.głomba@pwr.wroc.pl

flue gas and the suspension sprayed in the absorber, SO₂ and oxygen concentrations in the flue gas and sodium and magnesium ions concentration in the liquid. Also important are the parameters affecting the pH value of the absorption suspension: limestone grinding degree, grindstone dissolution rate and its reactivity towards SO₂, as well as CaCO₃ content, retention time of limestone in the reactor tank and the temperature of the process.

2. LIMESTONE DISINTEGRATION

In most cases, the goal of limestone disintegration is to increase the specific surface area of the solid phase in order to accelerate e.g., dry or wet boiler gas desulfurization. Mechanical disintegration may be achieved in two ways. In the case of limestone (Mohs scale hardness of 3.0 [1]), the disintegration process is started in jaw, cone and roll crushers (preliminary and medium disintegration). Proper disintegration consists of fine and very fine grinding, usually in ball mills.

Disintegration of solids is characterized by an index known as the disintegration degree [1]:

$$n = \frac{d_{p1}}{d_{p2}}, \quad (1)$$

where: d_{p1} – largest raw material particle size, d_{p2} – largest product particle size.

The relationship between the type of disintegration and the degree of disintegration is presented in Table 1.

Table 1

Disintegration degrees achieved in various disintegration operations [1]

Operation	Disintegration degree, n	Largest product particle size, d_{p2} [mm]
Crushing preliminary medium	3–6	>50
	4–10	5–50
Coarse grinding	5–10	0.5–5
Grinding fine very fine colloidal	10–50	0.05–0.5
	>50	0.005–0.05
	>50	<0.005

Disintegration in crushers is usually performed in dry conditions, while grinding can be performed in both dry and wet conditions. Wet grinding is characterized by lower energy demand and elimination of dust formation and convection. Dry grinding

is accompanied by less abrasive wear of the steel grinding elements, and thus lower oxide contamination of the ground product.

Grindability of the same material collected from different beds may vary. To allow differentiation in grindability, enabling the comparison of various materials and solid grinding devices were introduced such as: material grindability, specific material flow capacity and unit grinding workload.

Grindability is defined by the following equation:

$$M = \frac{\dot{m}}{\dot{m}_{st.c}}, \quad (2)$$

where: \dot{m} – flow capacity of the material in the mill, kg/s, $\dot{m}_{st.c}$ – flow capacity of standard coal in the same mill, kg/s [2, 3].

3. REACTIVITY OF GROUND LIMESTONE

Limestone reactivity was determined by static titration of limestone suspension with 1 M sulfuric acid at constant pH corresponding to the project specific value (e.g. pH = 5.2) and at predefined temperature, corresponding to the project specific temperature of the absorption suspension in the reactor tank, e.g. 55 °C for flue gas emitted from an anthracite boiler and 65 °C for flue gas emitted from a lignite boiler [3]. Consumption of sulfuric acid until a constant pH value is achieved (e.g., pH = 5.2) is recalculated as a degree of ground limestone conversion, which is then compared to reference limestone meal giving acceptable FGD results. Overall test time is 60 min. The lower and upper limits of the reference limestone meal reactivity [4] are presented in Fig. 1.

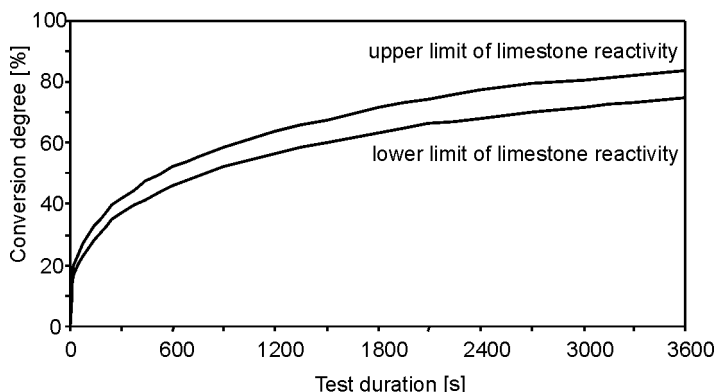


Fig. 1. Lower and upper limits of the reference limestone meal reactivity

Mokrosz [5] conducted reactivity tests for eight selected European carbonate based sorbents and chalk [5]. The results of this research are presented in Table 2.

Table 2

Results of reactivity tests for selected carbonate-based sorbents [5]

No.	Sorbent	CaCO ₃ content [%]	D ₄₃ *[μm]	Conversion rate after 60 min [%]
1	chalk	96.50	1.92	72
2	sorbent 6	97.24	3.28	60
3	sorbent 2	97.04	3.96	50
4	sorbent 7	95.40	6.27	40
5	sorbent 3	96.57	7.99	39
6	sorbent 4	95.36	7.62	35
7	sorbent 8	95.10	9.73	30
8	sorbent 5	96.36	9.72	30
9	sorbent 1	93.70	2.57	22

D₄₃* – mean mass diameter (de Brouckere mean diameter).

The reactivity of the sorbents depends on the grinding degree and CaCO₃ content. Comparison of sorbents 7, 3, 4, 8 and 5, where CaCO₃ was found at concentrations of over 95%, shows large differences in reactivity. The reactivity is clearly reduced with the increase of the particle mean diameter. At the same time, sorbent 1, despite a relatively high grinding degree, is poorly reactive as it contains a small amount of CaCO₃. The results obtained for different sorbents [5], varying in terms of reactivity, allowed to identify one that was best for use in FGD systems.

4. GROUND LIMESTONE DISSOLUTION RATE

Kuciel [6] studied the rate of dissolution of ground limestone in the tank and its impact on selected parameters of SO₂ absorption in FGD systems. He collected three samples of ground limestone used in three flue gas desulfurization systems. The grain size distribution of the collected samples is presented in Fig. 2. The grain size is characterized by the volume/surface mean diameter (Sauter mean diameter) of the particles. The goal of the study was to determine the coefficient characterizing the kinetics of dissolution of limestone samples in the absorption suspension defined by:

$$\frac{dR}{dt} = -k, \quad (3)$$

where: R – radius of a spherical limestone particle, μm, t – time, s.

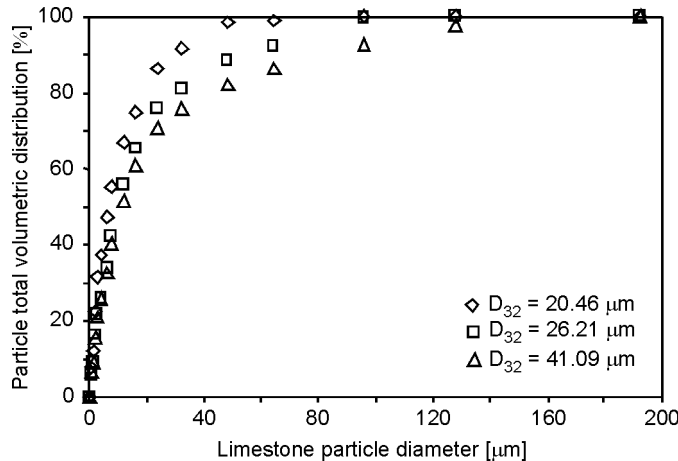


Fig. 2. Grain size distribution of the ground limestone test samples

Test limestone sample of mass m_0 was added to the suspension of the composition corresponding to that in the selected FGD system, then stirred and titrated with sulfuric acid so that the predefined pH value remained constant.

In this way, volumes of acid used per known time intervals (e.g. every minute) could be determined. From these results, time dependence of m/m_0 was calculated, where: m_0 – starting limestone sample mass, m – limestone sample mass after titration time t . This relationship was used to determine the coefficient k (Eq. (3)).

The calculated values of the coefficient k for three limestone samples and several pH values of the suspension are presented in Fig. 3.

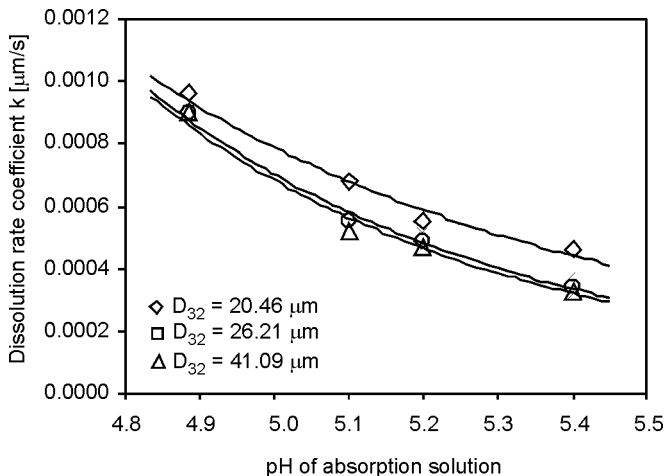


Fig. 3. Dissolution rate coefficient k for selected limestone samples in the absorption suspension in function of pH [6]

The limestone dissolution rate coefficient is higher for lower pH values and higher sorbent grinding degrees (lower D_{32} diameters). The impact of the latter parameter is slightly reduced upon reduction of the pH value of the suspension. Using the model described in [7], Kuciel calculated the tank volumes for the working conditions in selected systems and compared them with the values designed for the system [6]. The values calculated using the proposed formula did not differ from the actual volumes of the tanks by more than 10%.

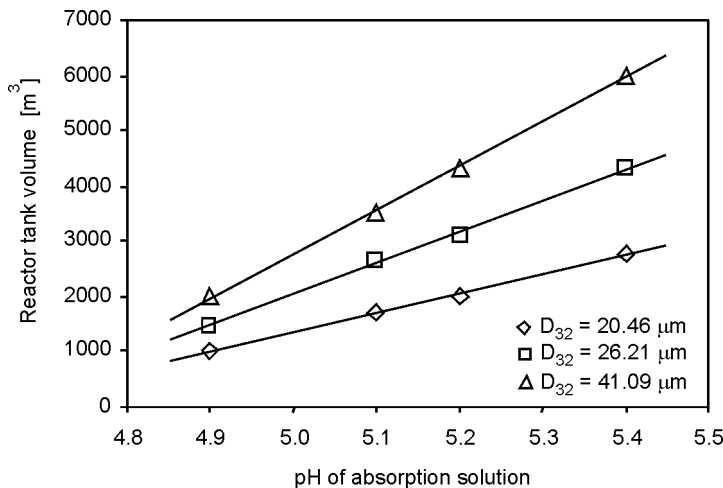


Fig. 4. The effect of pH and the mean limestone grain size on the reaction tank volume [6]

The dependences of the calculated values of the tank volume based on Kuciel results [6] on pH of the absorption suspension and the limestone disintegration degree are presented in Fig. 4. One may have serious objections to the dependence of the tank volume on pH, since an opposite effect is obvious – the higher pH of the suspension, the shorter its required retention time in the tank and the lower the tank volume itself is [8]. Kuciel [6] does not analyse the relationship presented in Fig. 3, suggesting that the dissolution rate of limestone particles increases along with increasing pH value.

5. SIMPLIFIED PROCEDURE OF CALCULATION OF THE TANK VOLUME

The design of systems for flue gas desulfurization in ground limestone suspensions starts with predefining the pH value of the suspension in the reactor tank based on literature data and, in the case of renowned design and installation companies, on the experience gained from installations designed and exploited in the past. The residence time of suspension in the reactor is also predefined based on the experience from pre-

vious installations. This operation is routine-based and does not result from a thorough knowledge of physicochemical properties of the sorbent (reagent), as it remains undefined at this stage; the material mining site or the supplier are not defined; nor are the exact chemical composition, reactivity and grain size distribution of the material.

Before designing of the process is started, one should initiate a simple and relatively inexpensive procedure consisting of samples collection from selected known limestone suppliers so as to avoid design mistakes and the resulting expensive adjustments of the working parameters of the FGD system. The samples should be tested for chemical composition and disintegration degree.

The samples prepared in this way should be tested with the purpose to determine the coefficient k of the limestone particle dissolution rate. To this end, a laboratory vessel (e.g., a flask) should be charged with a suspension prepared beforehand to correspond the intended composition in the FGD tank at nominal working conditions. The suspension in the vessel (flask) should be stirred and charged with a pre-weighed limestone sample of known chemical composition and grain size distribution and stirred again.

Thus prepared suspension is titrated with a sulfuric acid solution to maintain a constant, predefined pH value, e.g. pH = 5.2 (sulfuric acid is dosed so that the pH value of the solution remains constant). The volume of the sulfuric acid introduced to the suspension during titration in a given interval should be carefully monitored for subsequent calculation of the mass of converted limestone over time and the m/m_0 ratio. These data allow for determination of both coefficient k and the m/m_0 ratio in function of time t with the following equation:

$$m = m_0 \left(1 - \frac{kt}{R_0} \right)^3, \quad (4)$$

where: k – coefficient of the dissolution rate of a ground limestone particle, $\mu\text{m}/\text{min}$, m_0 – mass of spherical particles at the beginning of titration, g, m – mass of spherical particles after time t , g, R_0 – radius of a spherical particle of ground limestone, μm , t – time interval between two consecutive doses of sulfuric acid introduced into the flask, min.

The procedure allows determination of the volume of sulfuric acid consumed in known time intervals, e.g. every minute (if pH value of the suspension after that time is at the predefined level). Calculations of k may be carried out for mean diameters of each fraction of particles, and thus Eq. (4) should be applied to m_{0i} , m_i and R_{0i} , where i is the considered fraction of particles, or to the Sauter mean diameter (which simplifies and speeds up the procedure of determining the coefficient k). After determining the value of k and predefining pH of the absorption suspension and the mean particle size ($D_S = D_{32}$) as assumed in the installation design, one may use the simplified method to calculate the absorption suspension reactor tank volume.

Multiple regression analysis of data presented in this paper was performed to model the impact of the most important parameters characterizing the reagent ground limestone (mean diameter of ground limestone particles D_{32} and the coefficient k of limestone dissolution rate) and the absorption suspension (pH). At the confidence level of 95%, the following correlation equation was obtained:

$$V_{zb} = pH^{-3.4455} k^{-1.5416} D_{32}^{0.587}. \quad (5)$$

Statistical regression parameters of the correlation are: multiplicity $R = 0.9999$, $R^2 = 0.9999$; adjusted $R^2 = 0.88882$; standard error $S_e = 0.0691$; observations: 12. Maximum deviations of the designed suspension tank volumes from the calculated values were 9.6 and -11.83%, while mean deviations were 5.14 and -5.44%. The comparison between the designed and the calculated reactor tank volumes is presented in Fig. 5.

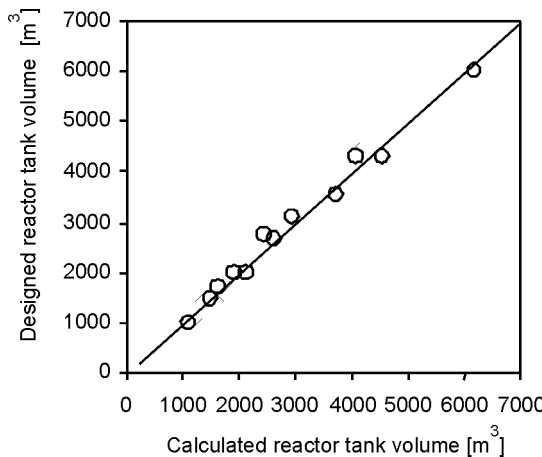


Fig. 5. Designed and calculated FGD system reactor tank volumes

According to Eq. (5), the volume of the reactor tank decreases upon increasing pH of the absorption suspension and sorbent dissolution rate, and increases upon increasing the ground limestone particle diameter. pH of the suspension has the greatest impact on the tank volume.

6. SUMMARY

Experimentally determined dissolution rate coefficients of limestone in the reactor tank, the reagent grinding degrees and pH values of the absorption suspension in three exploited FGD systems [6] were used to establish the correlation equation (5) which can be used to calculate the working tank volume. The equation is characterized by

relatively low deviation of actual reactor tank volumes from the calculated values; the mean deviation is about 5%.

In the case of known values of pH of suspension (either predefined or defined for particular FGD system exploitation conditions), rate of the limestone dissolution in the absorption suspension (characterized by limestone dissolution rate coefficient) and the limestone grinding degree (D_{32}), they may be used to calculate the volume of the reactor tank.

In order Eq. (5) be used in calculations of the suspension tank volumes of an FGD system being designed or already in operation, the limestone grinding degree (characterized by the mean particle diameter D_{32}), the coefficient k of the limestone dissolution rate and pH value of the absorption suspension should be experimentally determined by established chemical analyses as described in appropriate standards.

REFERENCES

- [1] KOCH R., NOWORYTA A., *Mechanical processes in chemical engineering*, WNT, Warszawa, 1992 (in Polish).
- [2] RUMPF H., Chem. Ing. Techn., 1974, 46, 1.
- [3] RUMPF H., *Mechanische Verfahrenstechnik*, Carl Hanser Verlag, München, 1975.
- [4] BURZAŁA B., WOJNAR K., *The issue of chemical analysis of limestone powder and products from FGD*, [In:] Proc. IV Forums: *Operational Experience FGD*, Tatrzańska Łomnica, 22–24 April 2000, 219.
- [5] MOKROŚZ W., Chemik. Nauka – Technika – Rynek, 2005, 58 (6), 301.
- [6] KUCIEL E., Inż. Chem. Proc., 1995, 16, 232.
- [7] LEVENSPIEL O., *The chemical reactor omnibook*, Oregon, 1989, 54.1–54.12.
- [8] GŁOMBA M., J. Air Waste Managem. Assoc. 2010, 60 (8), 1009.

KATARZYNA JUDA-REZLER*, MAGDALENA REIZER*, WOJCIECH TRAPP**

ANALYSIS OF POSSIBLE CLIMATE CHANGE IMPACTS ON AIR POLLUTION BY SULFUR SPECIES OVER CENTRAL-EASTERN EUROPE

High resolution, complex modelling system built with regional climate model (RegCM3), original emission model (EMIL) and air quality model CAMx was employed for analysing projected climate change impacts on concentrations and depositions of sulfur compounds (SO_x) over Central and Eastern Europe. With employment of constant emission rates, results show a slight increase of SO_2 concentrations in the future, as well as increase of SO_x deposition in the mountains and decrease in central and eastern parts of Poland. Projections indicate also slight changes in a number of days and hours during the calendar year with SO_2 levels exceeding European limit values. The biggest changes are evident in the vicinity of large point emission sources.

1. INTRODUCTION

Climate change and air pollution are mutually connected. Since 2007, it is very likely (with probability higher than 90%) that *most of the observed increase in globally averaged temperatures since the mid-20th century is due to the observed increase in anthropogenic greenhouse gases (GHGs) concentrations* [1]. On the other hand, climate change may affect exposures to air pollutants by many ways [2] such as affecting weather and thereby local and regional pollution concentrations (a), affecting anthropogenic emissions, including adaptive responses involving increased fuel combustion for fossil fuel fired power generation (b), affecting natural sources of air pollutant emissions (c), and changing the distribution and types of airborne allergens (d). Local weather patterns influence atmospheric chemical reactions as well as atmospheric transport and deposition processes. In addition, the chemical composition of the atmosphere may in turn have a feedback effect on the local climate. Weather is also

*Warsaw University of Technology, Faculty of Environmental Engineering, ul. Nowowiejska 20, 00-653 Warsaw, Poland. Corresponding author M. Reizer, e-mail: magdalena.reizer@is.pw.edu.pl

**Ekometria Sp. z o.o., Orfeusza 2, 80-299 Gdańsk, Poland.

associated with energy demands (e.g. for space heating and cooling) that could alter patterns of fossil fuel combustion. In particular, individual responses to extremely hot/extremely cold weather can result in large increases in air conditioner use/fossil fuel use for heating purposes.

According to the latest Intergovernmental Panel of Climate Change (IPCC) Assessment Report [1], warming of the climate system is unequivocal, as is now evident from observations of increases in global average air and ocean temperatures, widespread melting of snow and ice, and rising global mean sea level.

Research in the last years has led to a substantial improvement of our understanding of the physicochemical behaviour of the atmospheric and climate systems, as well as impacts to human health and ecosystems. Moreover, a large amount of information has been collected, and modern tools developed, that may be applied to assess both the air quality at regional and local scales, as well as global and regional climate changes. General circulation models (GCMs), also referred to as global climate models are used to simulate long term changes of climate as a result of slow changes in some boundary conditions or anthropogenically driven changes such as the GHGs concentrations. To simulate climate changes in a statistical sense (i.e., the means and variability), GCM's are run for longer periods (years, decades). Most climate models are large dynamical deterministic systems involving a million variables on huge computers. They can reproduce reasonably well climate features on large scales (global and continental) but their accuracy decreases when proceeding from continental to regional and local scales because of the lack of resolution. However, in many applications, particularly related to the assessment of climate change impacts, the information on surface climate change at regional to local scale is fundamental. For this end, during the last decade, regional climate models (RCM) have been increasingly used to examine climate variations at scales that are not resolved by global models (e.g. [3–5]). To the extent that they produce realistic climate simulations, such models can be powerful tools in the studies of regional climate impacts. RCM are usually working with fine spatial resolution of 10–60 km.

For studying climate change impacts on air quality, the modelling systems coupling GCM/RCM with complex air quality models (AQM) are being used. The most widely AQM used in such coupled systems are, in present, the so-called third generation photochemical Eulerian grid models, namely CAMx (comprehensive air quality model with extensions) and CMAQ (community multiscale air quality) models. The comparison of these models is given in [6].

Most of the studies that have attempted to quantify the potential effects of climate change on air quality examined the impact of increased temperature on global O₃ formation [7, 8]. In general, these studies find that O₃ concentrations increase as temperatures rise, although the estimated magnitude of the effect varies considerably. However only few studies deal with regional and local scale [9–11].

The aim of this study is to apply coupled RCM-AQM modelling system to model the interaction between climate and air quality by projections of present and future air

pollution levels and loads in the target regions on Central-Eastern Europe. Sulphur species having multifaceted impacts on human health, ecosystems and radiation budget of the atmosphere are chosen as key species.

2. METHODS

2.1. DESCRIPTION OF THE MODELLING SYSTEM

Modern modelling system, based on regional climate model, RegCM3, the original emission model, EMIL, and air quality model CAMx were applied for assessing air pollution in present and future climates. The system was implemented for high resolution ($10\text{ km} \times 10\text{ km}$) modelling domain, centred over Poland ($52.00^{\circ}\text{N}, 19.30^{\circ}\text{E}$) on a grid with 120×109 points. The map projection choice was Lambert conformal. The modelling domain, called hereafter WUT (Warsaw University of Technology) domain, is presented in Fig. 1. The implementation of the modelling system was carried out within the 6. European Union Framework Programme CECILIA (Central and Eastern Europe Climate Change Impact and Vulnerability Assessment).

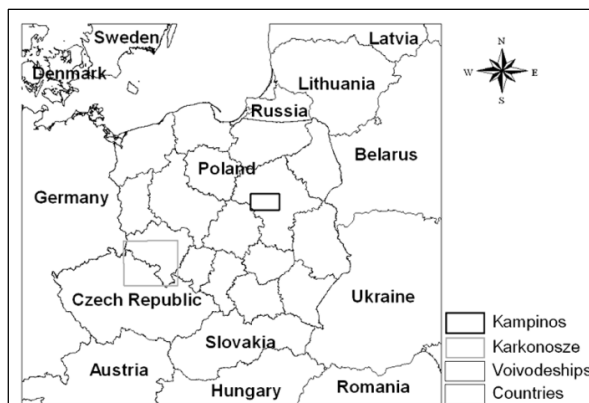


Fig. 1. WUT modelling domain with areas chosen for assessment of climate change impacts on forest ecosystems

CAMx is a photochemical third generation Eulerian grid model developed at ENVIRON International Corporation (Novato, California) [12]. Simulations have been carried out using CAMx v.4.40. The chemistry mechanism invoked was Carbon Bond, version 4 [13], including 117 reactions – 11 of which are photolytic – and up to 67 species (37 state gases, up to 18 state particulates and 12 radicals). The domain vertical profile contained 12 layers of varying thicknesses, extending up to 450 hPa. Boundary conditions for air quality simulations were calculated with $50\text{ km} \times 50\text{ km}$

resolution for the European domain at BOKU (Universität für Bodenkultur, Vienna, Austria) under CECILIA project [14].

Regional climate model RegCM3 is a three dimensional hydrostatic model that allows to simulate the climate over a given area. The model was developed at ICTP (The Abdus Salam International Centre for Theoretical Physics) in Trieste. The dynamical core is based on the hydrostatic version of the NCAR-PSU Mesoscale Model version 5 (MM5) [15]. In present study, for 10 km x 10 km resolution simulations, the improved version of RegCM3 for high resolution use, RegCM3-Beta [5], was used. The domain's vertical profile contained 18 layers of varying thickness, extending up to 50 hPa.

Not all meteorological fields from the RegCM3-Beta may constitute direct input to CAMx model. Therefore, pre-processor which prepares the required input fields was developed at Charles University in Prague under CECILIA project. In pre-processor *on-line* emissions of biogenic hydrocarbons (isoprene, monoterpenes) were also calculated as a function of meteorological parameters (temperature and radiation) and the available land use categories, following Guenther et al. [16].

An important part of the study was development of a detailed anthropogenic emission and emission parameters database for Poland. For this purpose, an original emission model EMIL (EMIssion model) was developed. The created database of large combustion plants (LCP) with a stack height that is equal or above 100 m ($h \geq 100$ m) for reference year 2000 consists of the following information: name of the LCP, number of stack, geographical coordinates, installed technological units, stack height and diameter, temperature of exhaust gases, velocity of exhaust gases as well as amount of emission of SO₂, NO₂ and PM₁₀. LCP sources were simulated in CAMx model individually. For area, mobile and point sources with the stack height below 100 m ($h < 100$ m), the model generates emissions for each cell of computational grid (10 km × 10 km). This is based on a detailed emission sources inventory composed for reference year 2000 in 1 km × 1 km resolution, meteorological data and terrain characteristics. Data on population density, sector-specific activity, fuel demands and characteristics, and sector-dependent Polish specific emission factors were collected. For temporal distribution of emissions, the EMIL model applies sector-specific monthly, daily and hourly emission factors.

For other countries belonging to the modelling domain anthropogenic emission database was prepared at BOKU, based on EMEP inventory (see [14] for details). For the Pannonian countries, a detailed, high resolution, emissions inventory was used. All these emissions were treated as area sources in CAMx simulations.

For the purpose of evaluation of the modelling system, simulations for 2000 year were carried out with regional climate model driven by the ERA40 reanalysis [17]. Then, high resolution simulations were completed for three decadal time slices: 1991–2000 (control decade), 2041–2050 (the so-called near future climate, DEK2) and 2091–2100 (the so-called far future climate, DEK3). RegCM3-Beta was driven by the ECHAM5 GCM under forcing from the SRES A1B IPCC greenhouse gas emission sce-

nario [18]. Global climate model simulations with $25 \text{ km} \times 25 \text{ km}$ resolution as boundary conditions for regional climate simulations were performed at ICTP under CECILIA project. To insolate climate change impacts on air quality, the anthropogenic emission were kept constant at the values of year 2000 for all simulated time slices.

2.2. SELECTED FOREST ECOSYSTEMS

In order to assess climate change impacts on selected forest ecosystems in Poland, two areas with a high afforestation rate were selected: Karkonosze domain covering Karkonosze National Park, and Góry Stołowe National Park as well as Kampinos domain covering Kampinoski National Park. Both areas are different in terms of geographical localization and climatic conditions. The WUT modelling domain with localization of selected forested areas is presented in Fig. 1.

2.3. AIR QUALITY STANDARDS AND THEIR EXCEEDANCES

Based on WHO guidelines, standards for ambient air pollutants were set in the framework of EU legislation. The latest EU Directive 2008/50/EC states the following standards:

- Limit value (LV) means a level fixed based on scientific knowledge, with the aim of avoiding, preventing or reducing harmful effects on human health and/or the environment as a whole, to be attained within a given period and not to be exceeded once attained.
- Critical level (CLev) means a level fixed based on scientific knowledge, above which direct adverse effects may occur on some receptors, such as trees, other plants or natural ecosystems but not on humans.

By subtracting the limit values/critical levels from the existing concentrations, the so called exceedances are obtained, which are direct estimates of population and/or environmental risk. Exceedance of CLev/LV is defined as a non-negative difference between CLev/LV and the concentration (C); $\text{Ex}(\text{CLev}_t) = \max\{C_t - \text{CLev}_t, 0\}$; $\text{Ex}(\text{LV}_t) = \max\{C_t - \text{LV}_t, 0\}$, where t is the averaging time for concentration, $t = 1 \text{ h}, 8 \text{ h}, 24 \text{ h}, 1 \text{ year}$. The EU Directive 2008/50/EC sets two legally binding SO_2 limit values for the protection of human health: $125 \mu\text{g}/\text{m}^3$ for daily mean SO_2 levels and $350 \mu\text{g}/\text{m}^3$ for hourly mean SO_2 levels not to be exceeded on more than 3 and 24 times per calendar year, respectively. The SO_2 critical level for the protection of vegetation was set at the level of $20 \mu\text{g}/\text{m}^3$ for both calendar year and winter season (from 1 October to 31 March).

3. RESULTS

3.1. EVALUATION OF THE MODELLING SYSTEM

Evaluation of the modelling system was carried out for 2000 year with RegCM3-Beta driven by reanalysis ERA40 meteorological fields. Annual mean SO_2 concentra-

tions were evaluated using observations from EMEP (<http://www.emep.int>) and EIONET-Airbase (<http://air-climate.eionet.europa.eu>) databases. For evaluation, data from 93 stations, including 5 stations located in Poland, were used. Results indicate a satisfactory performance of the modelling system. The following evaluation measures have been obtained: the correlation coefficient between predicted values and observations $r = 0.67$, Willmott's index of agreement IA = 0.76, root mean square error RMSE = $2.71 \mu\text{g}/\text{m}^3$, normalized mean square error NMSE = 0.45. Finally, FAC2, a fraction of predictions within the factor 2 of observations, was determined as a widely used measure of agreement between model results and observations. For WUT domain, 75% of observation–model pairs lie inside the factor 2 agreement area.

3.2. IMPACTS OF CLIMATE CHANGES ON SO₂ LEVELS

Figure 2a shows the distribution of calculated annual mean levels of SO₂ for the control period, while differences between pollutant levels for control and for DEK3 periods are given in Fig. 2b.

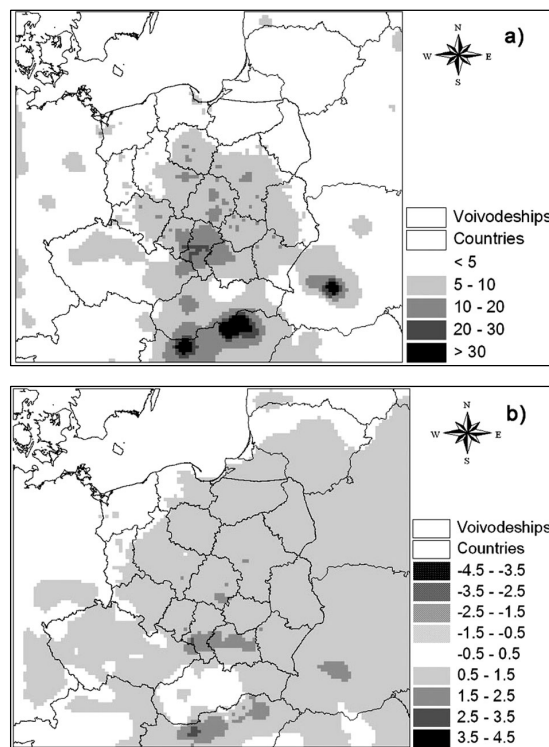


Fig. 2. Annual mean SO₂ concentrations [$\mu\text{g}/\text{m}^3$] in the control period 1991–2000 (a), and climate change impacts on SO₂ concentrations in terms of the differences [$\mu\text{g}/\text{m}^3$] for DEK3 (2091–2100) against the control period (b)

For the control period, high SO₂ annual mean levels (up to 30 µg/m³) were obtained for Upper Silesia region in Poland as well as for Hungary and Ukraine, where the levels are the highest and exceed 30 µg/m³. The high SO₂ concentrations calculated for Hungary and Ukraine are due to the treatment of LCP sources as area sources in these countries. In future, higher SO₂ concentrations (up to 3.5 µg/m³) are predicted. The highest increase of SO₂ levels is expected for Upper Silesia region in Poland as well as for Northern Hungary.

3.3. IMPACTS OF CLIMATE CHANGES ON EXCEEDANCES OF SO₂ LIMIT VALUES FOR THE PROTECTION OF HUMAN HEALTH

Number of days with daily mean SO₂ levels exceeding 125 µg/m³ calculated for the control decade and differences in number of exceedance days between DEK3 and control decade are presented in Fig. 3.

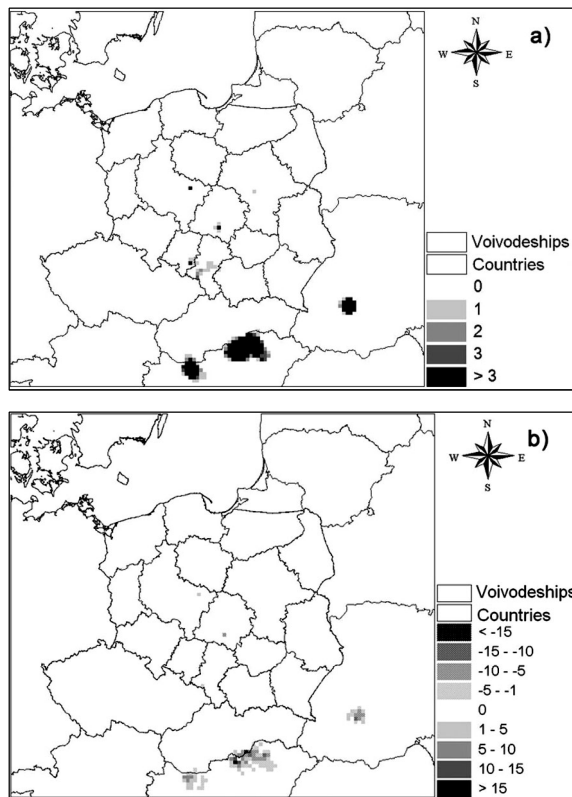


Fig. 3. Number of exceedances [days] over SO₂ daily limit value of 125 µg/m³ for control decade 1991–2000 (a) and climate change impacts on SO₂ limit value exceedances in terms of the differences [days] for DEK3 (2091–2100) against the control period (b)

On the majority of the WUT domain, no exceedances of the daily LV exist for SO₂ in 1991–2000 period (no days with daily mean concentration exceeding 125 µg/m³). The exceedances occur in the surroundings of large combustion plants where the limit value is not met (number of days with daily mean levels over 125 µg/m³ is higher than 3). The maximum number of days with average concentration exceeding 125 µg/m³ equals to 95 and was calculated for Northern Hungary. For 2091–2100 period there are also no exceedances of the daily LV for SO₂ on the majority of the WUT domain. Only in the surroundings of LCP the number of exceedance days slightly decreases in Poland as well in direct vicinity of LCP and increases in further vicinity of LCP in Hungary and Ukraine. The highest differences were calculated for the vicinity of Mátra Power Plant in Hungary (from –18 to 17 exceedance days).

Number of hours with hourly mean SO₂ levels exceeding 350 µg/m³ calculated for the control decade and differences in number of exceedance hours between DEK3 and the control decade are presented in Fig. 4.

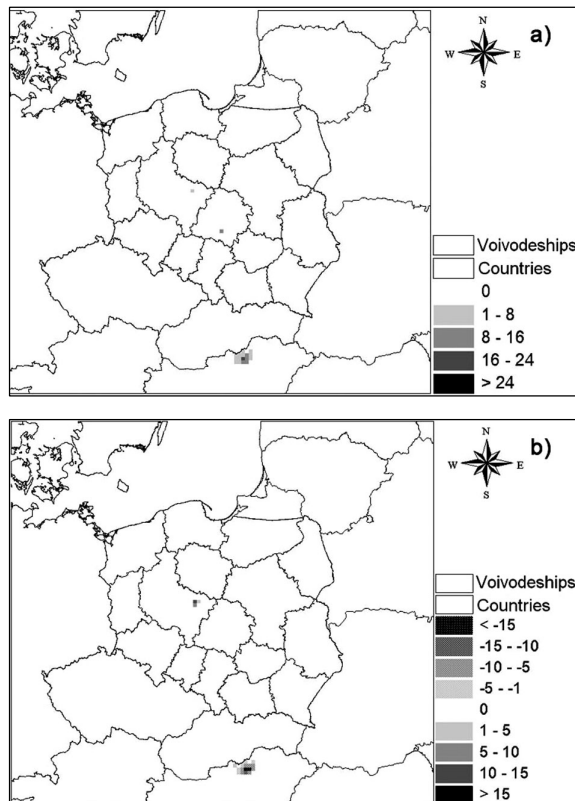


Fig. 4. Number of exceedances [h] over SO₂ hourly limit value of 350 µg/m³ for control decade 1991–2000 (a) and climate change impacts on SO₂ limit value exceedances in terms of the differences [h] for DEK3 (2091–2100) against the control period (b)

On the majority of the WUT domain, no exceedances of the hourly LV occur for SO₂ in the control period. The exceedances occur in the surroundings of LCP in Hungary and in Poland, however the number of hours with levels over 350 µg/m³ is not higher than 24, thus the LV is met. For 2091–2100 period also no exceedances of the hourly LV for SO₂ occur on the majority of the WUT domain. The climate impact is seen only in few grid points – increase (up to 14 h) in Poland and decrease in the vicinity of Mátra Power Plant in Hungary.

3.4. IMPACTS OF CLIMATE CHANGES ON EXCEEDANCES OF SO₂ CRITICAL LEVEL FOR THE PROTECTION OF VEGETATION

Exceedances of SO₂ annual critical levels of 20 µg/m³ calculated in the control period and DEK3 are shown in Figs. 5a, b, respectively.

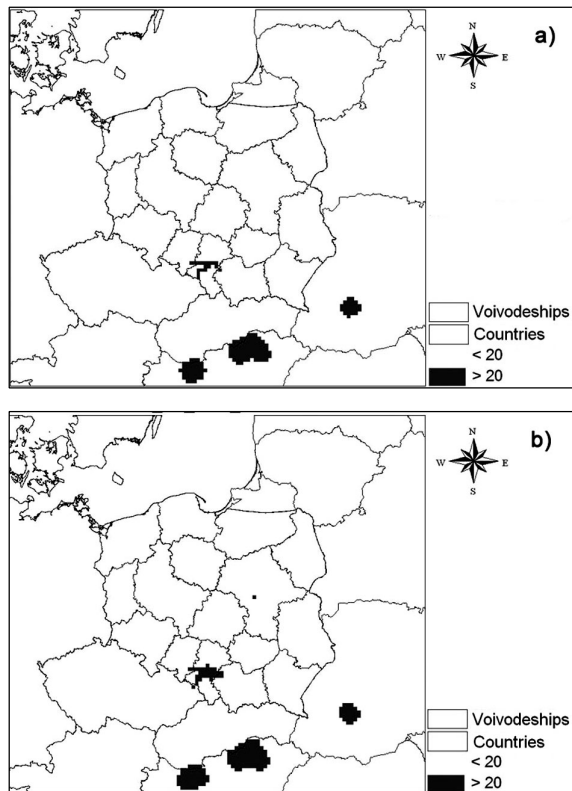


Fig. 5. Exceedances [µg/m³] of SO₂ annual critical level for the protection of vegetation in the control period 1991–2000 (a) and for DEK3 2091–2100 (b)

In 1991–2000, the annual SO_2 critical level of $20 \mu\text{g}/\text{m}^3$ is exceeded only in Upper Silesia industrial region in Poland and for vicinity of LCP in Northern Hungary and Ukraine (maximum value equals to $51 \mu\text{g}/\text{m}^3$). For far future 2091–2100 period, there is no significant change in the areas and size of exceedances. It can be noticed that exceedances area in Upper Silesia is slightly wider for the end-century decade in comparison to the control period.

3.5. IMPACTS OF CLIMATE CHANGES ON SO_x DEPOSITION OVER SELECTED FOREST ECOSYSTEMS

Deposition of oxidized sulfur (SO_x), which is the sum of SO_2 and sulfates, SO_4^{2-} , was calculated with RegCM3-Beta/EMIL/CAMx modelling system for each grid cell of selected forest areas. Total deposition of sulfur was calculated as the sum of wet and dry deposition. The relevant computational procedures for obtaining a time and space variable dry and wet deposition are included in the CAMx model [12]. Then, trend analysis of the total deposition of SO_x in the whole 1991–2100 period was performed, based on annual mean deposition calculated for each domain. A linear continuity between analysed periods was assumed.

In a similar way, trend analysis of air temperatures (2 m) and precipitation amounts calculated for 1961–2000, 2021–2050 and 2071–2100 time slices, was conducted (simulations performed by RegCM at CUNI). Concerning precipitation simulation, this is the most difficult task in climate modelling. Nowadays all climate models overestimate precipitation amounts and thus their results cannot be used directly. Consequently, model results are corrected with observations. In the present study, precipitation values were corrected with observations from the Climate Research Unit CRU TS 1.2 [19] database. Figure 6 shows estimated temperature and precipitation values for the whole 1991–2100 period for both selected domains.

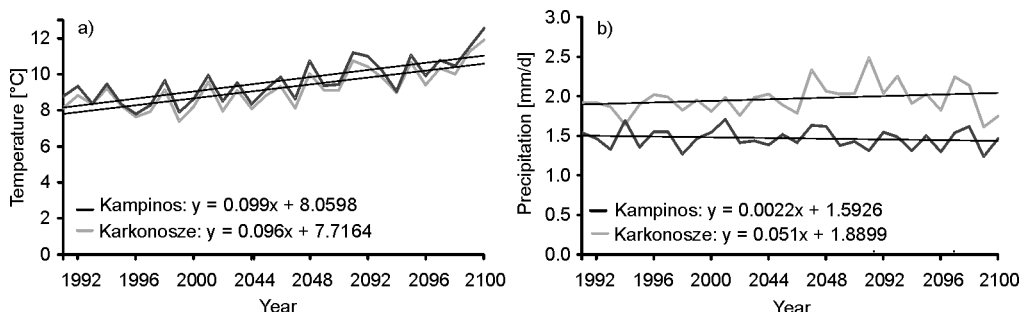


Fig. 6. Projected trend of temperature (a) and precipitation (b) changes for 1991–2100 period for Kampinos and Karkonosze domains

In the 1991–2100 period, increase in temperature is clear and amounts to 2.8 °C for both selected domains. In the same time, precipitation increases by 0.3 mm/day in Karkonosze domain and slightly decreases by 0.05 mm/day in Kampinos domain. Estimated total deposition of oxidized sulfur in the whole 1991–2100 period for both selected domains is presented in Fig. 7.

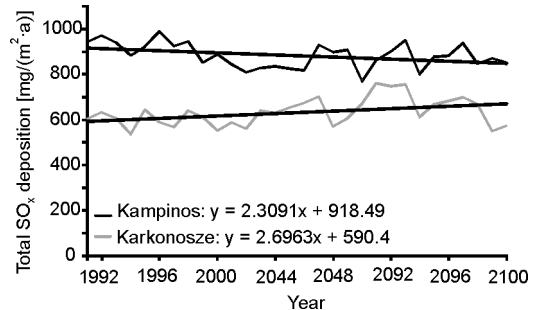


Fig. 7. Projected trend of total deposition of SO_x [mg S/m²] in the 1991–2100 period for Kampinos and Karkonosze domains

For the whole considered period decreasing and increasing trend in total sulfur deposition is projected for Kampinos and Karkonosze domains, respectively. The increase in total sulfur deposition for Karkonosze domain equals to 80 mg S/(m²·year), while the decrease for Kampinos domain equals to 70 mg S/(m²·year).

4. DISCUSSION AND CONCLUSIONS

High resolution simulations of climate change impacts on SO₂ concentrations and SO_x depositions over Central-Eastern Europe were performed. A complex RegCM3-Beta/EMIL/CAMx modelling system was employed for calculations. It turned out to be a useful research tool. The obtained results of SO₂ concentrations in 2000 year reproduce, with satisfactory accuracy, observations from 93 air monitoring stations. Comparison of SO₂ concentrations obtained for the vicinity of LCP sources over Poland and over Ukraine and Hungary indicates better model performance for Poland. This is due to the individual treatment of LCP sources in Poland and employment of LCP parameters for simulation of the subgrid scale rise and spread of the plume. The LCP sources in Hungary and Ukraine were treated as surface area sources. These resulted in significant overestimation of SO₂ concentrations in the vicinity of these sources.

The results of simulations indicate a slight impact of climate change on SO₂ concentrations. Between 2091–2100 and control period a slight increase (up to 2.5–3.5 µg/m³) was observed in average SO₂ levels over Central-Eastern Europe. Also exceedances of daily and hourly air quality standards have very similar values and spatial distribution. The biggest changes are visible in the vicinity of LCP sources. In all simulations, the emissions were kept constant and air quality was dependent only on the projected

changes in climate parameters. The results show that SO₂, as the primary pollutant, slightly subjects to these changes, under assumed A1B IPCC scenario.

In opposite, the impact of climate changes on SO_x deposition is clearly evident. Trend analysis indicates a decrease in total deposition of sulfur in Kampinos domain equal to 70 mg S/(m²·year) and increase in Karkonosze domain equal to 80 mg S/(m²·year). At the same time, for both domains air temperature increases, while precipitation increases in Karkonosze domain and in Kampinos domain trend line shows no change. The sulfur deposition increase in Kampinos domain is probably due to both an increase in wet deposition (precipitation increase) and in dry deposition. Climate model results (not shown in this study) show increase of average annual wind speed in the future climate for both areas. For Karkonosze domain, it is probably the reason of increase of dry deposition, characteristic of mountains and foothill areas. On the other hand, decrease of sulfur deposition in Kampinos domain is probably associated with the location of the domain in the vicinity of Warsaw agglomeration with large point sources of SO₂. At higher wind speeds, plume of pollutants from these sources is transported faster over longer distances, resulting in reduction of dry deposition in the analysed domain.

Because many factors affect air quality, the results of this study should not be considered as predictions of future air quality associated with climate change. Rather, they demonstrate the sensitivity of atmospheric air pollutants to changes in specific meteorological variables.

The research presented in this study will be continued. The distribution of NO₂ concentrations and NO_x deposition, critical loads of sulfur and nutrient nitrogen for selected areas as well as exceedances of critical loads will be examined.

ACKNOWLEDGEMENTS

This work was supported by the Central and Eastern Europe Climate Change Impact and Vulnerability Assessment Project (CECILIA), financed by EU 6. FP Contract GOCE 037005 to Warsaw University of Technology. The calculations were partly carried out in the Academic Computer Center in Gdańsk, Poland on a cluster supercomputer GALERA. The authors wish to thank Dr. Michal Belda from Charles University (Czech Republic) for providing RegCM3 results for selected domains, Dr. Erica Coppola from ICTP (Italy) for providing climatic boundary conditions, Dr. Bernd C. Krüger from BOKU (Austria) for providing chemical boundary conditions and Dr. Zoltan Barcza from Eotvos Lorand University (Hungary) for inspiring discussions.

REFERENCES

- [1] IPCC, *Fourth Assessment Climate Change 2007: Impacts, Adaptation and Vulnerability*, Assessment Report from Working Group II, Intergovernmental Panel on Climate Change, Brussels, 2007.
- [2] BERNARD S.M., SAMET J.M., GRAMBSCH A., EBI K.L., ROMIEU I., Environ. Health Perspect., 2001, 109 (2), 199.
- [3] BUBNOVA R., HELLO G., BÉNARD P., GELEYN J.-F., Mon. Weather Rev., 1995, 123(2), 515.

- [4] GIORGI F., PAL J.S., BI X., SLOAN L., ELGUINDI N., SOLMON F., *Theor. Appl. Climatol.*, 2006, 86, 1.
- [5] PAL J.S., GIORGI F., BI X., ELGUINDI N., SOLMON F., GAO X., RAUSCHER S.A., FRANCISCO R., ZAKY A., WINTER J., ASHFAQ M., SYED F.S., BELL J.L., DIFFENBAUGH N.S., KARMACHARYA J., KONARÉ A., MARTINEZ D., DA ROCHA R.P., SLOAN L.C., STEINER A.L., *Bull. Am. Meteorol. Soc.*, 2007, 88 (9), 1395.
- [6] TESCHE T.W., MORRIS R., TONNESEN G., McNALLY D., BOYLAN J., BREWER P., *Atmos. Environ.*, 2006, 40 (26), 4906.
- [7] STEVENSON D.S., DENTENER F.J., SCHULTZ M.G., ELLINGSEN K., VAN NOIJE T.P.C., WILD O., ZENG G., AMANN M., ATHERTON C.S., BELL N., BERGMANN D.J., BEY I., BUTLER T., COFALA J., COLLINS W.J., DERWENT R.G., DOHERTY R.M., DREVET J., ESKES H.J., FIORE A., GAUSS M.A., HAUGLUSTAINE D.A., HOROWITZ L.W., ISAKSEN I.S.A., KROL M.C., LAMARQUE J.F., LAWRENCE M.G., MONTANERO V., MÜLLER J.F., PITARI G., PRATHER M.J., PYLE J.A., RAST S., RODRIGUEZ J.M., SANDERSON M.G., SAVAGE N.H., SHINDELL D.T., STRAHAN S.E., SUDO K., SZOPA S., *J. Geophys. Res.*, 2006, 111, D08301, doi:10.1029/2005JD006338.
- [8] RACHERLA P.N., ADAMS P.J., *Atmos. Chem. Phys.*, 2008, 8 (4), 871.
- [9] SZOPA S., HAUGLUSTAINE D.A., VAUTARD R., MENUT L., *Geophys. Res. Lett.*, 2006, 33, L18805, doi: 10.1029/2006GL25860.
- [10] MELEUX F., SOLMON F., GIORGI F., *Atmos. Environ.*, 2007, 41, 7577.
- [11] NOLTE C.G., GILLILAND A.B., HOGREFE C., MICKLEY L.J., *J. Geophys. Res.*, 2008, 113, D14307, doi:10.1029/2007JD008497.
- [12] ENVIRON, *User's Guide to the Comprehensive Air Quality Model with Extensions (CAMx), Version 4.40*, ENVIRON International Corporation, Novato, California, 2006.
- [13] GERY M.W., WHITTEN G.Z., KILLUS J.P., DODGE M.C., *J. Geophys. Res.*, 1989, 94, 12925.
- [14] KRÜGER B.C., KATRAGKOU E., TEGOULIAS I., ZANIS P., MELAS D., COPPOLA E., RAUSCHER S., HUSZAR P., HALENKA T., Q. J. Hung. Meteorol. Serv., 2008, 112 (3–4), 285.
- [15] GRELL G.A., DUDHIA J., STAUER D.R.: *A description of the fifth-generation Penn State/NCAR mesoscale model (MM5)*, National Center for Atmospheric Research, Boulder, Colorado, 1994.
- [16] GUENTHER A.B., ZIMMERMANN P.C., HARLEY R., MONSON R.K., FALL R., *J. Geophys. Res.*, 1993, 98, 12609.
- [17] UPPALA S.M., KÅLLBERG P.W., SIMMONS A.J., ANDRAE U., BECHTOLD V.D.C., FIORINO M., GIBSON J.K., HASELER J., HERNANDEZ A., KELLY G.A., LI X., ONOGI K., SAARINEN S., SOKKA N., ALLAN R.P., ANDERSSON E., ARPE K., BALMASEDA M.A., BELJAARS A.C.M., BERG L.V.D., BIDLOT J., BORMANN N., CAIRES S., CHEVALLIER F., DETHOF A., DRAGOSAVAC M., FISHER M., FUENTES M., HAGEMANN S., HÖLM E., HOSKINS B.J., ISAKSEN L., JANSEN P.A.E.M., JENNE R., MCNALLY A.P., MAHFOUT J.-F., MORCRETTE J.-J., RAYNER N.A., SAUNDERS R.W., SIMON P., STERL A., TRENBERTH K.E., UNTCH A., VASILJEVIC D., VITERBO P., WOOLLEN J., Q. J. R. Meteorol. Soc., 2005, 131 (612), 2961.
- [18] NAKICENOVIC N., ALCAMO J., DAVIS G., DE VRIES H.J.M., FENHANN J., GAFFIN S., GREGORY K., GRUBLER A., JUNG T.Y., KRAM T., LA ROVERE E.L., MICHAELIS L., MORI S., MORITA T., PAPPER W., PITCHER H., PRICE L., RIAHI K., ROEHL A., ROGNER H-H., SANKOVSKI A., SCHLESINGER M., SHUKLA P., SMITH S., SWART R., VAN ROOIJEN S., VICTOR N., DADI Z., Special Report on Emission Scenarios, Cambridge University Press, Cambridge, 2000.
- [19] NEW M., LISTER D., HULME M., MAKIN I., *Clim. Res.*, 2002, 21 (1), 1.

MICHAL BRANC*, JIŘÍ HORÁK*, TADEÁŠ OCHODEK*

FINE PARTICLE EMISSIONS FROM COMBUSTION OF WOOD AND LIGNITE IN SMALL FURNACES

Assessment of household combustion emission was carried out based on data on meteorological conditions in heating season (outdoor temperature) and the emission factors. Available emission factors, both for various fuels and for various combustion devices differ markedly. The results of experimental determination of particle matter emissions, including dividing total suspended particulate matter into various fractions (PM_{10} and $PM_{2.5}$) have been presented in the paper. Various combustion devices to burn wood and lignite were used in experiments. Samples were taken in a dilution tunnel with the help of an impactor. It was found that specific emissions differ significantly during the combustion cycle. Compared to the used emission factors, differences are evident. It was found that TSP specific emissions depend mainly on the type of construction not its age.

1. INTRODUCTION

Ambient particle matter belongs to significant pollutants threatening human health due to its size spectrum and chemical composition. The size of particles determines the respiratory tract deposition; particles exceeding 10 μm in size are captured in the upper respiratory tract (nose, nasopharynx, mouth). Smaller particles (PM_{10}) are called a thoracic fraction; they are farther separated in the lower respiratory tract (larynx, bronchia etc.) and a wider spectrum of particles penetrates into human lungs (predominantly particles smaller than 2.5 μm ($PM_{2.5}$) [1]). Chemical composition determines toxic influence of particles deposited on organism.

Assessment of household combustion emission in the Czech Republic is carried out based on meteorological conditions in heating season (subsequent determination of fuel consumption) and the emission factors. For lignite combustion, the emission factor is defined by the relation $1 \times A'$ in kg/t, where A' is ash content in fuel (in %). Apportionment of PM_{10} and $PM_{2.5}$ in the total particle matter amount has been determined

*VŠB – Technical University of Ostrava, Energy Research Center, Innovation for Efficiency and Environment, 17. Listopadu 15/2172, 708 33 Ostrava-Poruba, Corresponding author J. Horák, e-mail: jirka.horak@vsb.cz

so far based on results of measurement performed in Poland [2] (PM_{10} proportion in total suspended particulate matter (TSP) is 75%, $\text{PM}_{2.5}$ – 25%). For wood combustion, the emission factor is expressed independently as ash content and it is 5.2 kg/t. Proportion of PM_{10} fraction is determined to 95% and $\text{PM}_{2.5}$ proportion to 90% of TSP. The emission factor is applied regardless to age and composition of heating devices which results in a considerable inaccuracy when assessing emissions in this category of furnaces.

Table 1

Overview of emission factors

Emission factor source	Device category	Coal		Wood			
		Emission factor [g/GJ]					
		TSP	PM_{10}	$\text{PM}_{2.5}$	TSP	PM_{10}	$\text{PM}_{2.5}$
GAINS ^a	boilers, output <50kW	350	315	280	250	240	233
	boilers, output <50kW, new	210	189	268	210	189	268
	stoves	600	540	480	750	672	651
	stoves adapted	420	378	336	259	249	241
	stoves new	300	270	240	140	134	130
	fireplaces	–	–	–	750	720	698
EIG	simplified calculation	household heating devices output <50 kW	444	404	398	730	695
	detailed calculation	fireplaces, open	350	330	330	900	860
		stoves	500	450	450	850	810
		stoves, modern	250	240	220	250	240
		boilers, output <50kW	400	380	360	500	475
		boilers, output <50kW, automatic	80	76	72	70	66
		pellet stoves	–	–	–	80	76
CEPMEIP	household heating devices	350	140	70	–	–	–
	household heating devices, low emission	–	–	–	150	143	135
	household heating devices, high emission	–	–	–	300	285	270
EF used in CR ^b	Household heating devices, output <50 kW	387	290	97	356	338	320

^a<http://gains.iiasa.ac.at/gains/EUR/index.login?logout=1>^bFor fuel with considered parameters: wood – lower heating value 14.6 MJ/kg, lignite – lower heating value 18.1 MJ/kg, lignite – ash content 7%.

Other three sets of emission factors (hereinafter EF) are applied in EU for determination of household solid fuel combustion emissions. These are EFs used in the GAINS emission model (developed by IIASA international research organization, used for projection of greenhouse gas and basic pollutant emissions in Europe) as well

as EFs published by the European Environment Agency in the Emission Inventory Guidebook (EIG) [3] and an EF set prepared within the framework of the project *The Co-ordinated European Programme on Particle Matter Emission Inventories, Projections and Guidance* (CEPMEIP) [4]. All of the mentioned EFs were determined by reputable agencies and it is not possible to say which of them are more representative.

The Czech EF is converted for average values of lignite and wood used for household heating and it is shown in Table 1 together with the above mentioned EFs.

2. EXPERIMENTAL

Used combustion devices and fuel. TSP experimental determination was performed on 6 combustion devices representing fundamental concepts such devices used in Czech Republic for heating requirements. These are automatic boilers, over-fire boilers, under-fire boilers, gasification boilers and fireplace stoves (Fig. 1).

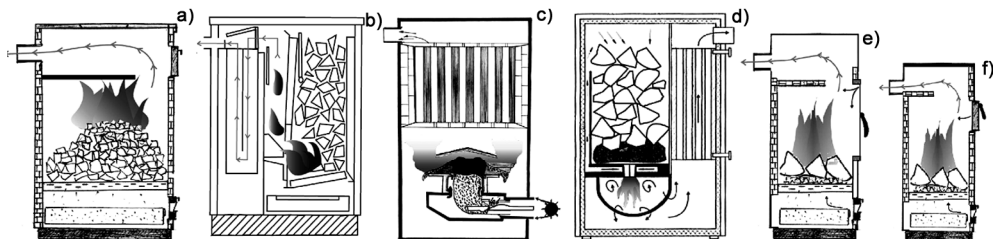


Fig. 1. Schemes of the over-fire (a), under-fire (b), automatic (c) and gasification (d) boilers, the fireplace stove (e) and classic stove (f)

An over-fire boiler is a hand fired device. Fuel batch is fire-penetrated all at once, whereas flue gas goes through the whole fuel bed. Flue way is formed by a single pass. An under-fire boiler represents a hand fired device. Fuel burning from the bottom is replenished with fuel which gradually slides down into the hearth from a reservoir. Flue gas does not pass through the stoked fuel bed. Flue way is formed by three passes. A gasification boiler represents a hand fired device of a modern design with two-phase combustion. In the first phase, fuel is gasified and in the second one, gas burns in a separate combustion chamber. Flue way is formed by "one-and-half pass". An automatic boiler represents a modern design device. Fuel is stoked automatically into a burner with the help of a screw conveyer and it burns subsequently in the under-fire way. Flue way is formed by a single pass only, though, the boiler is fitted with a deflector to capture particles. The conception of the used fireplace and classic stoves makes use of the over-fire combustion system therefore the conception corresponds to the over-fire boiler. During the tests, lignite and wood of parameters presented in Table 2 were used. In the table, w_f' is the total water in raw fuel, percentages of ash (A), carbon (C), hydrogen (H), nitrogen (N), oxygen (O),

and sulfur (S) refer to dry ash (superscript d) or raw fuel (superscript r), V^{daf} is the proportion of volatile combustible, Q_i^r – gross calorific power of raw fuel.

Table 2

Fuel parameters

Sample	w_i^r [%]	A^r [%]	A^d [%]	C^r [%]	H^r [%]	N^r [%]	O^r [%]	S^r [%]	V^{daf} [%]	Q_i^r [MJ/kg]
Lignite nut 1	27.5	4.18	5.77	46.9	3.83	0.650	16.4	0.620	51.1	19.1
Wood (beech)	9.58	0.83	0.92	41.1	5.11	0.09	43.08	0.22	85.58	15.68

Sampling principle. Before the measurement, the combustion devices were placed on a weigh bridge and fitted with instrumentation for determination of basic operation parameters and flue gas composition behind the boiler and in the dilution tunnel (DT). The schematic diagram of the combustion devices, connection to the DT and location of sampling points is shown in Fig. 2.

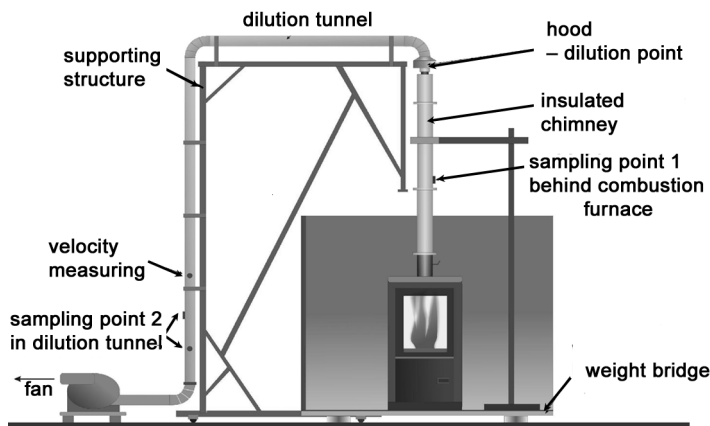


Fig. 2. Scheme of the dilution tunnel

Flue gas composition was measured in two sampling points (1 and 2). With the help of concentration of one component (O_2) in the sampling points, TSP concentrations determined in the DT can be converted to the condition before dilution or to the O_2 reference value. PM determination was performed by the gravimetric method. The principle of the measuring method is based on “isokinetic” aspiration of a gas sample from the DT (sampling point No. 2) and a capture of particular fractions. The impactor made by TCR TECORA (Fig. 3) serves for sampling of particle matter and their dividing to PM_{10} and $PM_{2.5}$ fractions. It is a probe with a retainer in which fractions are separated by centrifugal forces with the help of a jet system and subsequently they are

captured on filters. The titan impactor including 2 dividing levels (for 10 µm and 2.5 µm) was made according to ISO 23210-2009 and it complies with EN13284-1.

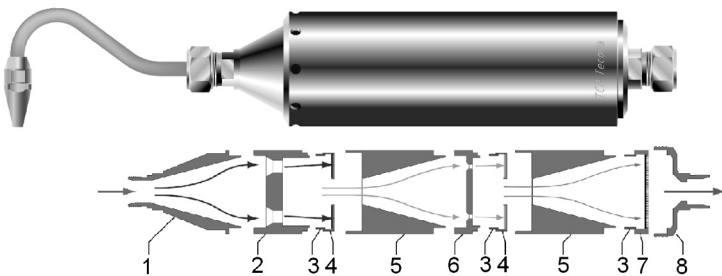


Fig. 3. Scheme of the impactor: 1 – connection cone to sampling nozzle, 2 – I PM10 cut stage, 3 – filter locking ring, 4 – I or II stage filter cassette, 5 – expansion cone, 6 – II PM2.5 cut stage, 7 – backup filter cassette, 8 – filter holder and connection cone to sample probe

The fractions over 10 µm and 10–2.5 µm fractions get stuck on the filter with the help of centrifugal forces, the fractions below 2.5 µm get captured on the filter by sieving of the sample. For capture, filters made of microfiber glass, 47 mm in diameter, MGG type, manufactured by Munktell, were used.

Sampling was carried out in the DT of 150 mm in diameter in which, thanks to dilution, concentration of solids was lower, and constant flue gas velocity c equalled 5–6 m/s. Flue gas sample was taken with the help of a sampling track which enabled maintenance of a required flow rate and, at the same time, it provided data on sampled amount of dry flue gas under normal conditions. The main parts of the apparatus were the Bronkhorst IN-FLOW Select flowmeter and the BUSCH SV 1025C frequency controlled pump. During the experiments, temperature in the DT was ca. 60 °C. The impactor was heated to this temperature as well, with the help of electrical heating strips with regulation. The sampled amount of flue gas was always calculated for the given temperature with the help of a software delivered by TCR TECORA; the sampled amount of flue gas had to be adhered to so that sorting of particle matter was ensured for characteristic 10 and 2.5 µm diameters. Sampling velocity corresponded to the flow rate value about $2.14 \text{ m}_\text{N}^3/\text{h}$. Isokinetics of sampling was provided by the choice of a nozzle with a proper diameter (12 or 14 mm).

Sampling was performed after stoking and then during a stable combustion process (the developed burning). Duration of samplings was given by the filter capacity and TSP concentration in flue gas. In most of the cases, the filter got blocked after ca. 10 min, however, at the gasification boiler, the sampling took 58 min. At stable modes, the TSP concentration was generally lower, therefore sampling periods were longer, they lasted about 30 min. In terms of burning, one sort of fuel in one combustion device, two samplings were always performed; for the automatic boiler, only one longtime sampling was performed.

After sampling, the filters (Fig. 4) were carefully removed and separated components of the impactor were rinsed with acetone into weighing bottles which were weighed beforehand. After evaporation of acetone in free air, the weighing bottles as well as filters were dried in a drier at 105 °C and subsequently cooled down in a desiccator. After cooling, the weighing bottles as well as filters were weighed on laboratory balances with 0.1 mg scale. Corresponding fractions on the filter and in the weighing bottles were summarized.

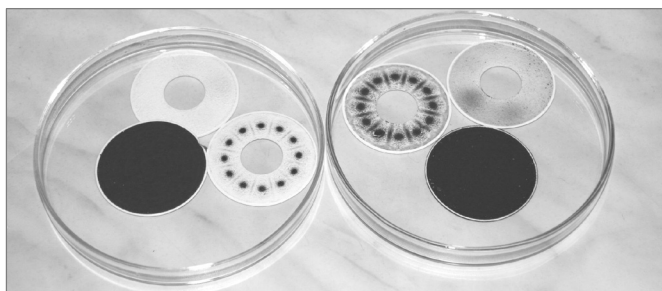


Fig. 4. Particular dust fractions on filters

Based on flue gas velocity, it was possible to determine its flow rate in the DT and mass flow of TSP and particular fractions. Based on the known fuel consumption and calorific power, specific emissions of TSP and particular fractions in mg/kg or in g/GJ were determined subsequently.

For all the devices, sampling was performed during a stable mode which was not operator intervened (door opening, fire poking, stoking-up, ash grate moving, etc). The devices were operated on nominal heat output and under the manufacturer recommended conditions. For the hand fired devices, sampling after servicing (stoking up and ash grate moving) which is necessary at a real operation, was performed as well.

3. RESULTS OF EXPERIMENTS

In Figure 5, the results of determination of particle matter emission factors related to fuel weight are presented. Within stable modes without servicing by an operator, the highest values of specific emissions were reached when burning lignite in the stove and the over fire boiler (135 and 117 g/GJ). On the contrary, the lowest value of 10.5 g/GJ was obtained when burning lignite in the under-fire boiler. For this boiler, the influence of the combustion method and of three passes of the flue way, in which there are convenient conditions for capture of emitted particles from the under-fired lignite bed, became evident. For wood, the highest specific emissions were determined when burning in the under-fire boiler (112 g/GJ). This fact bears evidence of different characteristics of particles emitted when burning wood and lignite and also of different

properties of under-fired wood and lignite beds. Other emission factors during wood burning in the stable modes were very similar and they ranged from 39.4 to 42.6 g/GJ.

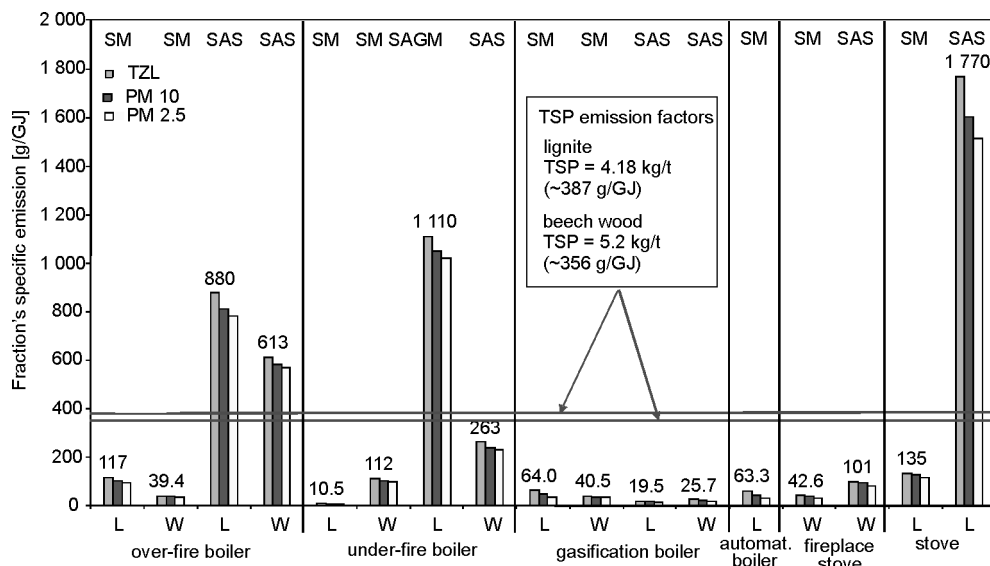


Fig. 5. Emission factors of particle matter fractions when burning lignite and wood: L – lignite, W – wood, SM – stable mode, SAS – sampling after stocking, SAGM – sampling after grate moving

The specific emissions of sampling performed after having intervened to the burning process feature markedly different values. The highest increase of specific emissions occurred in the under-fire boiler where lignite specific emission increased to 1110 g/GJ, which represents ca. 100-fold increase. The highest absolute value was reached for the stove where the specific emission of 1770 g/GJ was determined. The increase for the stove was similar to the increase for the over-fire boiler, 7.5–15.5-fold increase occurred. The specific emission increase for the over-fire boiler and the stove is given by production of a large amount of tar matter after fuel stoking. For the rest of the tests, the increases were significantly lower; for the gasification boiler, even decrease of the specific emission occurred.

The above described unstable conditions after servicing feature different durations, from several minutes to tens of minutes. With regard to mostly significantly different values of specific emission values under unstable conditions and with regard to their duration, it is obvious that they influence the resulting values of specific emissions. In light of influence on health of living organisms, attention is paid to small (respirable) proportions. Size of particles emitted by individual combustion devices when burning particular fuels is shown in Fig. 6. Evident significant differences exist of proportions of particular fractions.

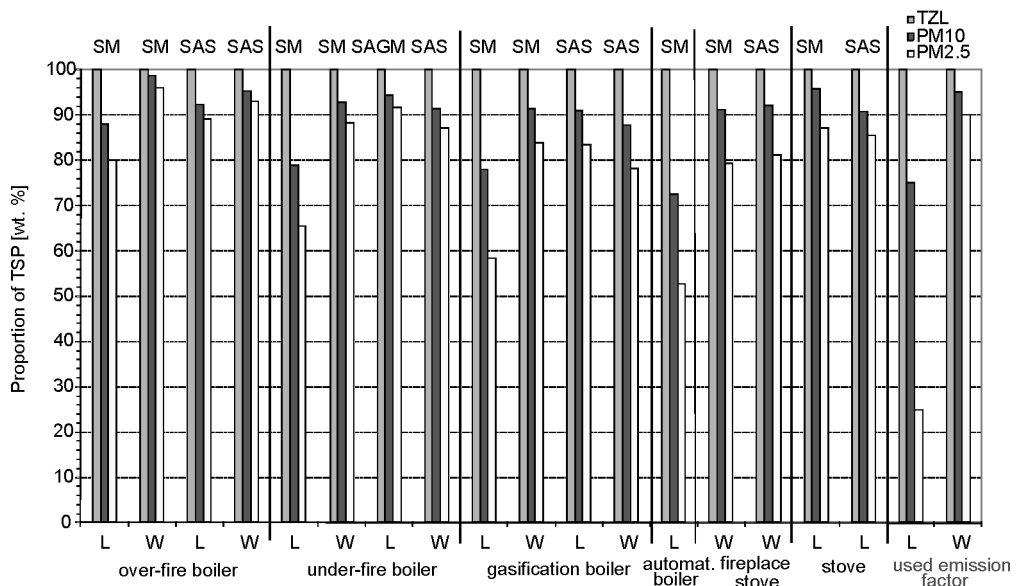


Fig. 6. Proportions of TSP fractions when burning lignite and wood:
L – lignite, W – wood, SM – stable mode, SAS – sampling after stocking, SAGM – sampling

When comparing stable modes, significantly higher production of PM₁₀ and PM_{2.5} fine fractions can be seen when burning wood. The fine particle proportion is influenced by the combustion device used. The highest proportions of fine fractions were determined for the over-fire boiler and the stove. For the over-fire boiler, PM₁₀ proportion ranged about 88% for lignite and over 98% for wood. As to other boilers, there were markedly lower proportions of fine fractions, namely when burning lignite. The lowest proportions were determined for the automatic boiler: PM₁₀ 73% and PM_{2.5} 53%.

By operator intervention into the combustion process, an important change in the emitted particle size spectrum occurred. When burning lignite, a substantial increase of fine fractions occurred mostly because of operator intervention; PM₁₀ proportions exceeded 90% and PM_{2.5} proportions ranged from 84 to 92%. A reverse trend was noted for the stove. The reverse trend was found out for wood combustion, when lower proportions of fine fractions were mostly determined after operator's intervention. For all the boilers, a decrease of both fine fraction proportions of the order of 2–5% occurred in contrast to stable modes. For the fireplace stove, a mild increase of the fine fraction proportion occurred.

4. COMPARISON OF THE SPECIFIC EMISSION VALUES TO THE EFS USED

For the over-fire boiler and the stove, it can be expected that the TSP production decrease after stoking will not be rapid and thus the representative emission factor will

be near an average value. For the boiler, the average values are 499 g/GJ for lignite, 326 g/GJ for wood, For the fireplace stove – 71.8 g/GJ and for the classic stove – 953 g/GJ. For the under-fire boiler, a rapid decrease to the values obtained in the stable mode can be expected; moreover, the under-fire boiler features a longer stoking-up period and a longer flue way than the over-fire boiler. For the above-mentioned reasons, the representative emission factors will range near the value which was found-out for the stable mode.

When comparing to the emission factors used in the Czech Republic for yearly balances of particle matter production, there is a noticeable difference (see Fig. 5). The used factors are higher than the specific emissions obtained for the under-fire and gasification boiler. On the contrary, the specific emissions determined for the over-fire boiler correspond to EFs. For the classic stove, the specific emissions exceed the used EF more than twice. Other emission factors used in EU are also higher in comparison to the experimentally obtained values, when compared to the emissions from more up-to-date boilers and fireplace stoves. On the contrary, for the over-fire boiler and the classic stove, they are lower than the specific emissions determined by the experiment. When comparing, there is a problem of different dividing of combustion devices to new, adapted and old.

A significant difference between the used proportions for fine fractions and the actually obtained proportions can be seen at the size spectrum. The determined proportions of fine particles which originate during lignite burning are higher than for the used EFs. By contrast, proportions of fine particles which originate during wood burning are lower than for the used EFs. For wood, the differences can be caused by fuel humidity. It is presumable that the specific emissions would be higher with higher fuel humidity.

5. CONCLUSION

The measurements proved that individual small furnaces, though they burn the same fuel, feature big differences in TSP specific emissions. Aside from the over-fire boiler and classic stove, lower specific emissions than the used EFs were determined for all the boilers. As to fine fractions, we can state that the determined proportions of fine particles which originate during lignite burning are higher than for the used EFs, contrariwise proportions of fine particles which originate during wood burning are lower than for the used EFs.

When comparing proportions of fine fractions, it is evident that larger proportions of fine fractions are emitted during wood burning.

The presented results show that composition of combustion devices affects significantly the real emission balance however, it is not included into emission calculation in the Czech Republic because of lack of information.

The main parameter affecting particle matter emissions is a type (design) of a combustion device. Dividing to new, adapted and old combustion devices is not an adequate parameter for EF specification. Over-fire boilers represent an old design and they produce considerably high particle matter emissions. In the Czech Republic, this type of a boiler is one of the best sold devices. Compared to that, older under-fire, gasification or automatic boilers can produce relatively low specific emissions which, in addition, are not influenced by servicing very much.

Fuel sort and combustion process setup has a big influence as well. The authors find EF specification for combination of fuel and a combustion device type more suitable for calculation of emission balances of small furnaces.

The presented specific emissions from individual combustion devices will be precisely by repeated sampling. Experiments with other fuels will be performed.

ACKNOWLEDGEMENT

This paper has been elaborated in support of the Ministry of the Environment within the scope of the SP/1a3/148/08 project *Determination of Particle Matter Chemical and Toxicological Properties and Research of their Origin* and of the Czech Science Foundation within the scope of the project No. 101/09/1464 *Thermodynamic Analysis of Biomass Combustion and Gasification*.

REFERENCES

- [1] BRANIŠ M., *Classified sampling of emissions*, Dissertation thesis, Praha, ČVUT, 2009 (in Czech).
- [2] HLAWICZKA S., KUBICA K., ZIELONKA U., WILKOSZ K., *Properties of emission of dust and heavy metals in coal combustion process in home combustion devices*, [In:] *Archiwum Ochrony Środowiska*, Zabrze, Instytut Podstaw Inżynierii Środowiska PAN, 2001, 27 (2), 29–45 (in Polish).
- [3] EMEP/EEA *Air Pollutant Emission Inventory Guidebook 2009*, Copenhagen, European Environment Agency, 2009; <http://www.eea.europa.eu/publications/emep-eea-emission-inventory-guidebook-2009>
- [4] CEPMEIP (Co-ordinated European Programme on Particle Matter Emission Inventories, Projections and Guidance), 2002, <http://www.air.sk/tno/cepmeip/>

MICHał ZIELINA*, WOJCIECH DĄBROWSKI*

IMPACT OF RAW WATER QUALITY ON OPERATION OF VARIABLE DECLINING RATE FILTER PLANTS

According to some numerical models of variable declining rate filters in a bank changes in raw water quality do not interfere with values of flow rates through filters as long as subsequent back-washes in a plant start always for the same water surface level above filter media. This simple operational rule was previously tested numerically. Now some results of experimental tests are also presented. Laboratory experiments confirm the operational rule predicted theoretically and supported by numerical computations.

1. INTRODUCTION

Despite intensive development of modern membrane techniques such as micro- and ultrafiltration [1, 2], traditional rapid filters are still widely used in water treatment to remove natural suspended matter or that produced in the process of coagulation, as well as iron and magnesium compounds [3]. In the first drinking water treatment plant applying Pall AriaTM membrane technology in Poland (Sucha Beskidzka), rapid filtration is used as a water pretreatment process which was recognized to be necessary for economical operation of 0.1 µm hollow fibre membranes. Lack of using chemicals for cleaning purposes makes rapid filtration not only economical, but also environmentally friendly technology. Though perhaps low-pressure membrane processes will dominate water purification systems in the future, yet their widespread use is limited due to their short life caused by fouling [1, 2]. Rapid filters owing to simple backwash system are allowed to work for long time at adequate pressure and capacity. However, frequent washing of rapid filters disrupts stable work of the station and causes sudden changes in flow -rate and pressure. VDR filters operation system significantly reduces these changes giving economic benefits by lengthening filter cycle and decreasing backwash frequency.

*Cracow University of Technology, Water Supply and Environmental Protection Institute, ul. Warszawska 24, 31-155 Cracow, Poland. Corresponding author M. Zielina, e-mail: mziel@vistula.wis.pk.edu.pl

Variable declining rate filters (VDRF) are equipped with orifices installed at outflows of filtrate from each filtration unit. These orifices create head losses of turbulent nature. Inflows to all filters are located below the lowest possible water level above filter media. The friction to flow created by pipes and valves should be negligible in comparison with the head loss of flow through the plants so water surface above filters fluctuates in time but essentially the same above all filters in any moment. Filters are backwashed in the same order. The backwash of the next filter starts when water surface above filters reaches a given level which should be calculated. Flow rates through all filters change rapidly just after each subsequent backwash in the plant which is illustrated in Figs.1, 2. During a backwash one of units is out of service, thus the remaining filters accept more raw water. The consequence of the sharp water level rise is a sudden increase in filtration velocities. After a backwash, the clean filter is put into the service again and is operated with the highest flow rate in the plant. As each of the filters is backwashed at different moments, they are operated under different flow rates. More details about VDRF construction and operation can be found elsewhere [4–8].

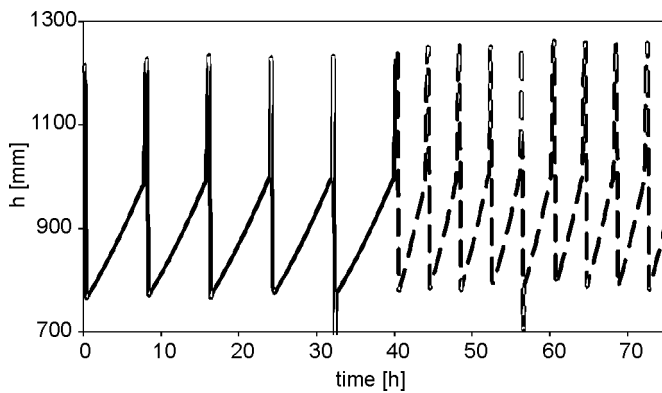


Fig. 1. Water table fluctuations for a sudden change of supply from a reference suspension I (solid line) to suspension II (dashed line) of different size gradations and concentrations according to computations published previously [9] and based on a simple UBE model of variable declining rate filters [11, 12]

Variable declining rate filters control systems are designed for stable operational conditions including temperature and quality of raw water. Such stable conditions are fulfilled only when deep groundwater is being treated, are somewhat realistic for filtering infiltration water and totally unfeasible for treatment of surface water. The discrepancies between theoretical assumptions considered at the designing step and reality do not stimulate application of theory into routine design methods. However, in our recent papers [9, 10] we have deduced that according to two different mathematical models as long as the raw water temperature is constant, the flow rates are practically

the same after sudden change in raw water quality if only the backwashes start for the same water level above all filters.

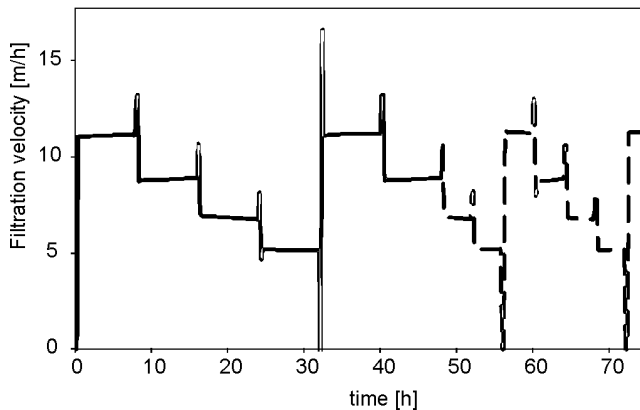


Fig. 2. Distribution of filtration velocities among four VDR filters before and after change of supply from reference suspension to suspension II (dashed line) of various size grades and concentrations according to computations [9] done based on a UBE model [11, 12] of variable declining rate filters

A rule for the operation of variable declining rate (VDR) filter plants under conditions of sudden changes in influent water turbidity has been tested using a mathematical model based on the unit bed element (UBE) approach. A UBE model developed by Mackie and Zhao [11] and adapted for Variable Declining Rate operation was used to investigate a plant behaviour in response to rapid changes in raw water quality. Two different cases have been considered. In the former, only the concentrations of solid particles were the subject of change and in the latter the particle size distribution changed as well. Numerical simulations were carried out under backwashing starting when the water level above the filters reached the same level (Fig. 1). It was found that this resulted in almost identical flow rates through each of the filters, but the length of filter runs, and the effluent quality were significantly different (Fig. 2). In conclusion for waters of stable temperature but different turbidities, backwashing should start for the same water level above the media, even if the raw water quality changes. None reliable mathematical models exist applicable for coagulated suspension flow through porous media, thus this conclusion has to be verified experimentally.

2. LABORATORY SET-UP

A four filtration column pilot plant has been constructed at the Cracow University of Technology. The columns were equipped with orifices installed at outflows and

operated in a variable declining rate manner. Two photographs of the laboratory set-up are presented in Figs. 3 and 4.

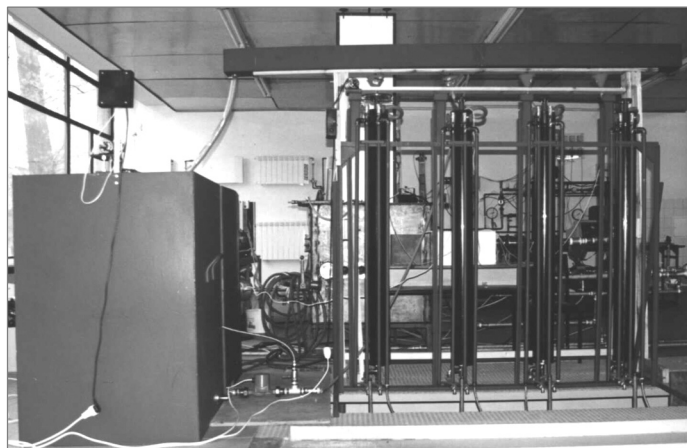


Fig. 3. Suspension tanks and flocculators located at the upper floor

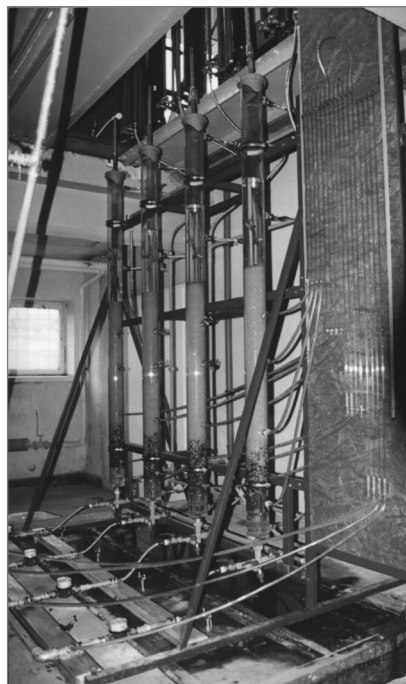


Fig. 4. Filtration columns located at the lower floor (below flocculators)

Suspensions kept in three tanks were in continuous movement due to internal re-circulation and mechanical stirring. Three different suspensions, all of the same tem-

perature equal to 16 °C but of different concentrations of suspended solids were prepared and used one by one. Each time suspension was pumped to a device controlling flow rate. This device was equipped with an orifice of an adjustable position enabling a precise adjustment of flow rate to a requested value. Then aluminium sulfate (5 wt. %) was injected to suspension streams just before four flocculators. The doses of coagulant were previously predicted in jar tests in function of concentration of clay suspension. Mechanical flocculators were divided into three compartments. The Stein–Camp gradient of mixing was about 80 s⁻¹ at the last compartment. After flocculation, suspension was directed to the system of filtration columns operated under a variable declining rate control system. The inside diameter of the columns was 0.098 m. Each column was equipped with a flowmeter and the total outflow from the plant was recorded again to verify the readings. The relative errors of flow rate measurements were below 0.5% in the range of flow rates from q_1 to q_4 , where subscripts refer to the number given to each of filtration column starting from the one just after a backwash q_1 and ending at the one just before its backwash q_4 .

Table 1
Media sand gradation

Fraction diameters [mm]	Content [%]
0.4–0.5	10.0
0.5–0.63	18.8
0.63–0.8	31.2
0.8–1.0	36.1
1.0–1.25	3.9

The gradation of sand used in the experiments is summarized in Table 1. The sand is quite fine in comparison with Polish standards and it follows rather British guidelines.

3. METHOD

The experimental filter plant was supplied with clay suspension of the concentration of suspended solids of 7 mg/dm³ coagulated with 7.5 mg/dm³ of aluminium sulfate Al₂(SO₄)₃·14H₂O for a period covering three backwashes of each of the column. This introductory period was necessary to prepare the filter media resistance to flow, different for each of the filtration columns and corresponding to values appropriate for the variable declining rate operation with a given value of the total head loss of flow through the media, the drainage and the orifice just before a subsequent backwash in a plant H and to the height of water surface fluctuations above filter media between backwashes h_0 . Values of H and h_0 were the same during the introductory period and then identical till the end of the experiments. Flow rates through filtration columns after

completing the third backwash for each of the column were almost identical to flow rates after completing the second backwash thus it seemed that the columns were ready for starting the major part of the experiment. In this part, clay suspensions of various origins, solids gradation and suspended solids concentrations were supplied from each of three suspension tanks one by one. The dose of alum was adjusted to each of the three suspensions as predicted previously in jar tests. These doses had much more visible impact on head losses development in filtration columns than the concentrations of clay suspended solids used in the experiments. The rotation speed of the stirrer was the same the whole time but due to different doses of coagulant it was expected that flocculation produced flocs of different sizes, thus also of different densities [13]. Some microscope observations of floccules and flocs supported this hypothesis.

4. RESULTS

The operation of the laboratory filtration plant was conducted starting the backwashes from the same value of H as applied in the primary part of the experiments. The water surface level was subject to dynamical changes and backwashed intended to be uniquely long but in practice they differed a little, thus the lowest head loss of flow through filtration columns equal to $H - h_0$ not always was exactly the same. The differences did not exceed however the average value by ± 2 cm. Moreover, the same period of taking one of the filters out of service for backwash resulted in different clogging of remaining filter media depending on suspension actually used for the plant supply. A pattern of the fluctuations of water surface and changes in flow rates in time are presented in Figs. 5 and 6.

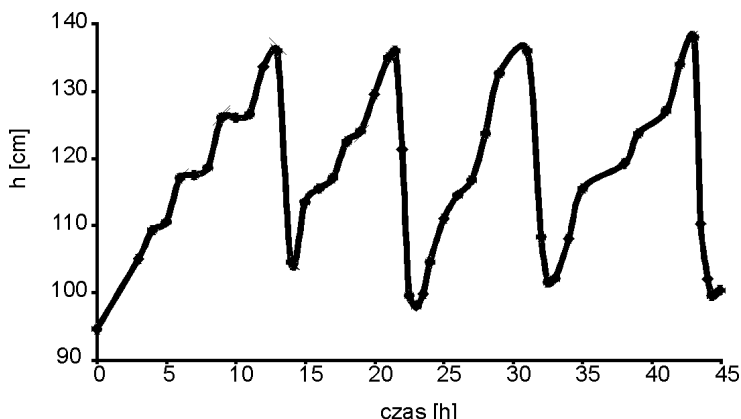


Fig. 5 Experimental time dependence of water surface fluctuations above filter media. h denotes the total head loss of flow through filter media, drainage and orifice

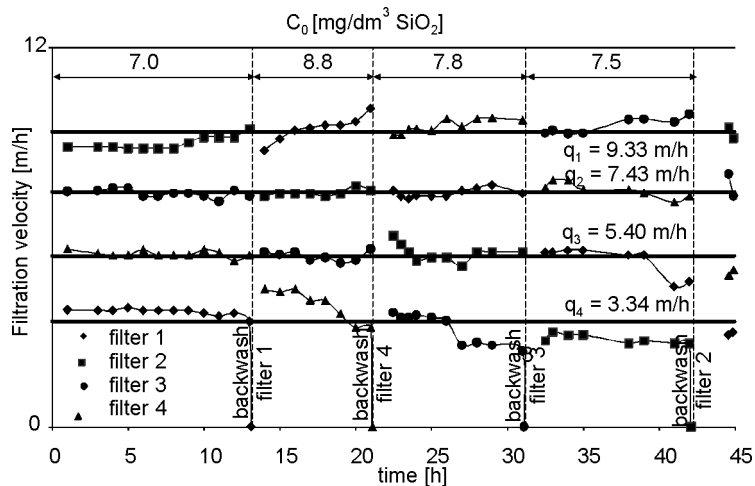


Fig. 6. Recorded time dependences of filtration velocity through filtration columns for various suspensions supplying the plant

For the plant operation based on starting backwashes when the water surface reached the same level, the flow rates illustrated in Fig.6 remained essentially the same in spite of different suspensions used and visibly different periods between subsequent backwashes in the plant. If one of flow rates tended to increase or decrease between subsequent backwashes in the plant, then at least another one behaved oppositely because the total flow ratio of inflow remained the same and the accumulation of water above filter media is limited. The average values of flow rates were denoted in Fig. 6 by horizontal solid lines.

5. CONCLUSIONS

The experiments confirmed our previous expectations [9, 10] that as long as the suspension temperature is constant changes of raw water quality do not disturb the water flow distribution among VDR filters if only all backwashes in the plant start exactly when the water surface level above filter media reaches the same value H . This refers to both series of experiments in which first only the concentration of suspension and then also suspended solids size diameters were subjects of changes. Thus in the same season this simple rule may be applied to keep the same flow rates through filters, and what is more important, the same pattern of filter media resistances to flow at the end of each subsequent backwashes in the plant. Unfortunately, adjusting the flow rate self control system to different temperatures (different seasons) requires more substantial changes [7] in operation as turbulent head losses in drainage and orifices do not depend on temperature but in filter media does.

ACKNOWLEDGEMENTS

The research was sponsored by the Polish Ministry of Science and Higher Education, grant No. 4 T09D 031 25 realized from 2003 to 2006 and 1235/T09/2005/28 realized from 2005 to 2007.

REFERENCES

- [1] KONIECZNY K., RAJCA M., BODZEK M., GEMBOŁYS B., Ochrona Środ., 2008, 30 (3), 3.
- [2] KONIECZNY K., RAJCA M., BODZEK M., KWIECIŃSKA A., Environ. Prot. Eng., 2009, 35 (1), 5.
- [3] VALENTUKEVICIENE M., Environ. Prot. Eng., 2009, 35 (3), 135.
- [4] ARBOLEDA J., GIRALDO R., SNEL H., J. Am. Water Works Assoc., 1985, 77 (12), 67.
- [5] CLEASBY J.L., DI BERNARDO L., J. Environ. Eng. Div (Am. Soc. Civ. Eng.), 1980, 106 (EE6), 1043.
- [6] CLEASBY J.L., Water Sci. Technol., 1993, 27 (10), 151.
- [7] DĄBROWSKI W., MACKIE R.I., Arch. Hydro-Eng. Environ. Mech., 1994, 41 (3–4), 37.
- [8] DI BERNARDO L., Filtr. Sep., 1987, 24 (5), 338.
- [9] MACKIE R.I., DĄBROWSKI W., ZIELINA M., Environ. Prot. Eng., 2003, 29 (1), 45.
- [10] MARZEC J., DĄBROWSKI W., Ochrona Środowiska, 1996, 61 (2), 19.
- [11] MACKIE R.I., ZHAO Q., Water Res., 1999, 33 (3), 794.
- [12] MACKIE R.I., ZIELINA M., DĄBROWSKI W., Acta Hydrochim. Hydrobiol., 2003, 31 (1), 25.
- [13] HO L., Newcombe G. Water Res., 2005, 39 (15), 3668.

